CHARACTERIZATION AND PETROPHYSICAL ANALYSIS OF "LOW-CONTRAST" THIN BEDDED VICKSBURG RESERVOIRS, TCB FIELD, KLEBERG COUNTY, TEXAS

By

HAN LI

Bachelor of Engineering
Sinkiang Petroleum Institute, China
1993

Master of Science
Research Institute of Petroleum Exploration
and Development, China
1997

Submitted to the Faculty of the
Graduate College of the
Oklahoma State University
in partial fulfillment of
the requirements for
the Degree of
MASTER OF SCIENCE
July, 2000

CHARACTERIZATION AND PETROPHYSICAL

ANALYSIS OF "LOW-CONTRAST" THIN

BEDDED VICKSBURG RESERVOIRS,

TCB FIELD, KLEBERG COUNTY,

TEXAS

Thesis Approved:

Zuhair al-Shaieb

Thesis Advisor

Gary J. Stewart

Michael Nichols

Norbert Dahlgren

Dean of the Graduate College

ACKNOWLEDGMENTS

I would like to extend my sincere gratitude to my advisor, Dr. Zuhair Al-Shaieb for his consistent guidance, encouragement, and unselfish support from all aspects. His enthusiastic attitude toward geology, broad knowledge and genuine friendship with students are all unforgettable throughout my life. I also want to express my heartfelt appreciation to my thesis committee members Dr. Gary Stewart and Dr. Mike Nicholl for their assistance, encouragement and friendship throughout this study. Mr. Jay Patchett's suggestions, comments, and support were invaluable in the interpretation of petrophysical component of the study.

I would like to thank my former fellow graduate students Jingyao Gong, Paul Blubaugh and Syed Mehdi and current fellow graduate student Phebe Deyhim for their encouragement and helpful suggestions.

A special thank is extended to Dr. Jim Puckette for his friendship and helpful advice and continuous encouragement. Besides, some thin section photos in Chapter IV were taken by Dr. Jim Puckette.

I would like to thank Dr. Phil Ward in Plant and Soil Science Department at Oklahoma State University for his great help in CEC measurement. Great thanks to James J. Howard in Phillips Petroleum for the Capillary pressure measurements.

Last but not the least, thanks to my mom, dad and husband. I can not finish this thesis without their spiritual encouragement.

TABLE OF CONTENTS

Chapter Page

LIST OF TABLES

LIST OF FIGURES

CHAPTER I

INTRODUCTION

General Statement

Significant reserves have been found in low resistivity and low contrast (LR/LC) oil and gas reservoirs. Abundant research work and drilling activities were carried out on LR/LC reservoirs, especially at the depletion of other conventional reservoirs. However, these subtle-type LR/LC reservoirs are difficult to identify and evaluate. They are often ignored due to the calculated high water saturation values from most water saturation equations. Thinly bedded and laminated nature of many LR/LC reservoirs further complicates the problem. Reservoir identification and productivity evaluation are also dependent on the vertical resolution permitted by logging tools and data processing.

A thinly bedded and laminated gas-bearing LR/LC sandstone in TCB field was selected for integrated core, petrographic and petrophysical analysis. TCB field (Figure 1) produces from multiple sandstone packages of Vicksburg Formation. The gas-bearing LR/LC 9900-ft zone of the Vicksburg Formation, was the focus of this study. Since 1942, TCB field has produced over 104 billion cubic feet (BCF) gas and 2,197,000 barrel condensate (BC) from Lower Vicksburg reservoirs (Int. Oil Scouts Assoc., 1997 and Petroleum Info. /Dwights, 1998). LR/LC 9900-ft sandstone produced over 20.4 BCF gas

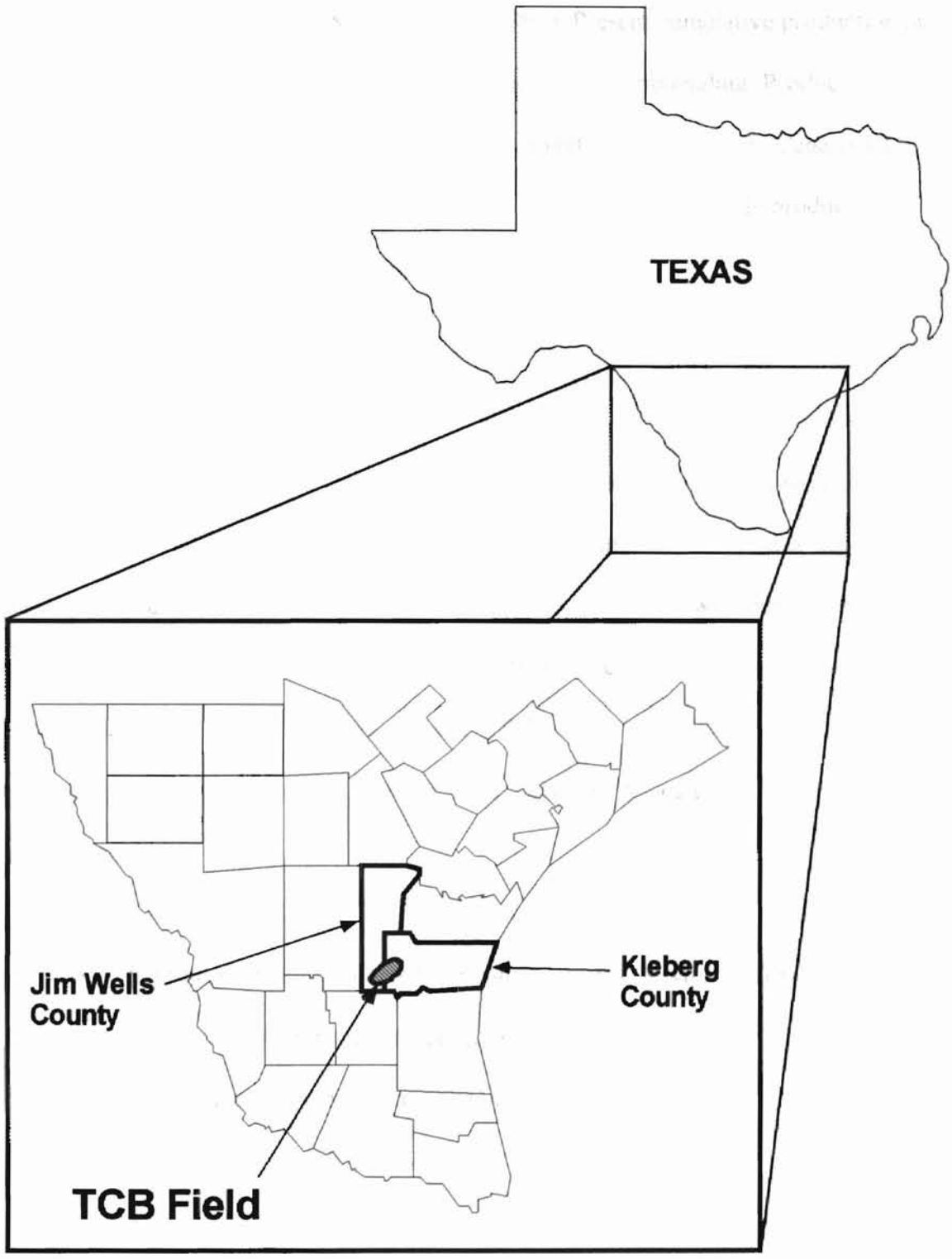

Figure 1. Location of TCB field in Kleberg and Jim Wells Counties, Texas (after Al-Shaieb, et al., 1998).

and 451,000 BC oil before the Lower Vicksburg reservoirs were combined into a common field in 1993 (Int. Oil Scouts Assoc., 1997). Present cumulative production in this LR/LC reservoir could not be determined because of commingling. Production data were available for wells of single-zone 9900-ft completions such as A.T. Canales #81. It has cumulated 1,010,752 MCF and 19,633 BC since 1995 and currently produces 400 MCF and 4-5 BC per day (PI/Dwights, 1998).

Objective of Study

This study is part of a Gas Research Institute Project —— " Improved Evaluation Techniques for U.S. Gulf Coast Reservoirs". The primary goal of this study was to develop improved formation evaluation techniques of the low-contrast 9900-ft zone based on the integration of all petrophysical methods. Specific objectives include:

1. Establish the rock framework of the LR/LC intervals (9900-ft zone), including lithology, bed thickness, detrital and diagenetic constituents and porosity characteristics.
2. Compare measured values of resistivity, porosity, gamma ray and SP from logs to core to determine the effective resolution limits of various wire-line logs.
3. Determine the criteria to identify reservoir zones from wire-line log data.
4. Improve the selection of parameters used in water saturation calculation such as m and n in Archie equation, CEC, Rw, etc.
5. Compare water saturation values from various calculation methods with those from core analyses to determine the most effective formula for water saturation calculation.

6. Establish a set of criteria to improve water saturation calculation in LR/LC reservoir intervals.

Although this study was based on data from TCB field, the result may aid in the evaluation of LR/LC reservoirs elsewhere if factors generating the LR/LC features are similar to those of 9900-ft zone. Factors generating LR/LC features in the studied 9900-ft zone will be discussed in detail in Chapter IV.

Location of Study Area

The studied LR/LC reservoir is located in the TCB field, Kleberg and Jim Wells Counties, Texas. It lies in the lower Gulf Coast Plain of South Texas, 13 miles W. from Riviera, TX (Figure 1).

TCB field lies in the Rio Grande Embayment. Rio Grande and Houston embayments constituent the two major depocenters in Gulf Coast Basin during the Tertiary time.

Methods of Study

There is no surface exposure of the Vicksburg Formation in the study area. Therefore, this study is based on integrated core and wire-line log analysis. Cores of 9900-ft sandstone were obtained from ORYX Energy Company (now Kerr McGee). These cores were first logged on specially designed petrolog forms which contain information on lithology, sedimentary structure, texture and constituents. Cores were then

sampled for thin-section, x-ray, SEM, ϕ-k, capillary pressure and cation exchange capacity (CEC) analyses.

Array induction, gamma ray, neutron-density, micro-imaging and nuclear magnetic logs were correlated to cores of the 9900-ft sandstone. The measurement accuracy of these tools in thinly bedded and laminated reservoirs was estimated. Porosity measurements from core-plugs were compared to porosity from wire-line logs and thin-sections. Color bands from the static micro-imaging log were correlated to other wire-line logs to study the expression of various color bands on other electrical logs. Therefore, reservoir and sealing beds can be better identified from other wireline logs.

A variety of water saturation calculation models were selected to calculate water saturations. Parameters in these calculations were checked to reflect rock properties. Calculated results were compared to core measurements to identify the most effective methods to estimate true water saturation.

CHAPTER II

GEOLOGIC SETTING

Tectonic and Stratigraphic Setting

The Vicksburg Formation was deposited in Early Oligocene. It is underlain by the Eocene Jackson Shale and overlain by Oligocene Frio Formation. The Vicksburg / Jackson contact is represented by a widespread erosional unconformity formed in response to eustatic sea level drop. In the earliest Oligocene, an Antarctic ice sheet was built up because of the global cooling and the eustatic sea level dropped correspondingly (Miller et al., 1987; Miller, 1989).

The global cooling was related to a series of plate reorganization and change in plate configuration from Late Middle Eocene to the Early Oligocene. During the Late Eocene, Tasmanian Seaway between Antarctica and Australia and the Drake Passage between Antarctica and South America were opened. Antarctica and the surrounding seas became cooler. The concurrent development of the Vema Channel in the South Atlantic and the Faroe — Shetland Channel in the North Atlantic (Pomerol and Premoli – Silva, 1986) provided the passage for cold waters from the high latitude to circulate to the lower latitude. This further facilitates the cooling of the global oceanic water and global climate.

Another important tectonic event during the Late Eocene-Early Oligocene was the collision of the Eurasian and Africa-India plates. The resultant partial blocking of Tethyan Seaway (Pomerol and Premoli-Silva, 1986; Ricou et al., 1986) enhanced the influence of the polar currents and global cooling.

During the Late Eocene and Early Oligocene, plate reorganization was also active in the Pacific area. The concomitant volcanic activities were widespread. Vicksburg Formation received large amount of volcanic rock fragments from West Texas- Mexico volcanic activity.

The Frio Formation overlies the Vicksburg Formation with no apparent depositional break between these two formations in Texas (Coleman, 1990). However, there was a change in the volcanic activity of west Texas and Mexico at Vicksburg / Frio boundary. The trans-Pecos volcanism ended during the deposition of Vicksburg Formation and was followed by the Chihuahuan volcanic episode concomitant with the Frio deposition.

The thickness of the Vicksburg Formation varies from 100 to 800 feet in Florida to 10,000 feet in South Texas (Han, 1981). Lithologies change dramatically in response to changes in depositional facies. The Vicksburg Formation is stable, non-clastic platform deposits in Florida and changes to unstable fluvial-deltaic / shallow marine deposits in Texas.

The subdivision of Vicksburg varies in different areas of the Gulf Coast (Figure 2). In TCB field, Vicksburg is subdivided into lower and upper Vicksburg (Figure 3). The type log of Vicksburg Formation of TCB field and the locally defined stratigraphic units

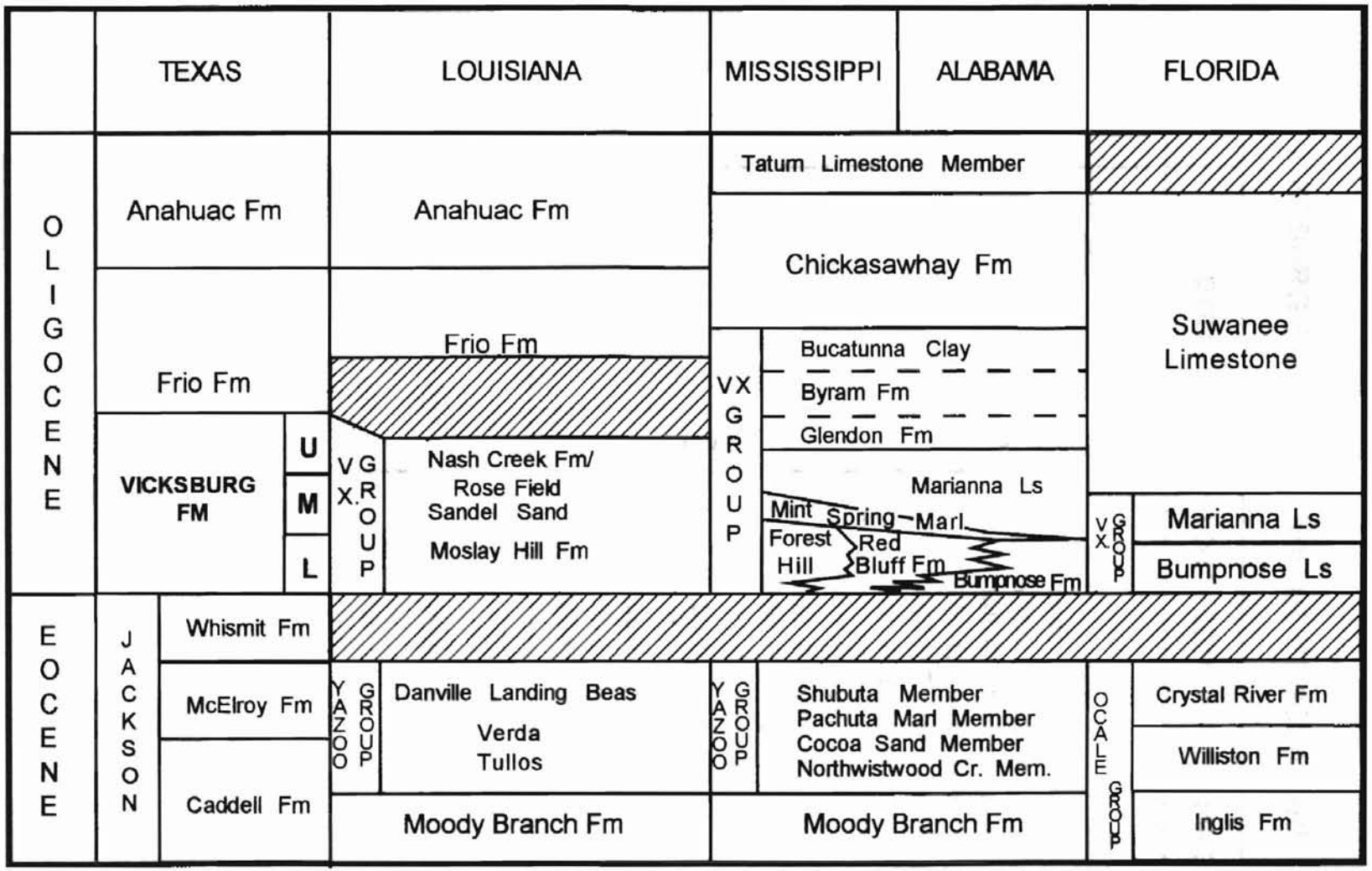

Figure 2. Generalized lithostratigraphic diagram of Vicksburg Formation/Group in Gulf Coast (adapted from Han, 1981, and Pasley and Hazal, 1990).

VICKSBURG STRATIGRAPHIC NOMENCLATURE

	TCB FIELD		LOCAL SUBSURFACE NAMES
OLIGOCENE	Frio Fm		Frio
	Vicksburg Fm	Upper	Nowacek Sandstone Wilson Sandstone 7900-ft Sandstone 8500-ft Sandstone 8650-ft Sandstone 8800-ft Sandstone
		Lower	9000-ft Sandstone 9400-ft Sandstone 9550-ft Sandstone 9900-ft Sandstone 10250-ft Sandstone 10500-ft Sandstone 10600-ft Sandstone 11000-ft Sandstone 11800-ft Sandstone
EOCENE	Jackson Group		Jackson Shale

Figure 3. Stratigraphic nomenclature in the TCB field area, Kleberg County, Texas (After Taylor and Al-Shaieb, 1986).

are shown in Figure 4. These stratigraphic units are traditionally divided by flooding surfaces and can approximately correspond to parasequences.

Structural Geology

The major structural styles of Vicksburg Formation include growth-fault, gravity-glide structure and diapirism. The synchroneity of the growth-faulting and deposition causes the thickening of downthrown blocks. Associated with major faults are migrational rollover elongate anticlines and a series of antithetic faults. Gravity sliding of the continental slope creates a strongly extensional regime along the shelf margin while strong compression predominates the lower slope, featured by the occurrence of shale or salt diapirism (Winker and Edward, 1983).

There are two major fault systems cutting the Vicksburg section, the Vicksburg fault zone and Frio fault zone, among which the Vicksburg growth fault zone is more important (Figure 5). The Vicksburg fault zone consists of a series of interconnected, arcuate faults that are generally parallel to the present coastline and represent the shelf margin position at the time of the Vicksburg deposition (Winker, 1982; Coleman, 1990). TCB field belongs to one of the large fields straddling the second growth fault within the Vicksburg fault zone. The general structural style of TCB field is also dominated by large syndepositional listric normal faults and accompanying "rollover" anticlines (Figure 6). In the earliest Oligocene, TCB field was located on the shelf margin with expanded section developed across the growth-fault, i.e. downthrown side (Figure 7). As a result of basinward migration of shelf margin in Cenozoic (Winker, 1982), TCB field lay on the

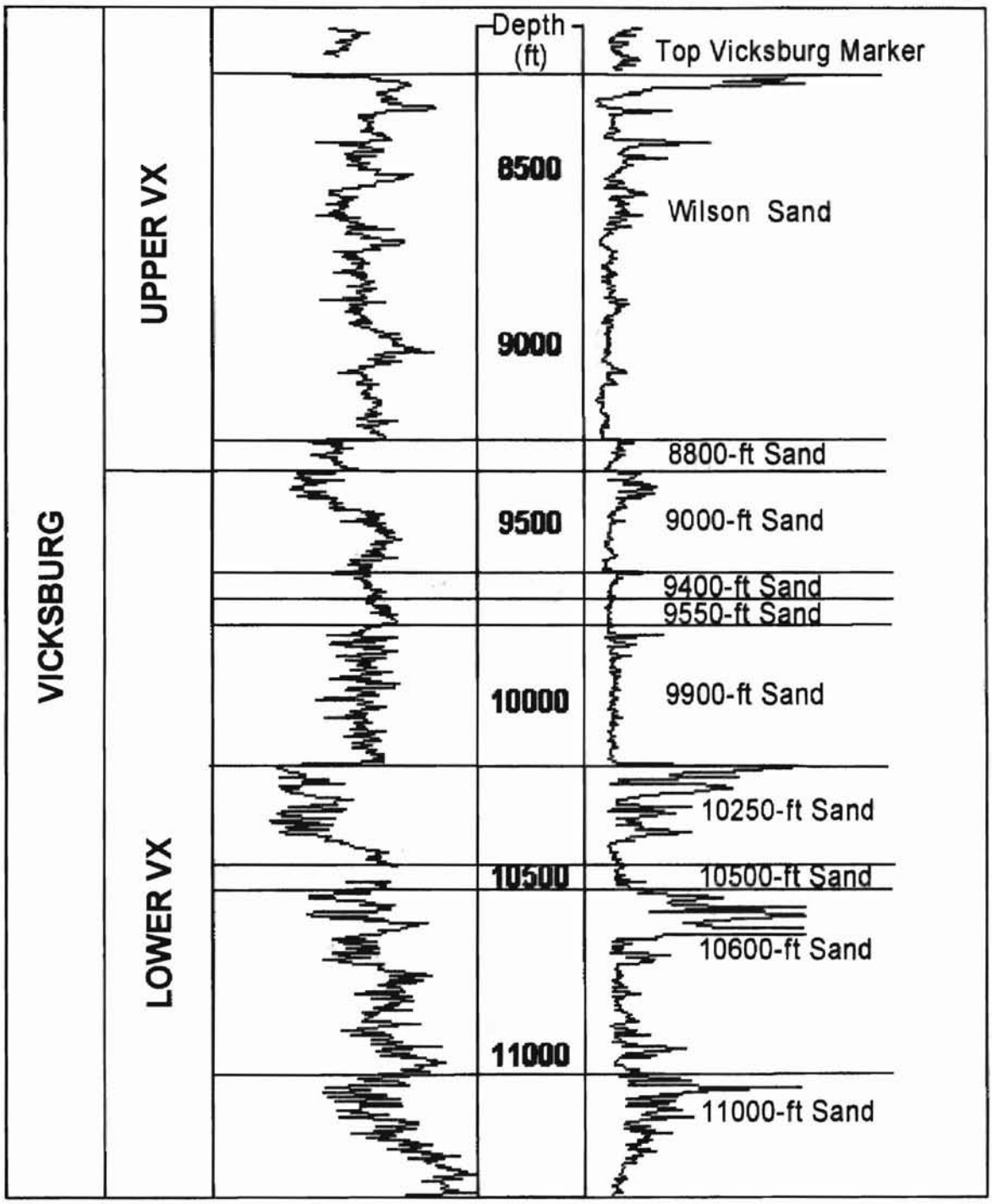

Figure 4. Type log in the study area.

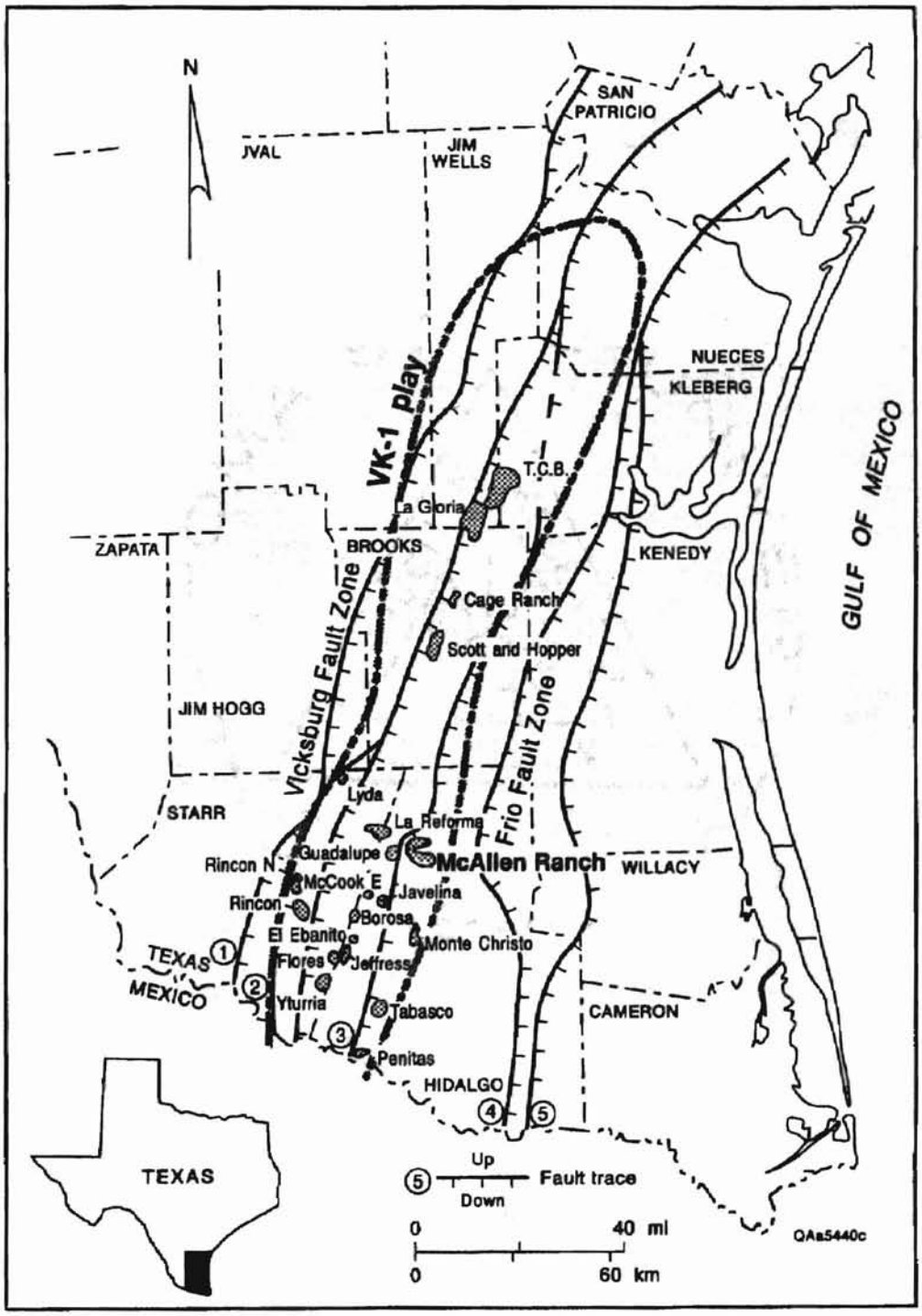

Figure 5. Map of the Texas Gulf Coastal Plain showing TCB field and main faults in the area (after Langford and Combes, 1994)

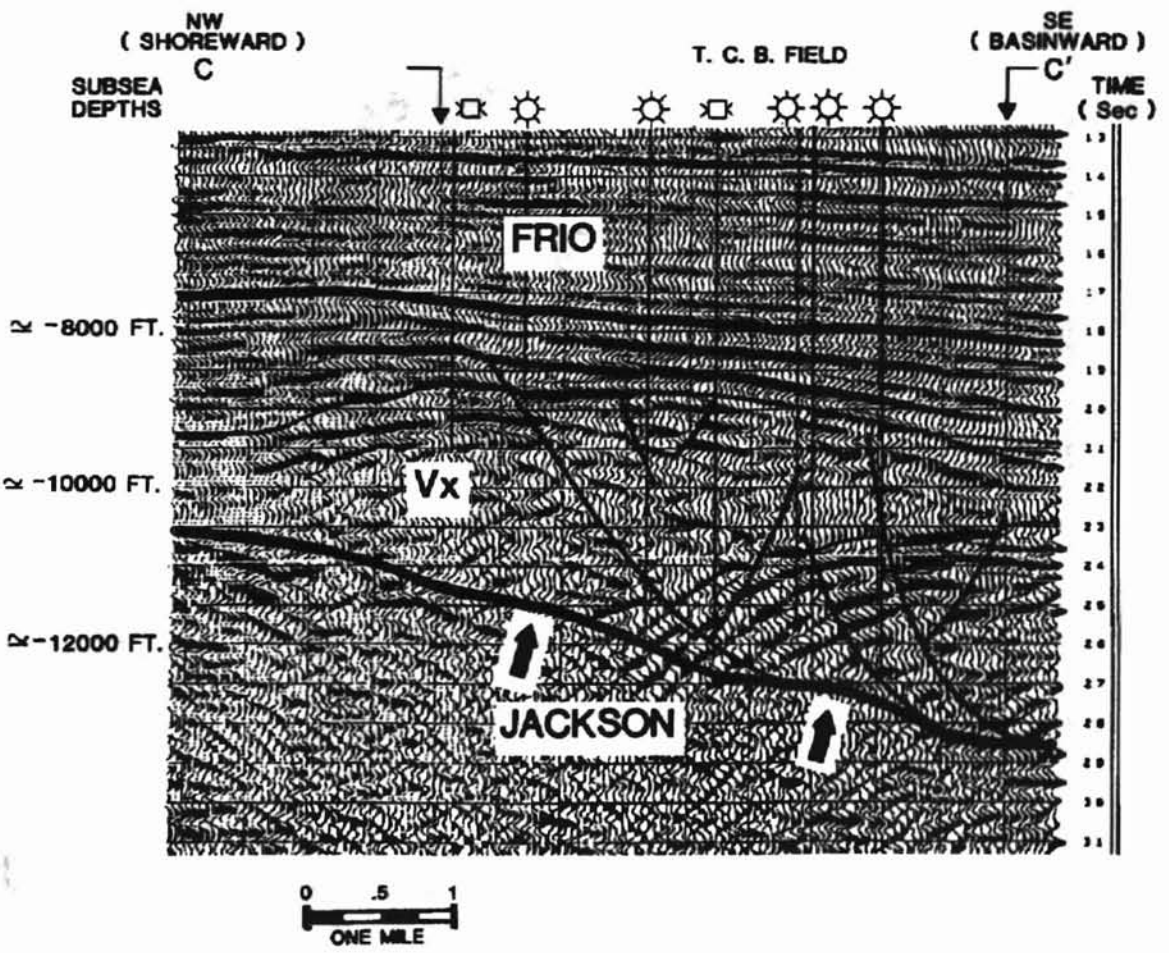

Figure 6. Dip oriented seismic cross-section demonstrating typical structural style for TCB Field (After Taylor and Al-Shaieb, 1986).

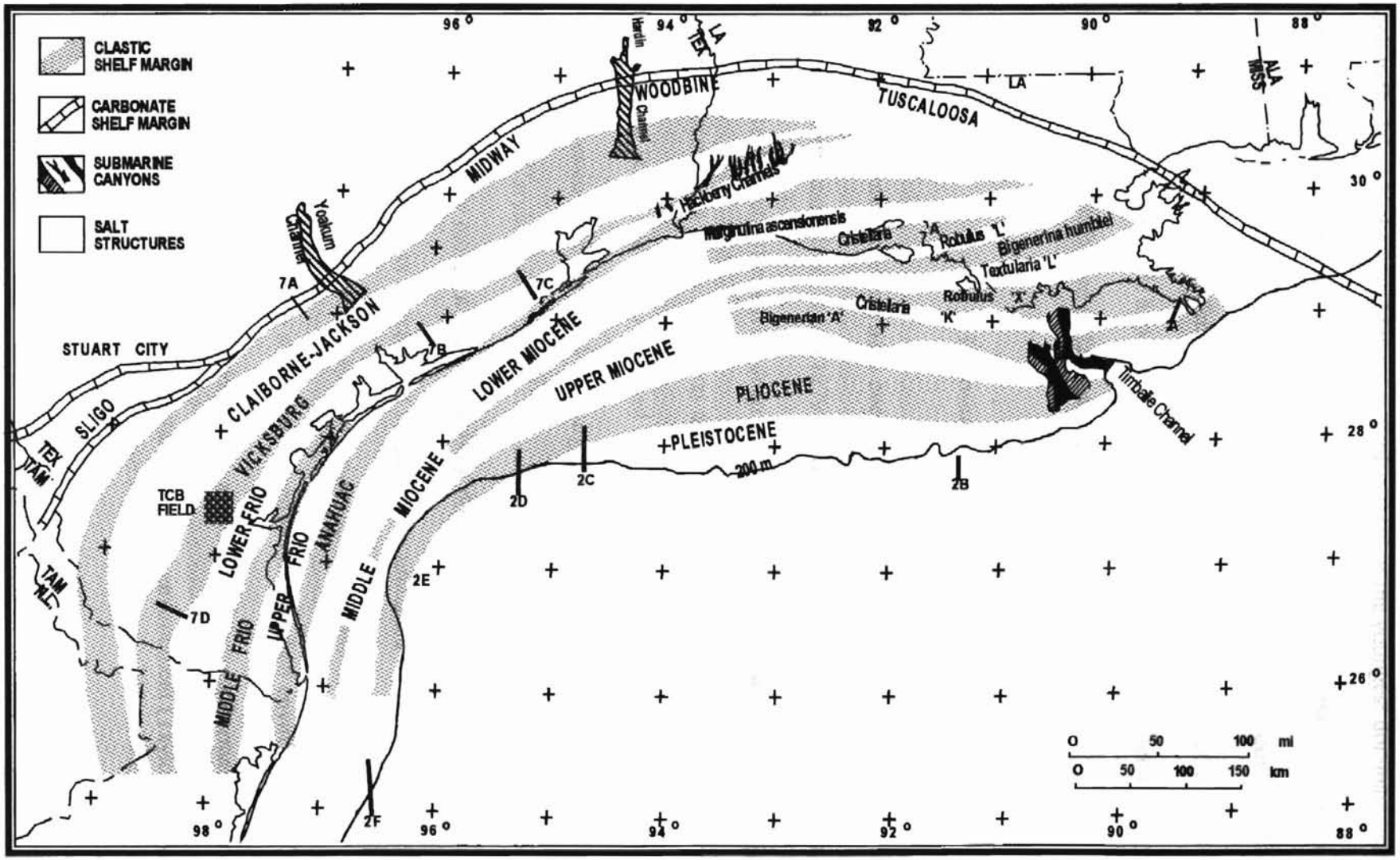

Figure 7. Shelf-margin trends of the northwestern Gulf of Mexico Basin (adapted from Winker, 1982).

shelf in the latest Vicksburg. Maximum displacement of the youngest dominant listric normal fault in TCB field ranges from 200 feet to 400 feet. Displacement seems to be proportional to the amount of sediments loaded on the shelf edge. The quick loading of large amount of sand-rich sediments over underlying shelf margin or slope shale is very unstable. The Jackson Shale appears to be the main surface of the decollement on which the Vicksburg was deformed or faulted (Taylor and Al-Shaieb, 1986).

Depositional Environment

Various interpretations have been given on the depositional environments of the Vicksburg Formation. Berg et al. (1979) held that much of the Vicksburg in South Texas was turbidite deposits of relatively deep water. Loucks (1978) and Han (1981) suggested that the Vicksburg in South Texas was deposited by a series of deltaic progradation. The Vicksburg of TCB Field is characterized by a series of deltaic progradation separated by minor transgression from Lower Vicksburg through Upper Vicksburg (Taylor and Al-Shaieb, 1986). Varying intensities of progradation, subsidence and marine reworking influenced sandbody morphologies. Vicksburg depositional systems were also influenced by growth fault activity as thicker sand sequences accumulated on the downthrown side of the listric faults in response to rapid progradation and subsidence.

The underlying Jackson shale was formed in an open shelf environment in TCB field (Fisher et al., 1970). The Frio Formation above the Vicksburg Formation was interpreted to be deposits in a fluvial-deltaic-strandline environment (Taylor and Al-Shaieb, 1986).

Vicksburg Formation is composed of multiple sand units (Figure 3). The environmental interpretation of the focused 9900-ft zone Vicksburg Formation is mainly accomplished by integrated whole core analyses and electric log signatures.

9900-ft zone spreads across the entire studied area and was cored in A. T. Canales 81 (9900 to 9943 ft) and A. T. Canales 85 (10410 to 10471 ft). Both cores are composed of thinly laminated, very fine-grained sandstone, siltstone and mudstone (Figure 8). Bed thickness is typically less than 2 feet and the maximum single bed thickness in the cored intervals is 4 feet (Figure 9). Ripple laminae, subhorizontal planar bedding and soft-sediment deformation features are common sedimentary structures (Figure 8). Shales and sandstones are extensively burrowed and contain fossil fragments (Figure 10, Appendix A). Burrow types include Ophiomorpha, Zoophycos, Chondrites, Teichichnus, Paleophycus, Planolites and Skolithos.

Gamma ray and spontaneous potential (SP) logs are most commonly used to identify depositional environments. The E-log patterns of 9900-ft zone are characterized by serrated electrical log signature, which is generated by frequent alternation of very fine-grained silty sandstones, siltstone and mudstone.

All above features are indicative of low-energy shallow marine shelf deposits. Sand-rich intervals are formed from the episodic increases in current energy. The sediment input may be associated with the wave-dominated delta and the longshore current reworking. Besides the shallow marine environment, reservoirs of similar low resistivity and low contrast wireline log patterns have been found in other major siliciclastic depositional environments such as channel fills, shingled turbidites and deep water fans including levee-channel complexes (Darling and Sneider, 1992).

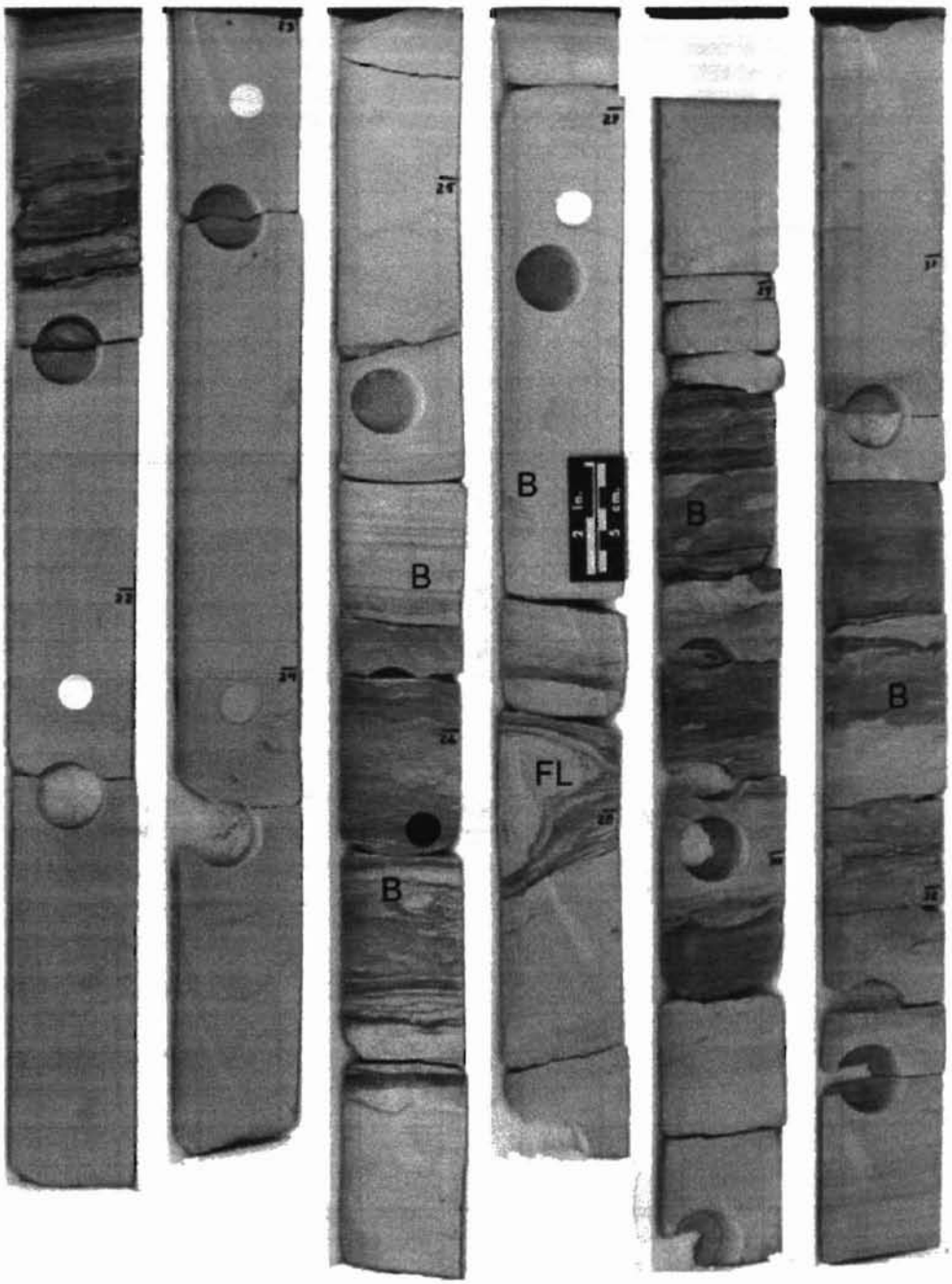

Figure 8. Core photo for 9900-ft sandstone. Major sedimentary structures include sub-horizontal bedding and flowing structure (FL). Burrows (B) can be identified commonly.

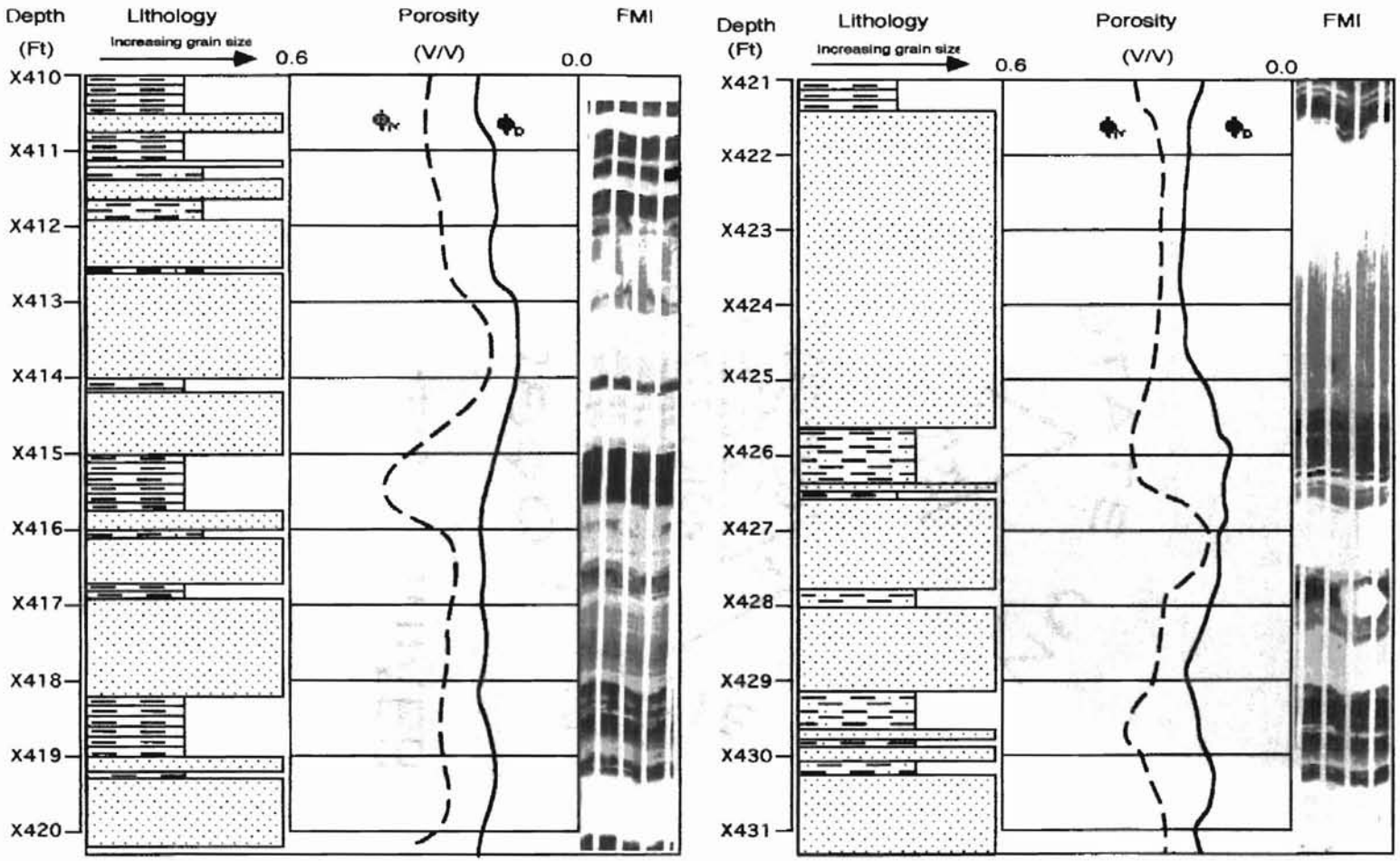

Figure 9. Bed thickness in LR/LC 9900-ft zone is typically less than 2 feet and the maximum single bed thickness in the cored interval is 4 feet.

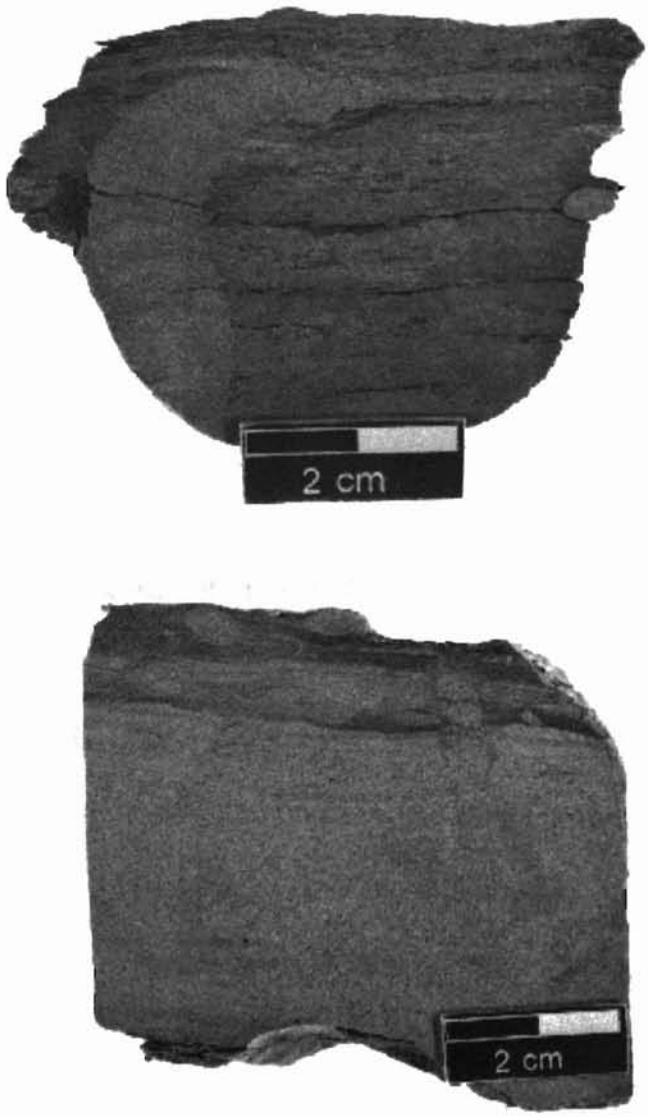

Figure 10. Shales and sandstones are commonly burrowed in 9900-ft zone.

CHAPTER III

PETROGRAPHY AND DIAGENESIS

Introduction

Previous Analysis

Petrography and diagenesis of the Vicksburg sandstone have been studied for about twenty years (Richman et al., 1980; Klass, 1981; Klass et al., 1981; Humphrey, 1986; Taylor and Al-Shaieb, 1986; Langford and Lynch, 1990; Al-Shaieb, et al., 1998). Vicksburg sandstone is notorious for its complex composition. Based on the average composition, Vicksburg sandstones can be classified as feldspathic litharenites with abundant feldspar and volcanic rock fragments. Quartz content is much lower than typical sandstones. Diagnenetic processes have a strong effect on these mineralogically immature rocks. Reservoir quality is greatly affected by the formation of secondary porosity and precipitation of cement and authigenic clays.

The petrographic study was focused on the low resistivity /low contrast reservoir in TCB field to provide a better understanding of the rock properties. This is essential for successful evaluation of reservoir quality and water saturation calculation, etc.

Sampling Procedure

Cores were first examined from bottom to top to obtain general ideas about facies variation and identify distinct changes in color, structure and/or lithology. Samples representative of each facies were selected. Then the cores were examined in detail and more samples were selected to concentrate on burrows, soft sediment deformation and cementation pattern, etc.

Point Count Analysis

Twenty-seven thin sections from the 9900-ft zone of A. T. Canales 81 and A. T. Canales 85 were selected for detailed petrographic analysis. A 100 point counts was performed for each thin section and the results were recorded on a specially designed form. Grain components include quartz, feldspar and rock fragment. Monoquartz and polycrystalline quartz were not counted separately. Plagioclase and K-feldspar were combined since K-feldspar occurs in trace amounts. Rock fragments are mainly volcanic rock fragments. Cements include carbonate and silica.

Texture

The 9900-ft zone is primarily silty very-fine grained sandstone, siltstone and mudstone. Under microscope, the average grain size varies from coarse siltstone to very fine-grained sandstone despite the existence of some fine-grained sand. The majority of the samples are medium sorted, subangular to subrounded and submature to immature in structural maturity.

Classification

The sandstones were classified on the basis of the relative percentages of framework grains. Percentages of framework components were first normalized and then plotted in the Folk (1974) (QRF) ternary diagram. The framework grains used for classification include quartz, feldspar, and rock fragments. As shown in Figure 11, sublitharenite, feldspathic litharenite, subarkose and lithic arkose were the major lithologies identified in individual thin sections. The average compositions were plotted as feldspathic litharenites. These lithologies represent the present composition after the partial to total dissolution of unstable feldspar and rock fragments. The original composition would be represented by higher feldspar and/or rock fragment contents, i.e. plotting toward the middle of the feldspathic litharenite and lithic arkose fields. Detailed petrographic analysis of 27 thin sections were presented in Appendix B.

Framework Constituents

Quartz, feldspar and volcanic rock fragments dominate the framework components, while other rock fragments are present in various amounts. Minor constituents include chert, metamorphic rock fragments, muscovite, biotite, glauconite, zircon, pyrite, tourmaline and shell fragments.

Major Constituents

Quartz is the most abundant detrital mineral found with an average content of 42.6% (Figure 12, Table 1). Quartz grains are mostly monocrystalline and have uniform extinction. Polycrystalline quartz occurs in trace amounts and may be better classified as

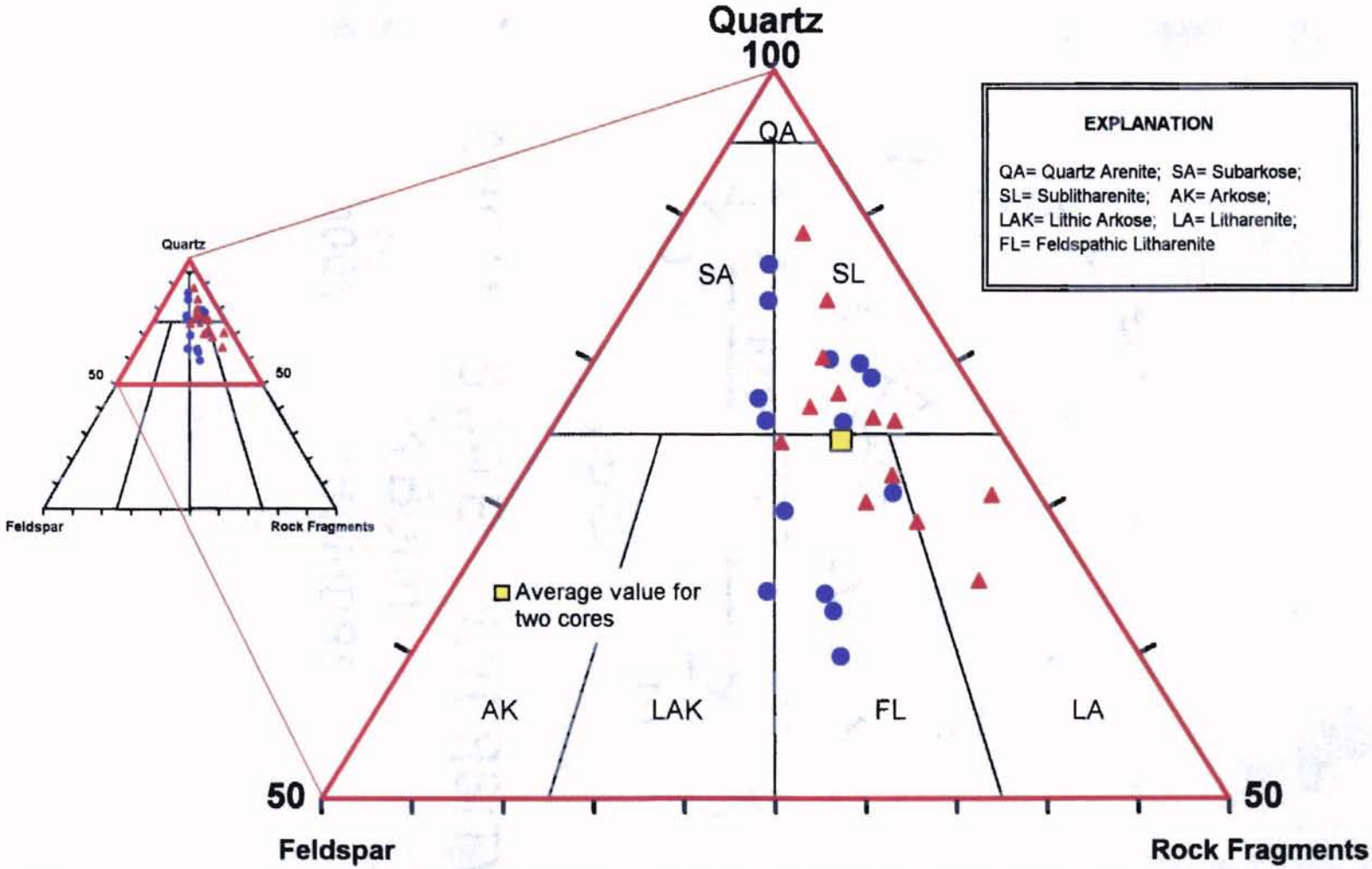

Figure 11. Detrital composition of 9900-ft sandstone as plotted on QRF diagram (Folk, 1974). The average present composition is feldspathic litharenites. The original composition before dissolution would be plotted toward the middle of the feldspathic litharenite and lithic arkose fields.

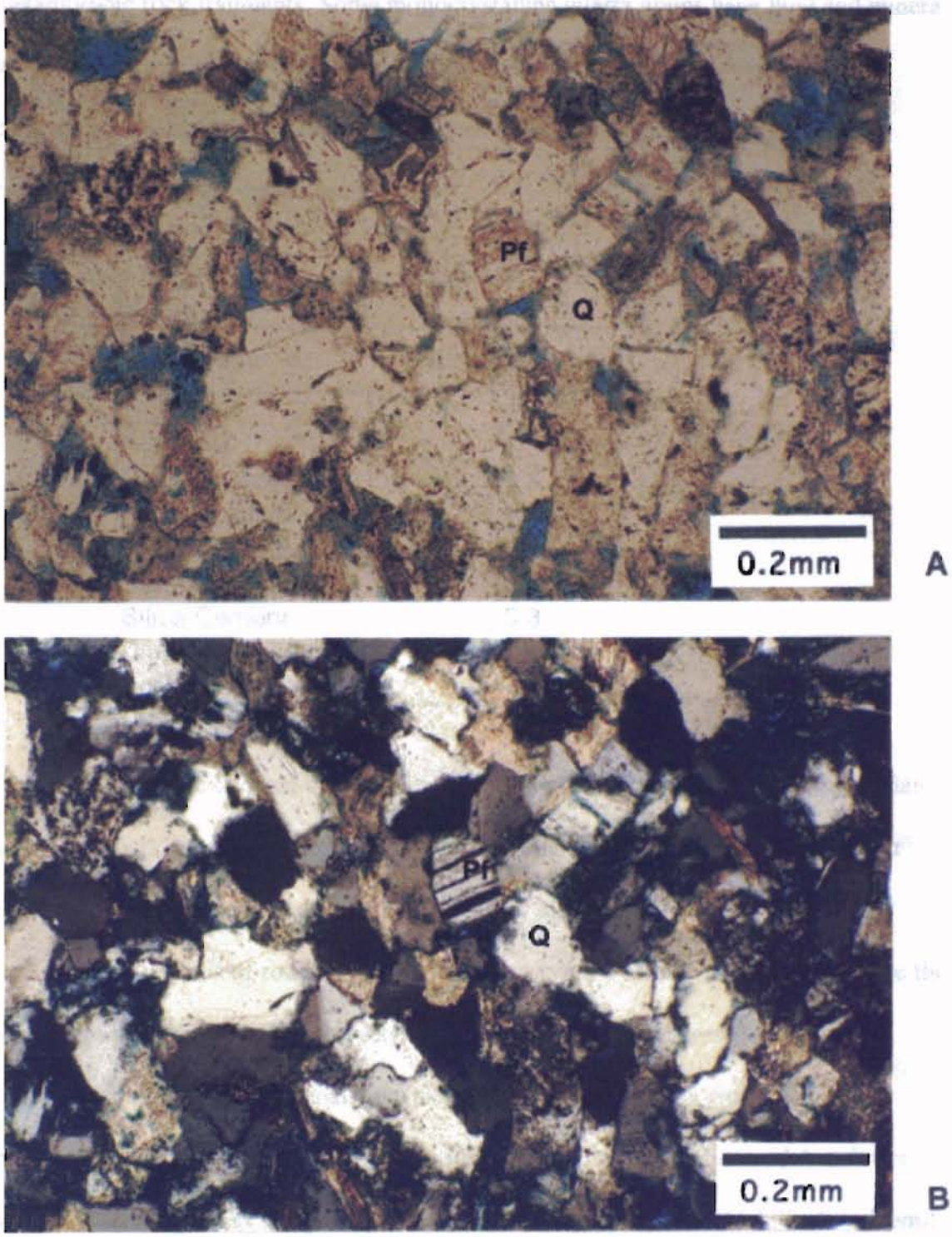

Figure 12. Quartz (Q) is the major framework constituent of 9900-ft sandstone. Quartz is predominantly monocrystalline. Feldspars (Pf) commonly show albite twins and dissolution along cleavage. A. × 100 PPL. B. × 100 XN.

metamorphic rock fragments. Some monocrystalline quartz grains have fluid and mineral inclusions such as zircon, tourmaline, etc. Besides, quartz grains commonly have corrosion features. The size of quartz grains mainly varies from 0.06 to 0.25mm, i.e. coarse silt to very fine-grained sand.

Table I. Average composition and porosity of 9900-ft zone.

Component	Percentage (%)
Quartz	42.6
Feldspar	5.3
Rock Fragments	9.5
Minor Constituents	1.2
Detrital Matrix	6.4
Carbonate Cement	13.5
Silica Cement	0.3
Diagenetic Clay	14.0
Porosity	7.1

The average feldspar content is 5.3%, with plagioclase being the most abundant. These feldspars commonly show twins and/or dissolution along cleavage. K-feldspar only occurs in trace content, partly due to its easy dissolution feature.

Various kinds of rock fragments were observed. Volcanic rock fragments are the most abundant which is 6.4% in average and up to 10% in some samples. In some volcanic rock fragments, original volcanic textures are well preserved, with feldspar phenocrysts easily identified (Figure 13). Sericitization, devitrification and dissolution of volcanic rock fragments are quite common. Therefore, it is somewhat difficult to identify them. Argillaceous rock fragments are the next significant rock fragments, taking up 2.7% in average (Figure 14). Carbonate rock fragments, chert and metamorphic rock fragments also exist, but are minor constituents (Figure 15).

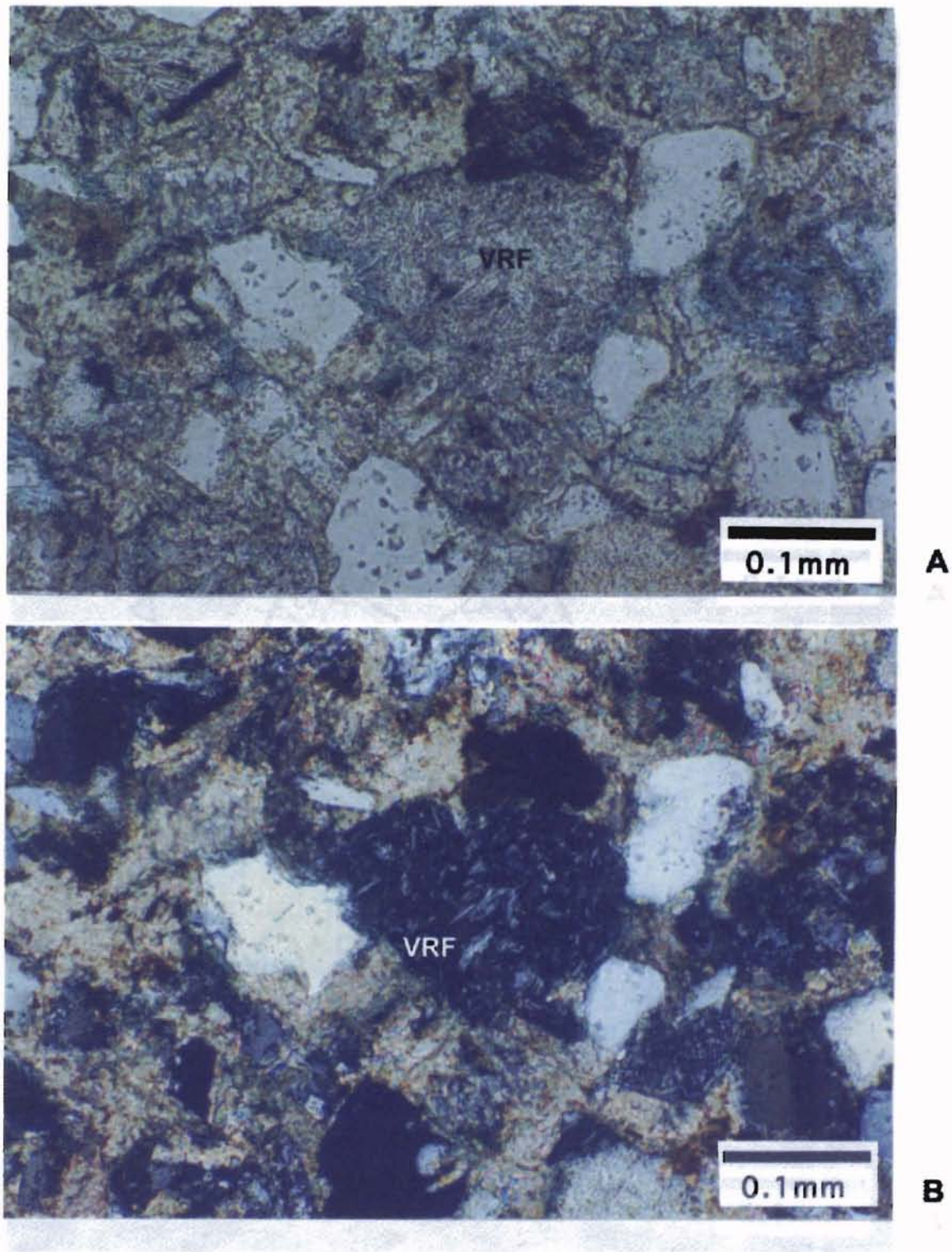

Figure 13. Photographs showing volcanic rock fragments with feldspar phenocrysts. A. × 200 PPL. B. × 200 XN.

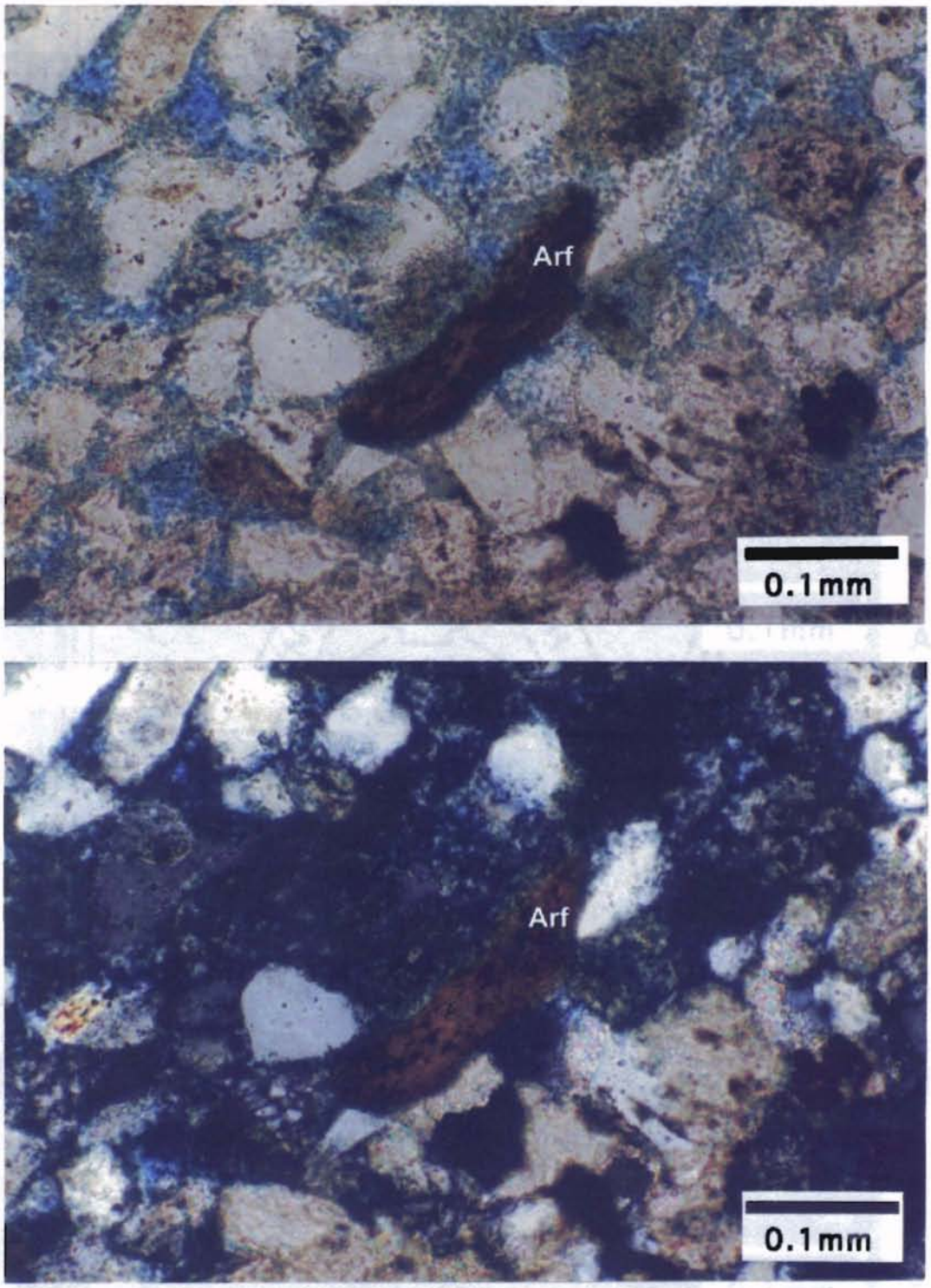

Figure 14. Phtographs showing argillaceous rock fragment (Arf).
A. × 200 PPL. B. × 200 XN.

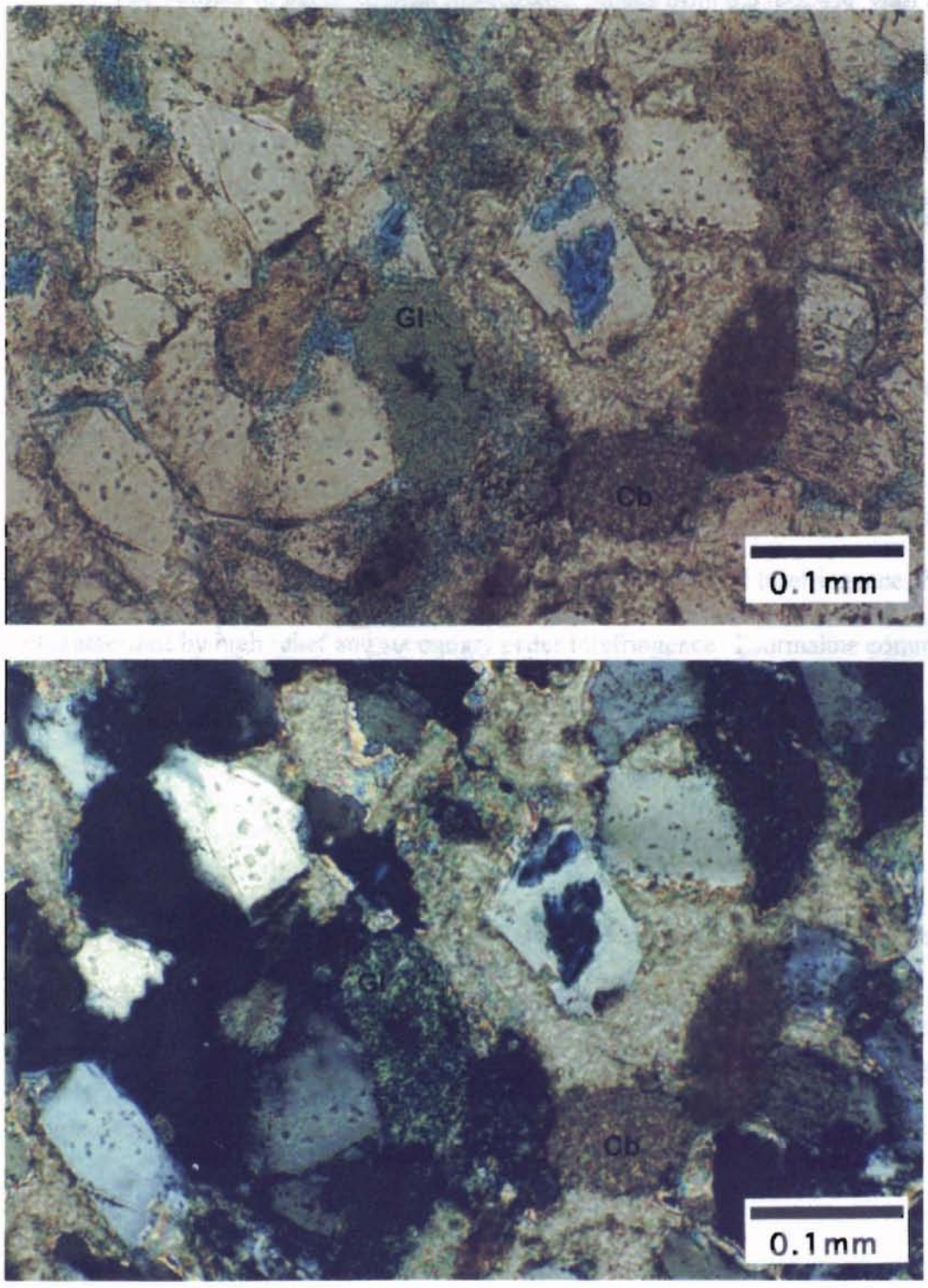

Figure 15. Photographs showing glauconite (Gl) and carbonate rock fragment (Cb).
A. × 200 PPL. B. × 200 XN.

Minor Constituents

The content of minor detrital constituents ranges from 0.3%-2.4%, with an average of 1.2 %, including glauconite, muscovite, biotite, pyrite, zircon, tourmaline and fossils.

Glauconite is a common constituent in all samples studied. It is typically round green pellets under plain polarized light and has darker green birefringence under cross-polarized light (Figure 15). Some of the glauconites were oxidized into brown color as seen under plain polarized light. The occurrence of glauconites is indicative of marine environment.

The other minor constituents generally occur in trace amounts. Muscovite and biotite can be easily identified by their color, shape, cleavage and birefringence. Zircon is characterized by high relief and secondary order birefringence. Tourmaline commonly has pleochroism. Fossils are mainly forams partially replaced by calcite (Figure 16).

Detrital Matrix

Detrital matrix is significant in several thin sections (Appendix B). It looks dirty and tends to occlude primary porosity greatly (Figure 17A). Some of the detrital matrix occurs in patchy area and flows around grains. It may be argillaceous rock fragments in origin and becomes pseudomatrix as a result of strong compaction (Figure 17B).

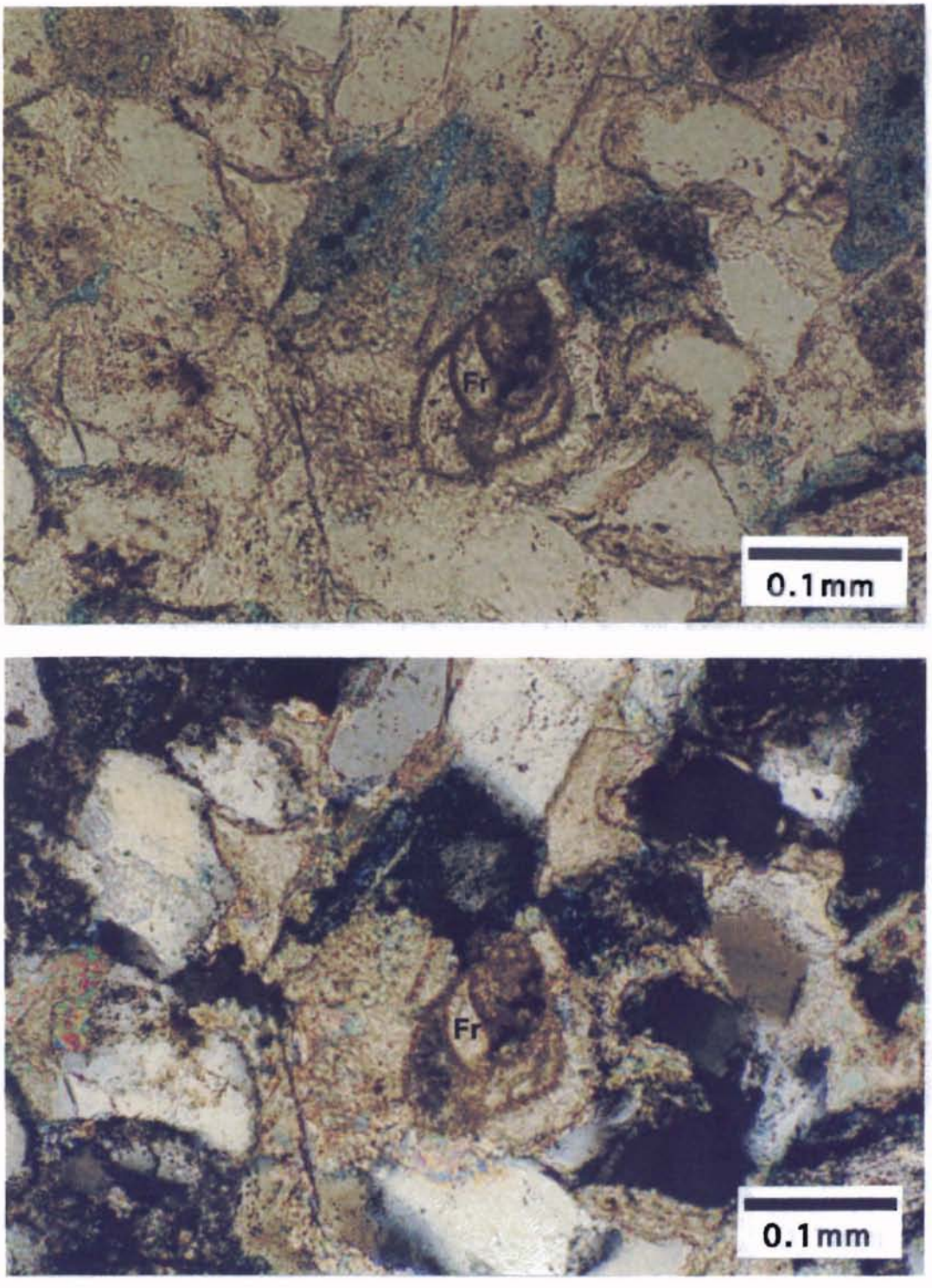

Figure 16. Photographs showing foram (Fr) replaced by calcite.
A. × 200 PPL. B. × 200 XN.

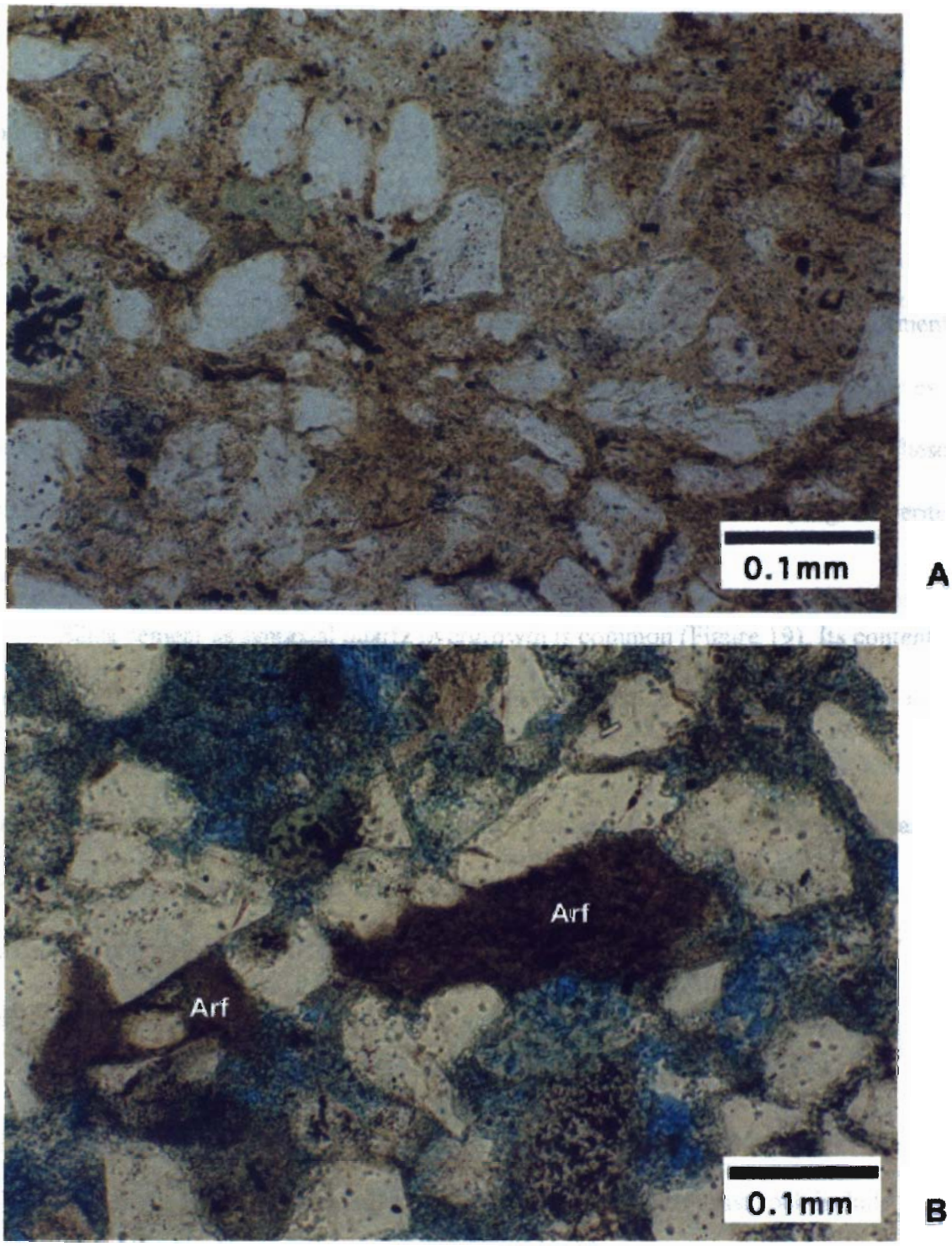

Figure 17. A. Detrital matrix nearly occluded all primary pore space. × 200 PPL.
B. Pseudomatrix flowing around rigid grains. It was formed by strong compaction of ductile argillaceous rock fragments (Arf). × 200 PPL.

Diagenetic Constituents

Vicksburg sandstones have undergone extensive diagenetic modification. The primary diagenetic products are various kinds of cements and authigenic clay.

Cements

Calcite is the major cement, with an average content of 11.8%. Carbonate cement profoundly affects the reservoir quality, commonly occluding pore space. In some zones completely cemented by calcite (Figure 18), permeability can be less than 0.01 md. These zones correspond to white color bands on Formation Micro-imaging (FMI) logs. Siderite is a minor diagenetic constituent and is present in some thin sections.

Silica cement as syntaxial quartz overgrowth is common (Figure 19). Its content varies from 0% to 4% of bulk rock composition in thin sections examined. Dust rims are commonly found to separate the syntaxial quartz overgrowth from the detrital grains. The cement appears cleaner than detrital grains since it contains less fluid inclusions. Silica cement can also drastically reduce porosity and permeability in some sandstones. Sandstones completely cemented by silica cement correspond to white zones on FMI logs.

Diagenetic Clays

Diagenetic clays documented in this low resistivity/low contrast rock include illite-smectite mixed layer clay, illite, kaolite and chlorite. They result from the direct precipitaiton from pore fluid or replacement of grain components which are mainly feldspar and volcanic rock fragments.

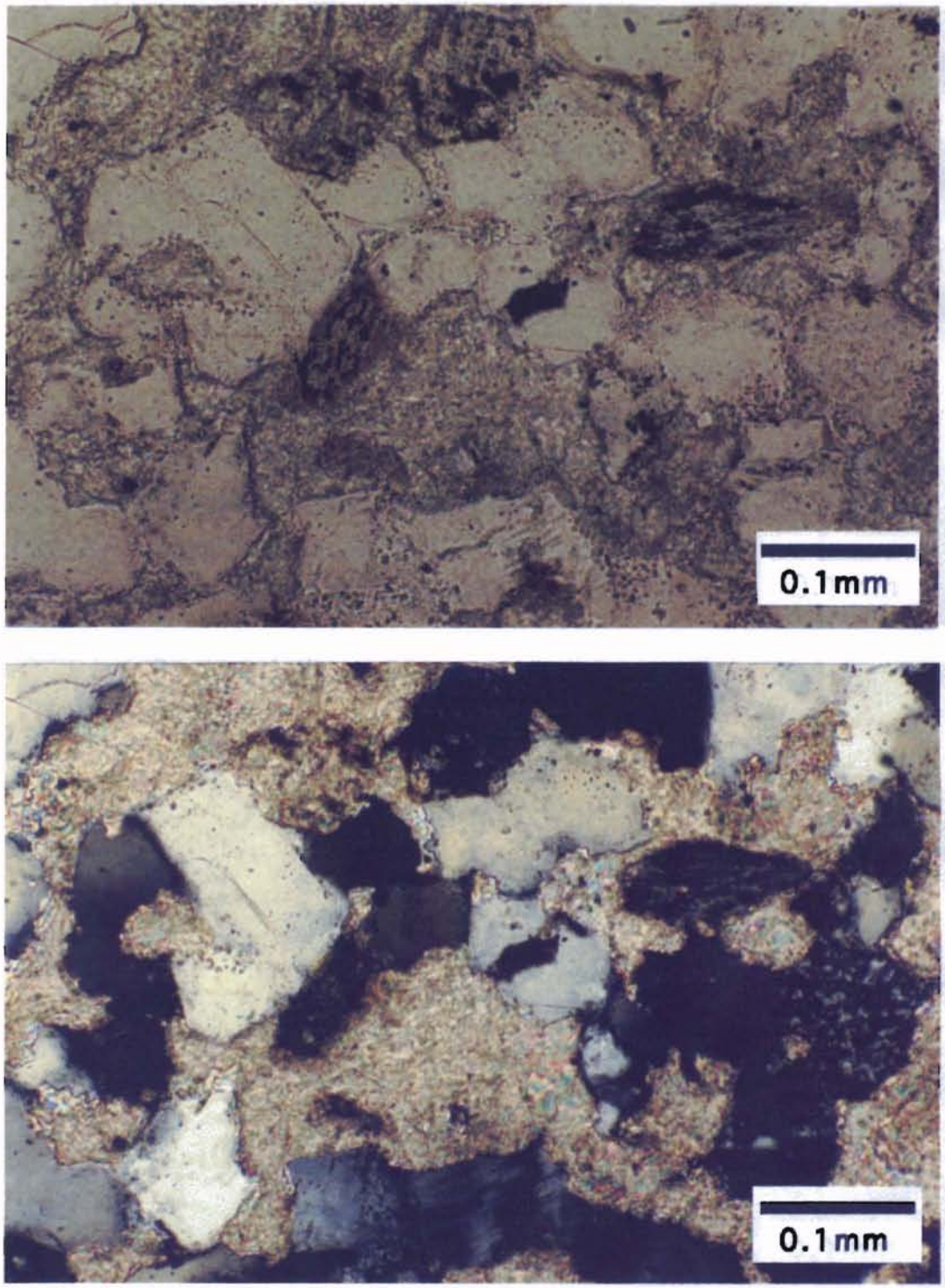

Figure 18. Photographs showing calcite cement obliterating all pore space.
A. × 200 PPL. B. × 200 XN.

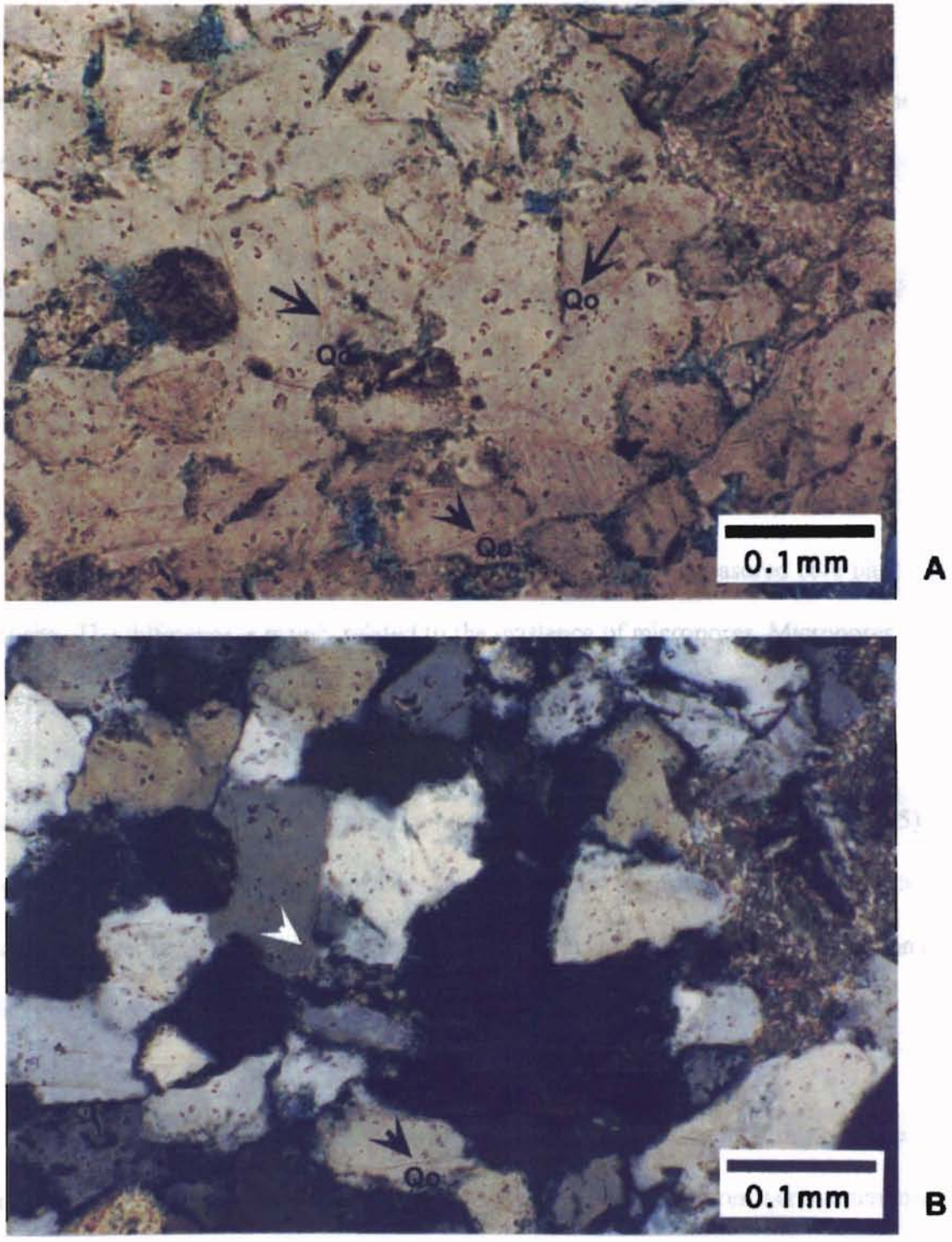

Figure 19. Photographs showing syntaxial quartz overgrowth (Qo). Dust rims (arrows) separate Qo from the detrital grains. A. × 200 PPL. B. × 200 XN.

Illite-smectite mixed layer clays are the most abundant clay mineral observed (Figure 20). These clays coat grains and fill pore space as revealed in SEM photomicrographs (Figure 21). Kaolinite is the second most abundant clay and is present in nearly all samples. It occludes secondary intergranular and/or intragranular pores (Figure 22). Chlorite is present in minor amount in nearly all samples and occurs as delicate "rosette-like" or platy crystals in SEM photomicrographs (Figure 21).

Porosity

The porosity of the thin section analysis ranges from 0.3%-15.8%, with an average of 7.1%. Thin section porosity is consistently lower than measured core plug porosity. The difference is mainly related to the existence of micropores. Micropores were not counted as pore space in point count analysis.

Porosity is predominantly secondary, and results primarily from the partial or complete dissolution of feldspar, rock fragments and calcite cement (Figure 23, 24, 25). Dissolution of quartz grains also provides some secondary porosity as suggested by the corrosion edge. Lesser amount of secondary porosity may also derive from dissolution of other constituents such as glauconite, argillaceous rock fragments, carbonate rock fragments, etc.

Pore systems are complex and variable, consisting of a mixture of intragranular (Figure 23A) and intergranular pores (Figure 23B). Intragranular pores were commonly seen in partially dissolved feldspar and volcanic rock fragments. Intergranular pores can be primary pores but are mainly secondary dissolution pores. Microporosity is another important feature in the 9900-ft sandstone as observed under microscope and by SEM

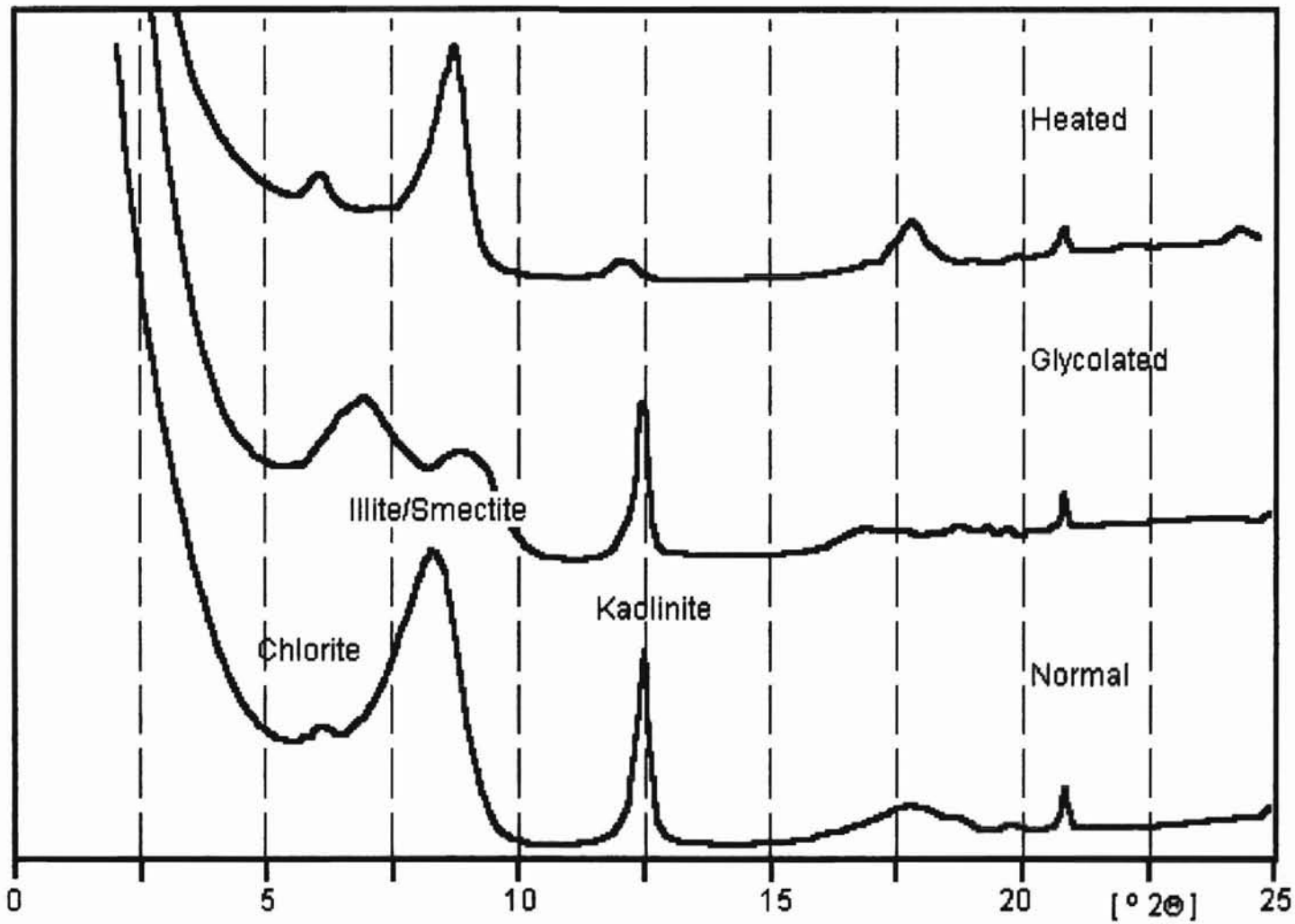

Figure 20. X-ray diffractogram of clay components in 9900-ft zone. Illite-Smectite mixed layer clay is the most predominant clay type.

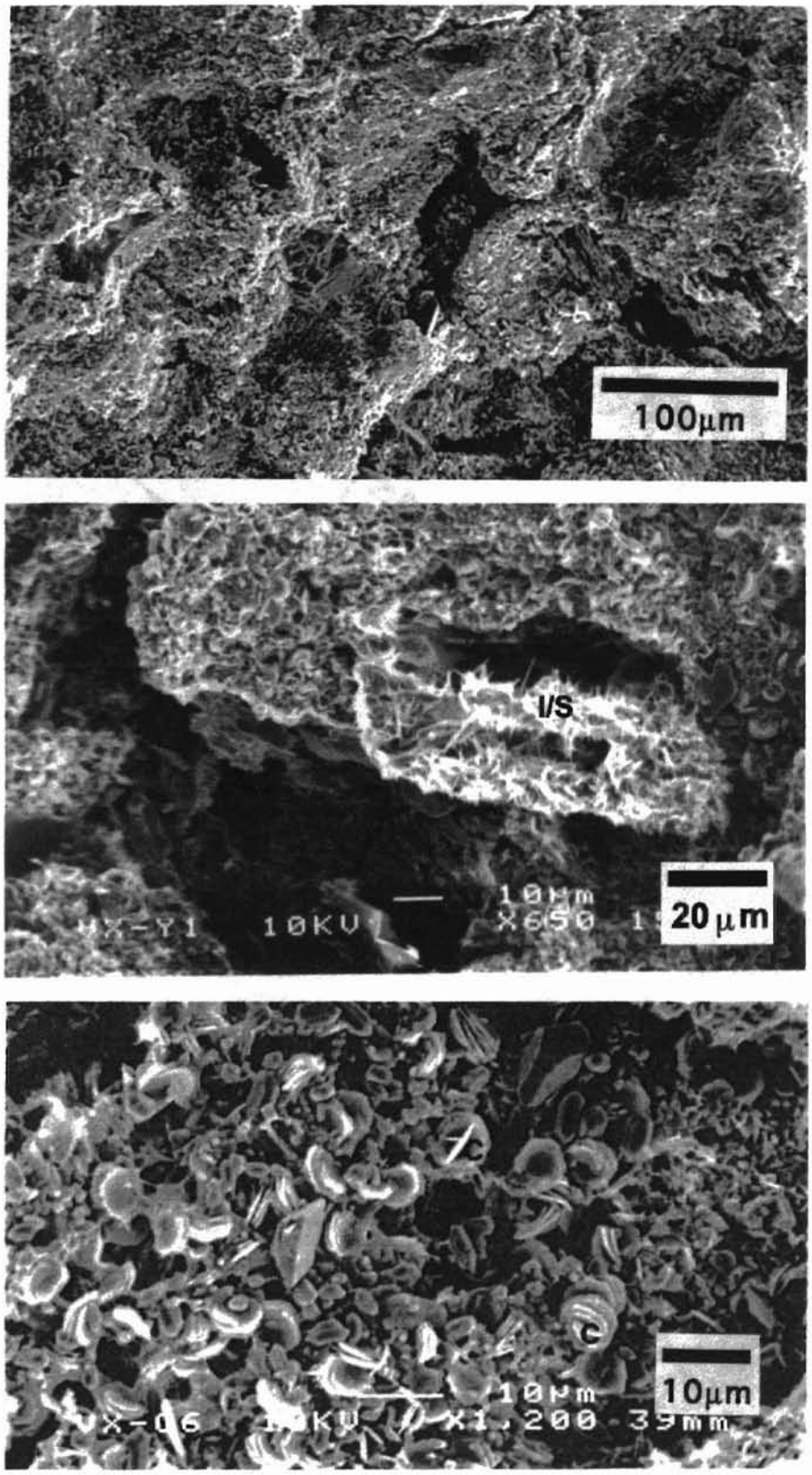

Figure 21. Scanning electron photomicrograph showing illite-smectite mixed layer clay (I/S) and chlorite (C).

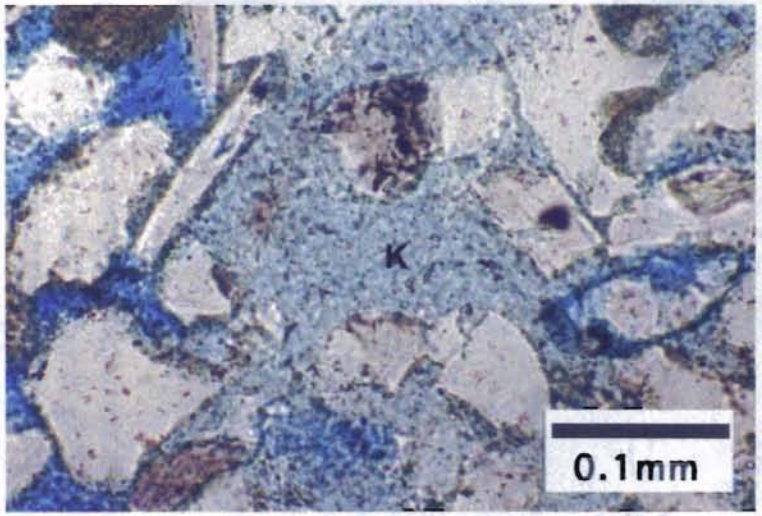

A

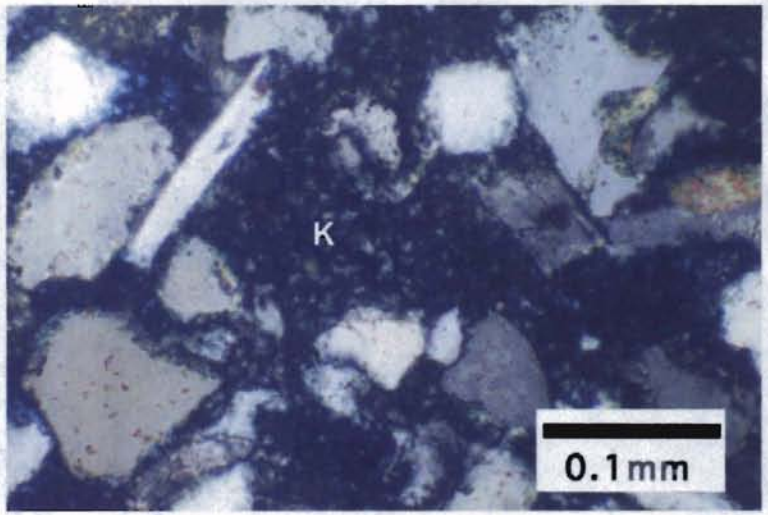

B

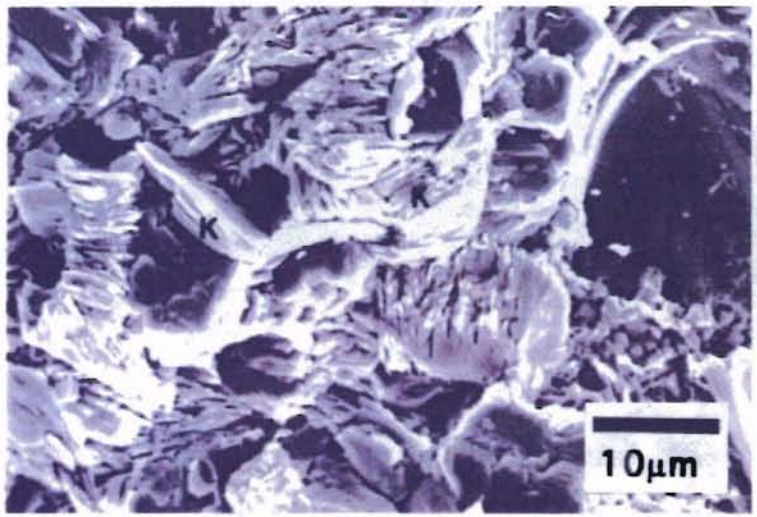

C

Figure 32. Authigenic kaolinite (K) occupying secondary pores.
A. Thin section photograph ×200 PPL.
B. Thin section photograph ×200 XN.
C. Scanning eletron photomicrograph.

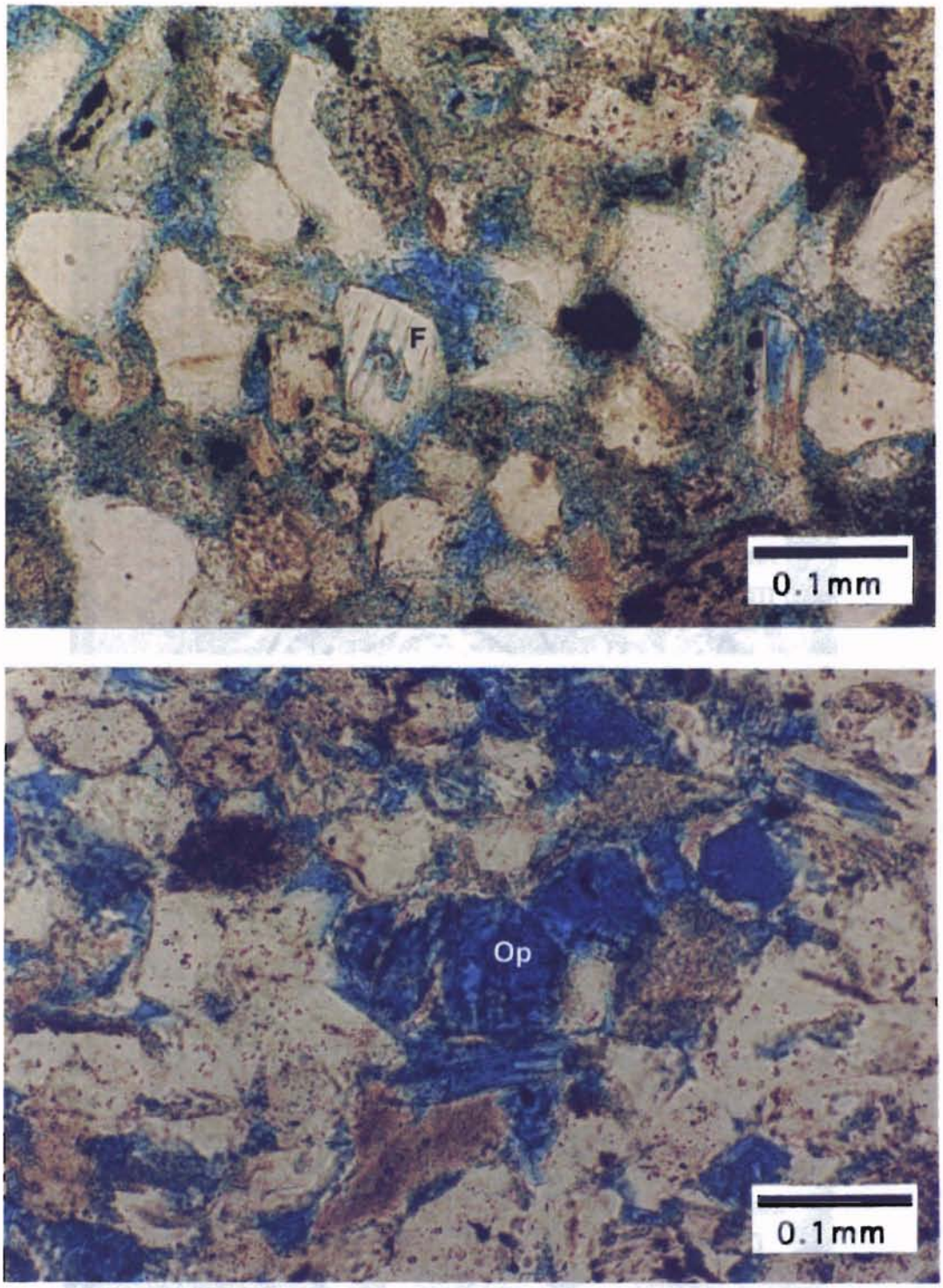

Figure 23. Secondary porosity from the dissolution of feldspar (F). A. Intragranular pores indicating initial partial dissolution of feldspars. × 200 PPL.
B. Oversized pore from nearly complete dissolution of feldspar. Faint feldspar remnants can still be identified. × 200 PPL.

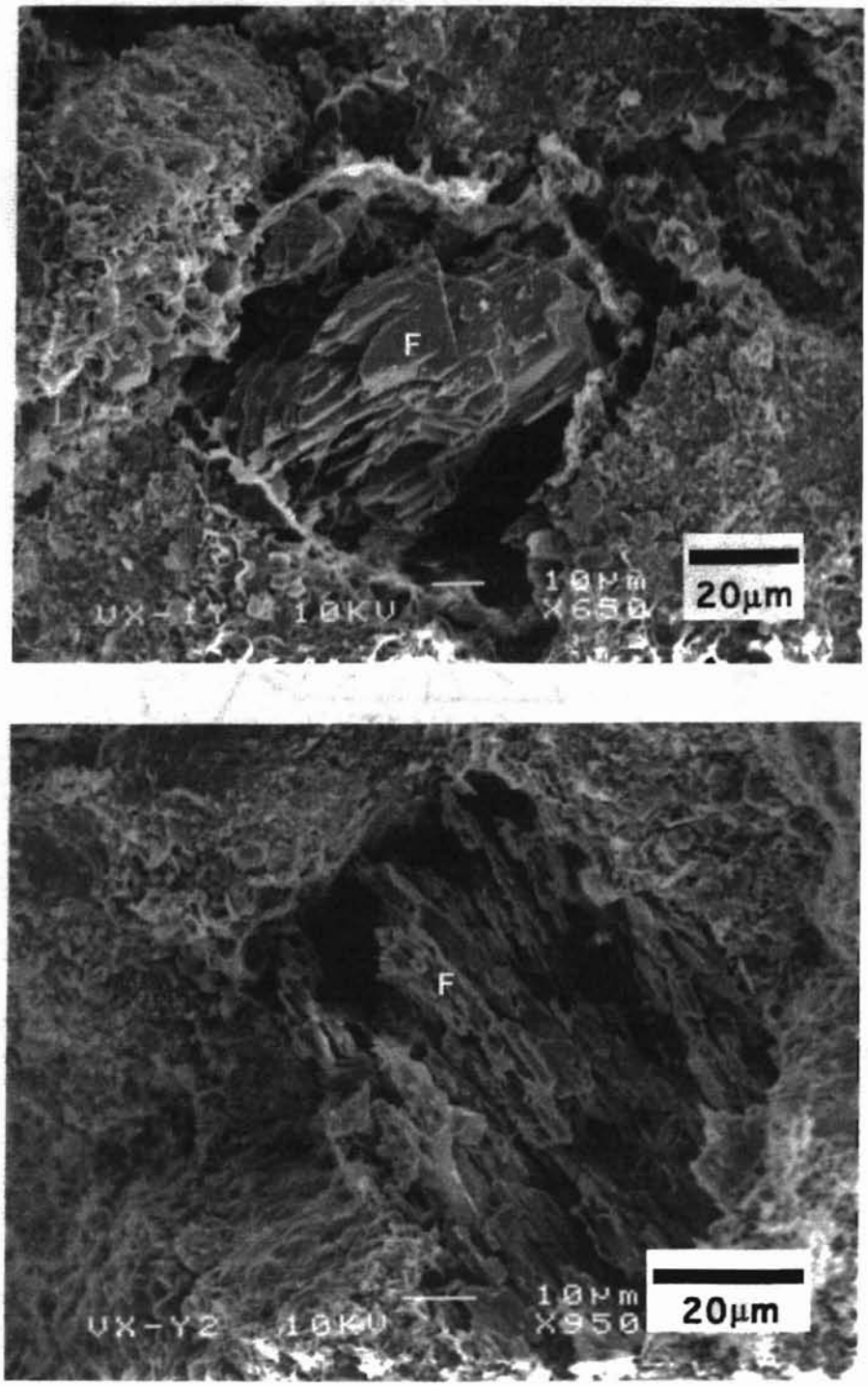

Figure 24. Scanning electron photomicrograph showing the dissolution of feldspar (F).

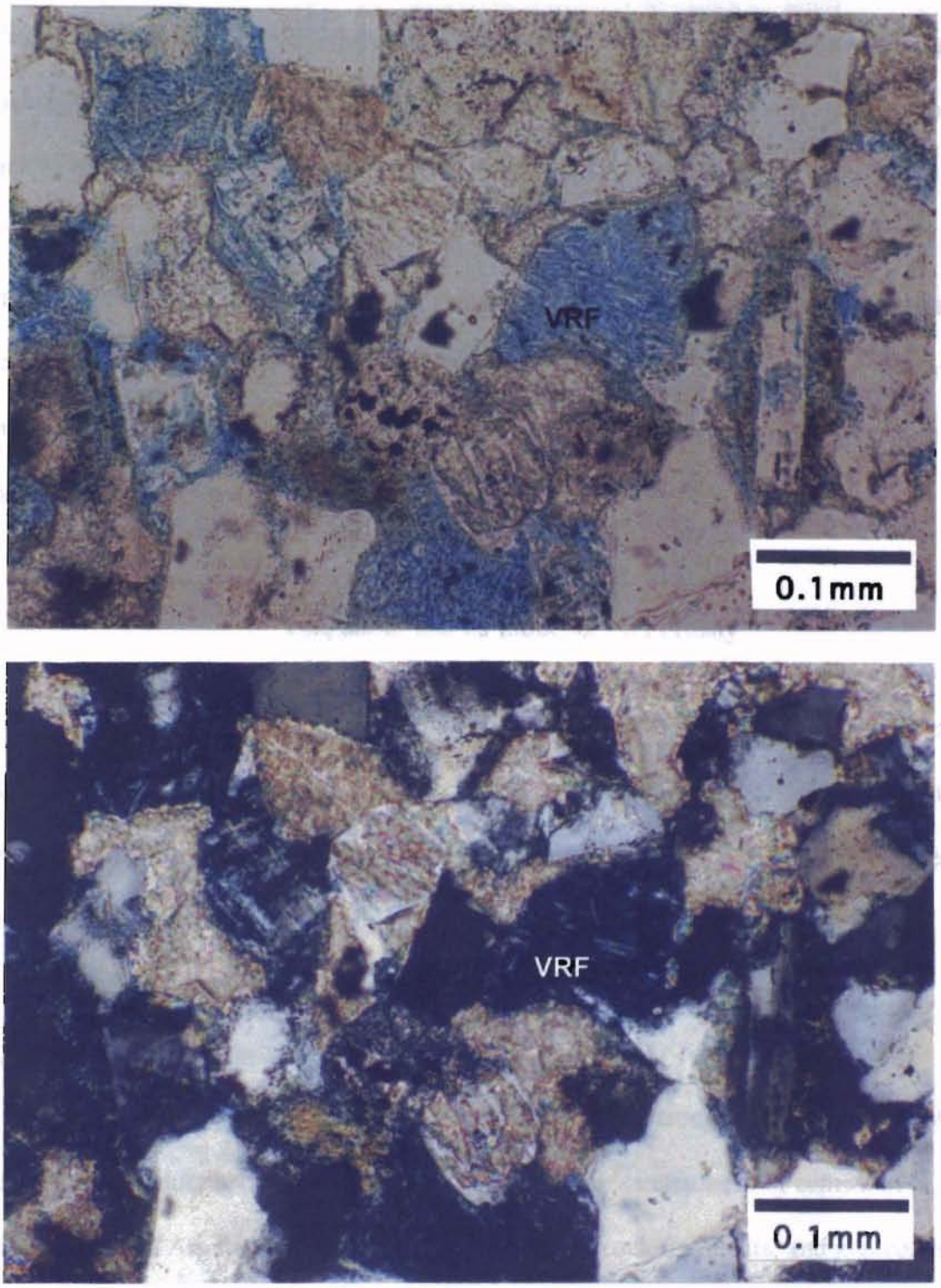

Figure 25. Photographs showing dissolution of volcanic rock fragments (VRF). The relict VRF can be identified by the randomly oriented feldspar laths.
A. × 200 PPL. B. × 200 XN.

analysis. Micropores develop between clays or in partially dissolved grains (Figure 26). Clay microporosity occurs not only in dispersed clays but also in detrital grains. In the Vicksburg sandstones, a variety of detrital grains are clay-rich and contain microporosity such as altered volcanic rock fragments, argillaceous rock fragments and glauconite. These intercrystalline micropores generally have small pore throat radii (less than 0.5 microns) and significantly reduce permeability. In clay-rich zones, micropore system and macropore system can coexist. The former is basically ineffective to capture hydrocarbon but can provide path for electrical current. The latter contributes to the major storage space for hydrocarbon.

Diagenesis and its Influence on Porosity

The original depositional fabric of 9900-ft zone was severely altered by various diagenetic processes. The primary diagenetic processes include: mechanical deformation, leaching of detrital grains and calcite cement, and precipitation of calcite cement, silica cement and authigenic clays.

Compaction and Mechanical Deformation

Vicksburg sandstones have undergone moderate to strong degrees of compaction. Deformation of ductile components was characteristic in sandstones not cemented in early diagenesis. Argillaceous rock fragments, volcanic rock fragments, and glauconite were squeezed between quartz, feldspar and other hard grains (Figure 17B), accentuating the compaction and correspondent decrease in porosity. Elongate muscovite and biotite grains were bent or contorted (Figure 27).

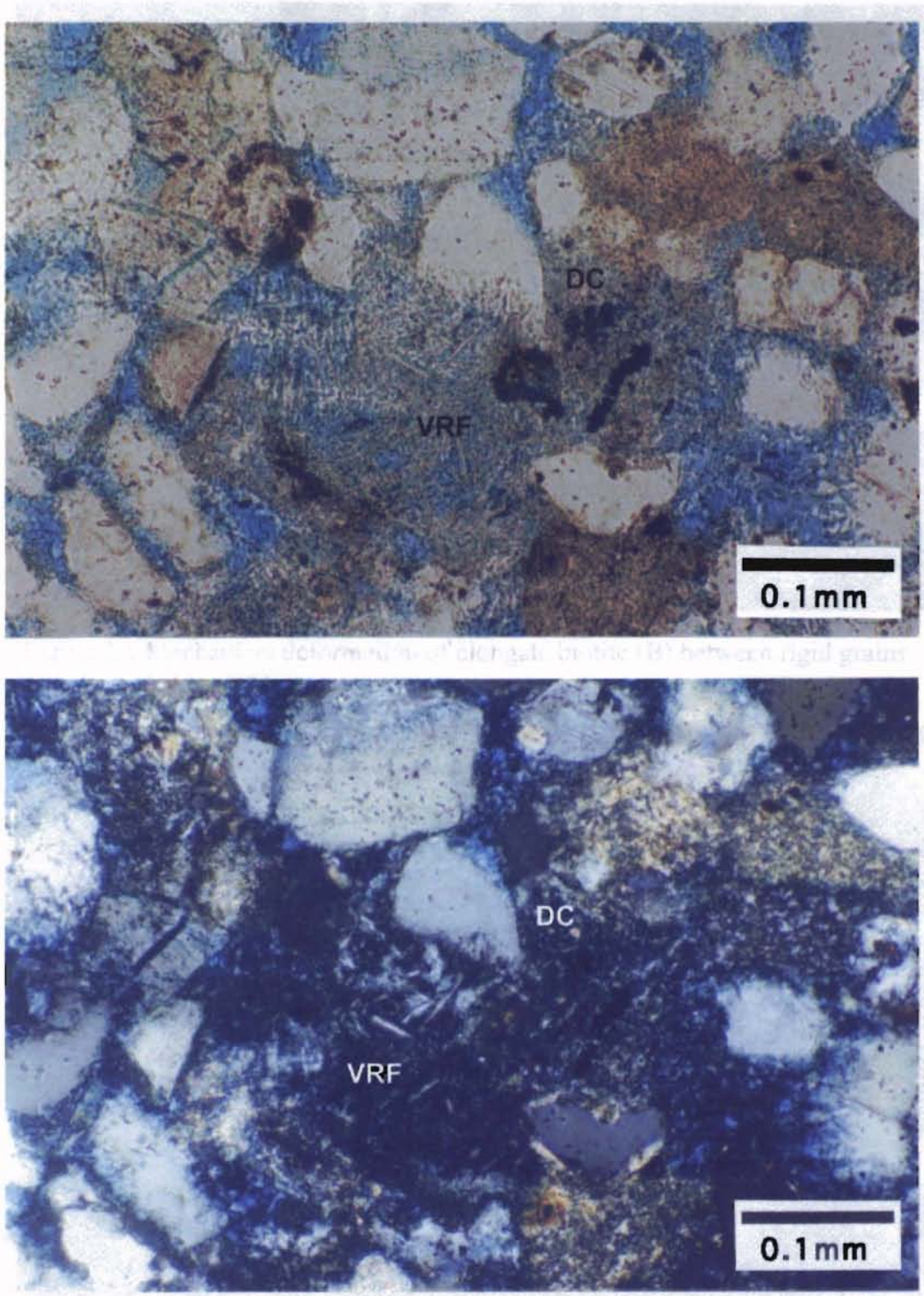

Figure 26. Microporosity in dispersed clays (DC) and clay-altered volcanic rock fragment (VRF). A. × 200 PPL. B. × 200 XN.

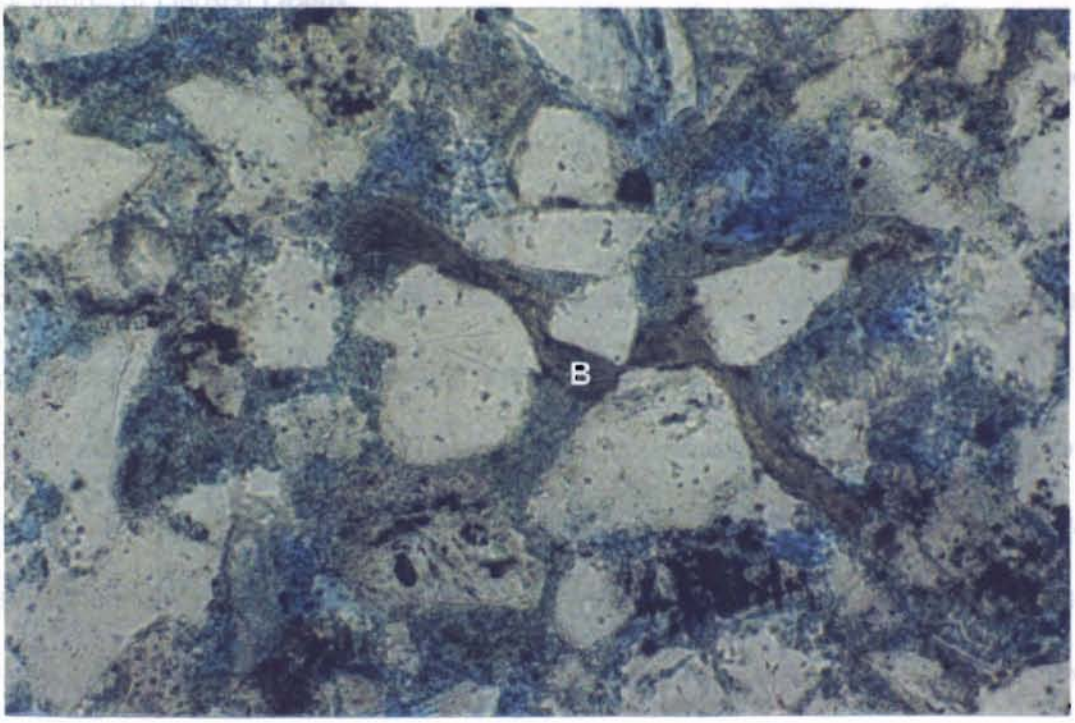

Figure 27. Mechanical deformation of elongate biotite (B) between rigid grains. ×200 PPL.

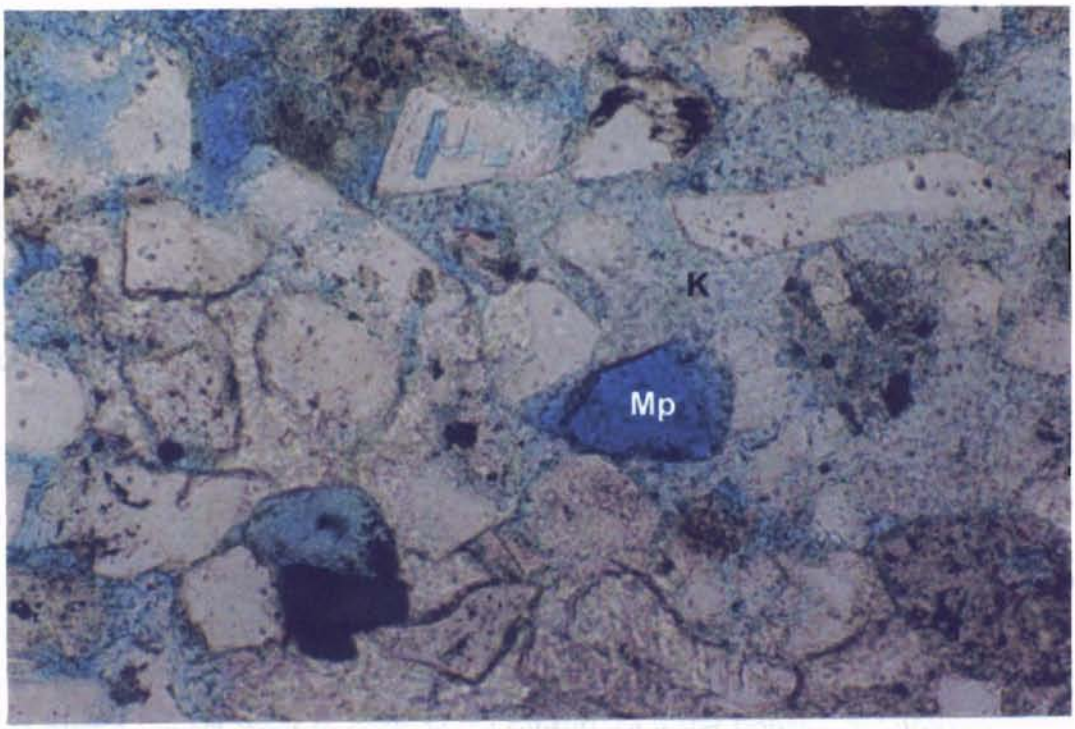

Figure 28. Photograph showing moldic pore (Mp). Surrounding kaolinte (K) was precipitated prior to grain dissolution. ×200 PPL.

Dissolution of Detrital Grains

Dissolution of detrital grains is essential for reservoir development in the studied 9900-ft sandstones. The dissolution of quartz grains may have initiated early and is associated with the formation of early calcite cement. However, the major dissolution accounting for reservoir development took place with further burial, where H^+ rich fluid was generated in response to thermal evolution of organic matter. The subsequent leaching of unstable detrital grains (feldspar, volcanic rock fragments, etc.) and carbonate cement can form abundant secondary porosity. Products of multiple stage leaching were observed under microscopes. Initial leaching generated some intragranular micropores in detrital grains (Figure 23A). With the further leaching, intergranular macroporosity were generated. Moldic and oversized pores suggest the complete leaching of metastable grains (Figure 23B, 28). Dissolution of detrital grains is not evident where clay matrix exists. In this case, porosity is also very low.

Dissolution of detrital grains provided both space and the source material for the precipitation of authigenic clays and late stage calcite cement.

Precipitation of Cement and Authigenic Clay

Calcite cements were formed in two stages. Early stage calcite cement may develop before major compaction. This is suggested by reduced mechanical deformation of ductile grains among early calcite "matrix". Quartz grains show apparent corrosion features and replacement by early calcite cement. The extensive development of early stage calcite cement tends to occlude the subsurface water flowing and protecte chemically unstable constituents from being leached in the early stage of dissolution. Other diagenetic processes, such as sericitization and precipitation of authigenic clays are

also slowed. Therefore, volcanic rock fragments and feldspars floating in the early stage calcite cement generally have fresh surfaces (Figure 29).

The subsequent dissolution of the early calcite cement can generate large amount of secondary pore space. These secondary pore space were then lined or filled by authigenic clays.

The next stage cementation was the local precipitation of quartz overgrowth on relatively "cleaner" quartz grains (Fig 19). Dust rims are commonly found to separate the syntaxial quartz overgrowth from the detrital grains. In areas with little clays, quartz overgrowth can completely occlude the pore space.

A second episode of calcite cementation is also quite common as suggested by apparent chemical alteration of detrital grains and replacement of quartz overgrowth by calcite cement (Figure 30). This late calcite cement should form after the formation of quartz overgrowth. Late stage calcite occurs as pore-filling cement and grain replacement.

Diagenetic clays are important component in porous sandstones of the studied 9900-ft zone. They occur as the direct precipitation from pore fluid or as the replacement of pre-existing components. The former type of clays is related to multiple-stage dissolution since these authigenic clays are found in secondary intragranular or enlarged intergranular pores (Figure 31).

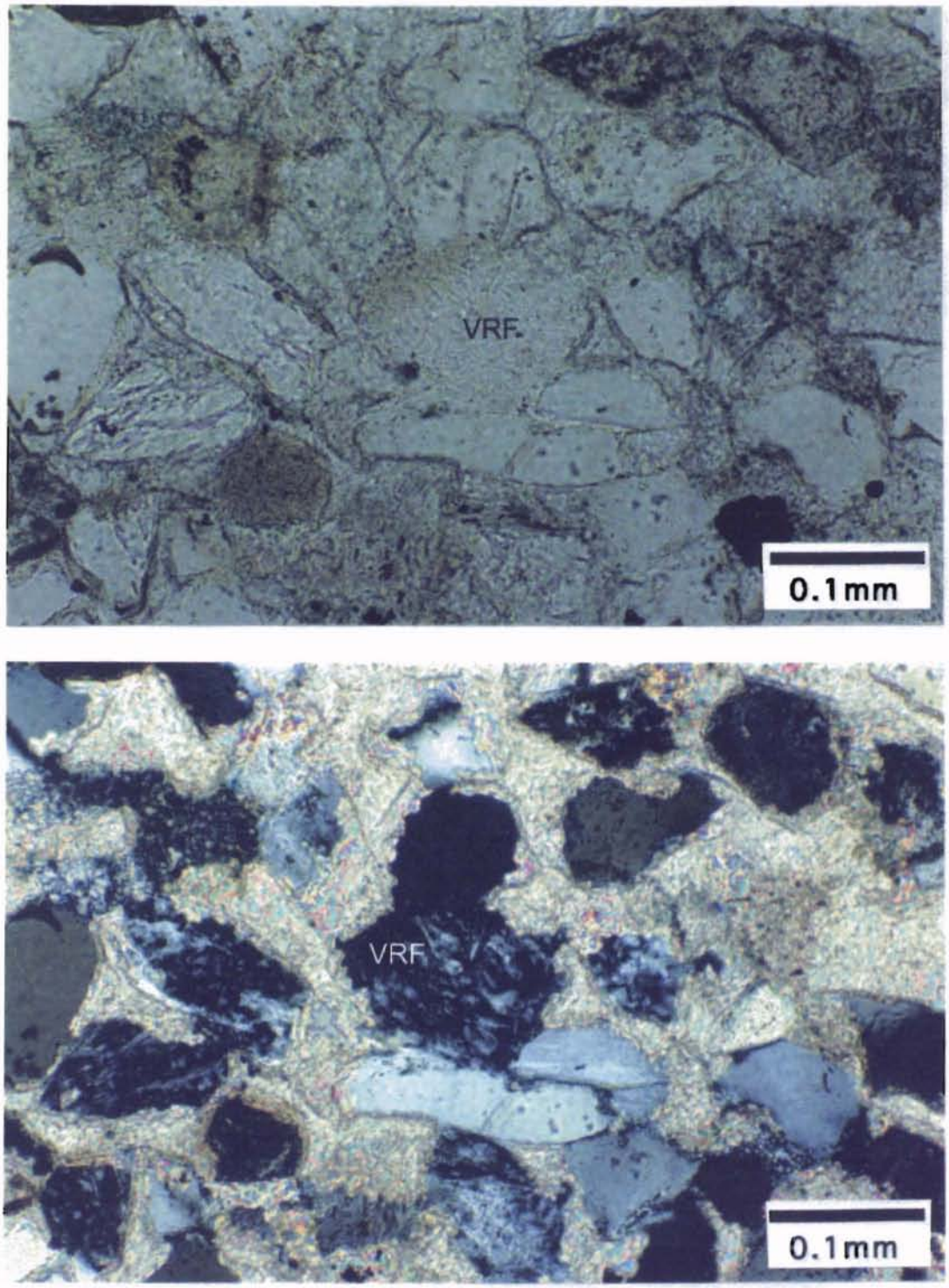

Figure 29. Photographs showing early stage calcite cement. Volcanic rock fragment (VRF) has little alteration. A. × 200 PPL. B. × 200 XN.

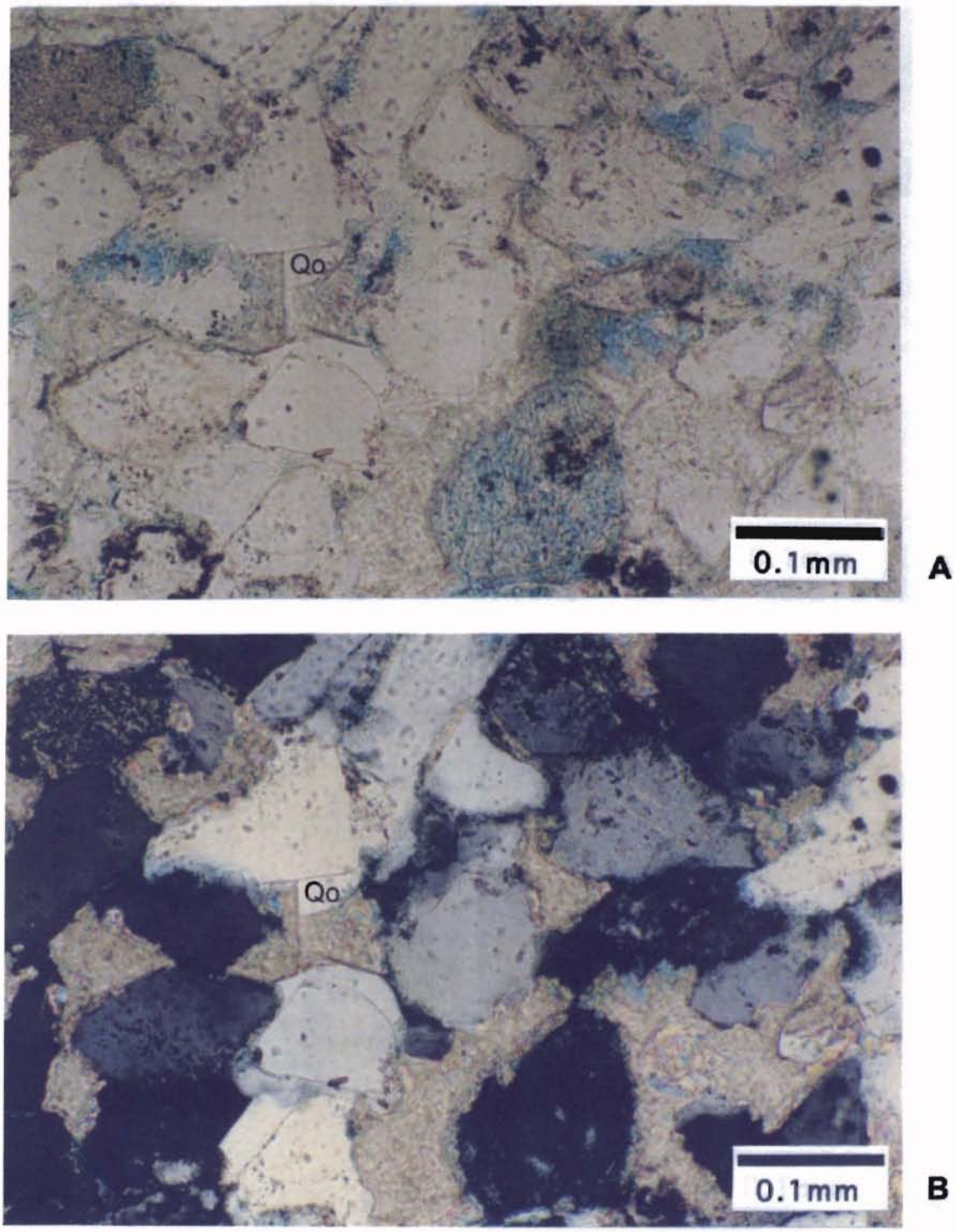

Figure 30. Photographs showing late stage calcite cement indicated by apparent alteration of detrital grains and calcite replacement of quartz overgrowth (Qo).
A. × 200 PPL. B. × 200 XN.

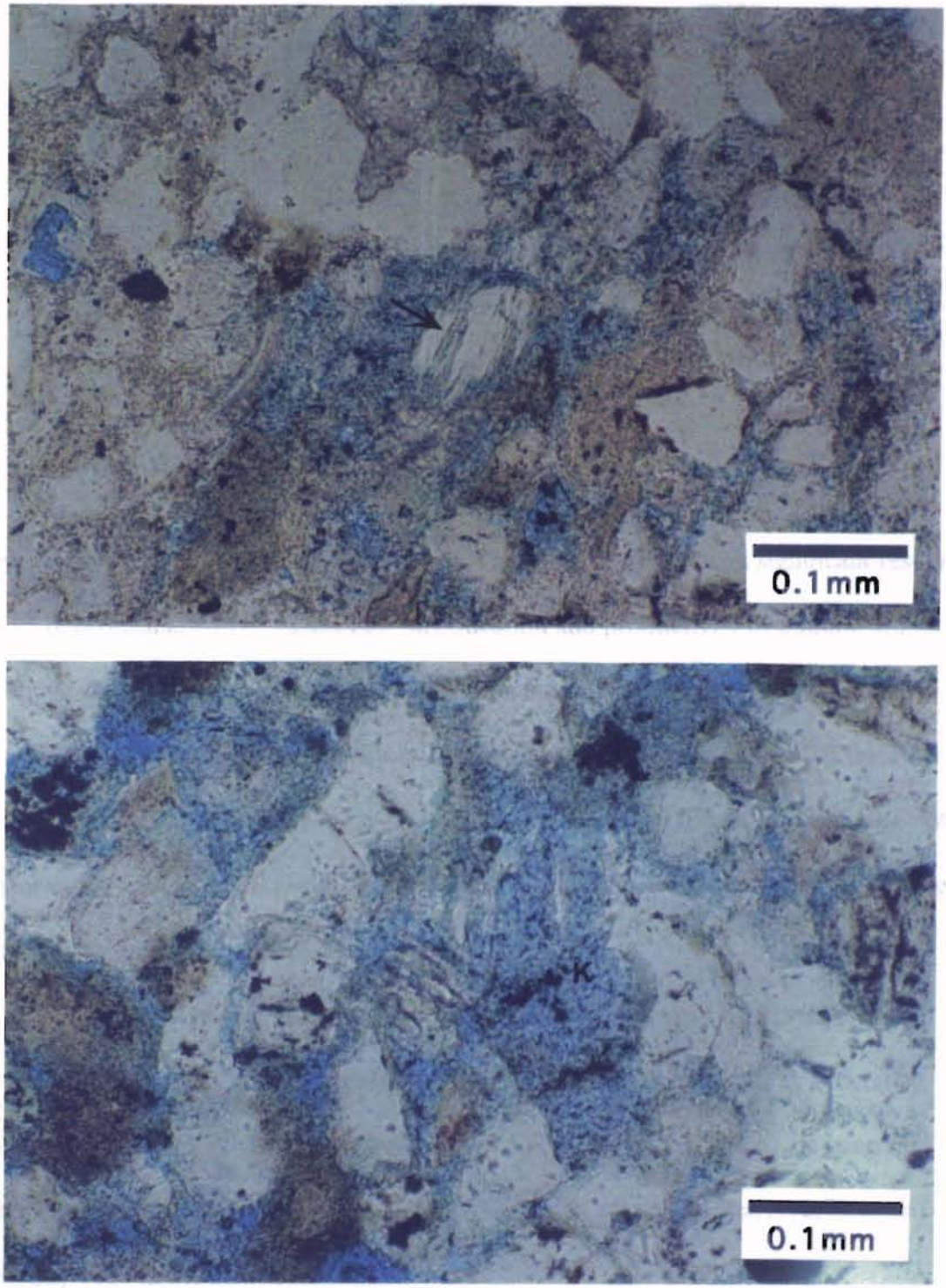

Figure 31. Photographs showing authigenic clays in secondary pore spaces.
A. Intragranular pore filled with authigenic clays. × 200 PPL.
B. Enlarged intergranular pore (EIP) filled with kaolinite (K). × 200 PPL.

CHAPTER IV

PETROPHYSICAL ANALYSIS

General Statement

Low-contrast thinly bedded/laminated oil and gas reservoirs are becoming increasingly important exploration targets. These reservoirs contain significant reserves, but are problematic in that reservoir identification and productivity evaluation are difficult. The high content of detrital and authigenic clays in these rocks causes considerable decreases in resistivity. Many sandstone beds are less than 1-ft thick and laminated with shales, which are beyond the resolution limit of most wireline logs. Water saturations determined using most water saturation calculation equations are very high for low-contrast thinly bedded and laminated reservoirs.

Recent technological advances in logging have improved interpretation and evaluation of LR/LC zones. High-resolution resistivity and porosity logs accurately represent rock properties in beds thicker than 1-foot. Formation micro-imaging logs (Formation MicroImager) (Schlumberger)/(Electrical Micro Imaging) (Halliburton) can identify beds to the inch scale.

The productivity of the studied 9900-ft Vicksburg sandstone zone was evaluated using an integrated approach involving detailed core analysis, production data and

various petrophysical methods. Wireline logs were correlated to other data to evaluate the effectiveness of various tools in determining lithology and measuring rock/pore fluid properties in shaly sandstones. The results indicated that core-calibrated micro-imaging logs could effectively detect reservoir and sealing facies in those low-contrast thin-bedded intervals. The correlation of FMI to high-resolution logs can improve recognition of reservoirs and non-reservoirs. Water saturations across LR/LC reservoirs were calculated using a variety of methods, including conventional Archie, Modified Archie, Waxman-Smits, Dual-Water, Modifed Dual-Water, Modified Simandoux and Indonesia equations. Calculated water saturation values were compared to those from core derived analyses. The best fit of log calculated and core measured water saturation values was achieved using Modified Archie, Waxman-Smits and Modified Dual-Water methods.

Core Analysis

Core analyses provided petrophysical measurements which include porosity, permeability, grain density and saturations of water, gas and oil. The core analysis was conducted by Core Laboratories, Inc., Houston, Texas. Core porosity is measured at 5360 psi overburden pressure.

Core porosity and permeability vary for different chromatic zones identified in Formation Micro-imaging logs (Al-Shaieb et al., 2000).

A crossplot of core derived porosity versus core derived permeability is shown in Figure 32. White, yellow and orange zones are plotted in three distinct areas. White zones have low porosity and permeability. Yellow zones have the highest porosity and permeability and represent reservoir facies. Orange zones have high porosity, but

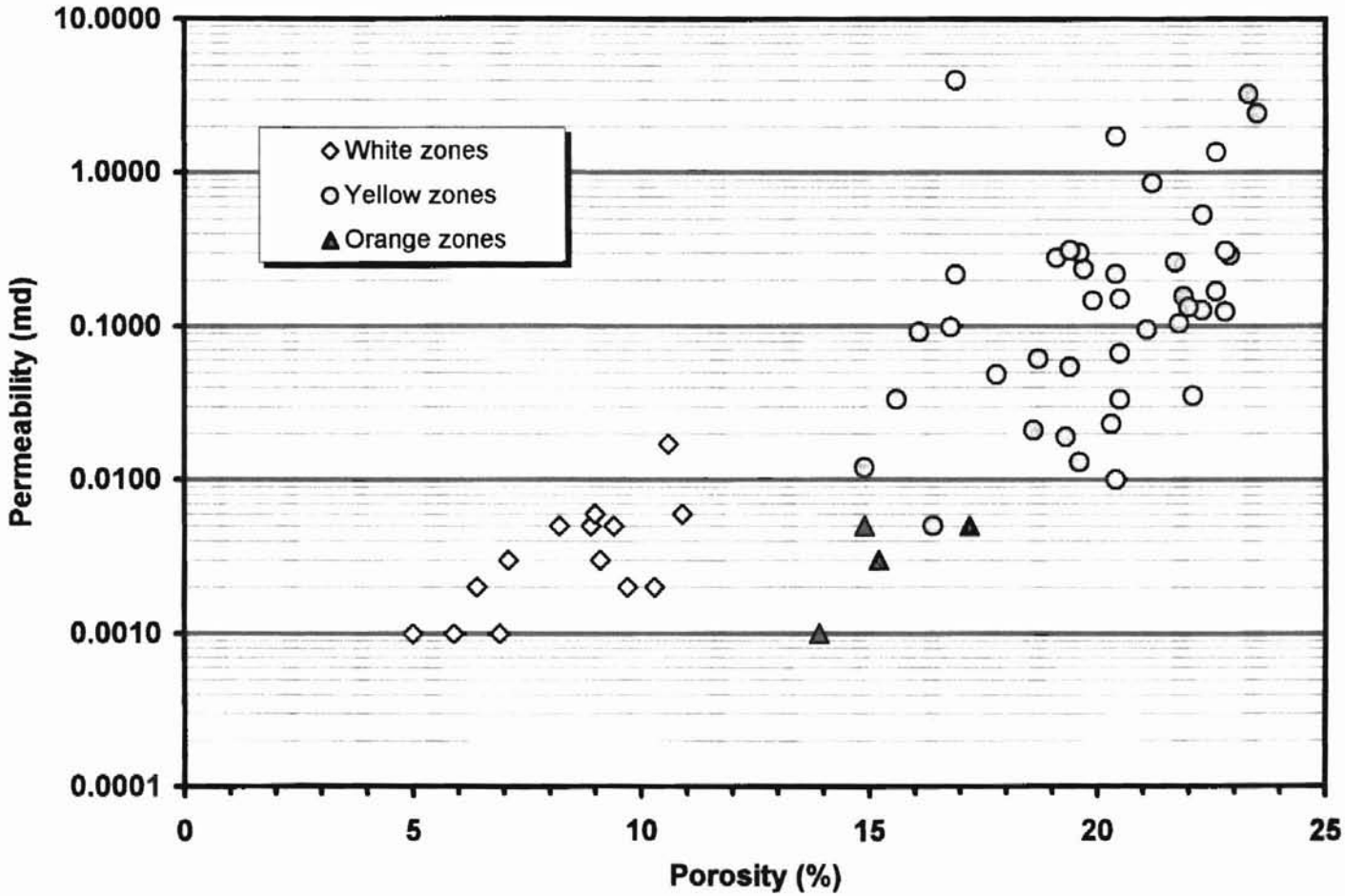

Figure 32. Crossplot of porosity and permeability. Note that all the permeability data greater than 0.1md are from yellow zones.

permeability tends to be low. Besides, yellow zones show a general increase of permeability with porosity. Permeability reflects the interconnectivity between pores in the rock and is a function of dissolution stage, since pore spaces are predominantly secondary dissolution pores. Permeability increases with the conversion from intragranular pores or moldic pores to enlarged intergranular pores.

Capillary Pressure Analysis

Capillary pressure is considered as the amount of pressure required to force the non-wetting phase to displace the wetting phase. Capillary pressure data can be used to evaluate the pore structure of the rock (Thomeer, 1960), determine the height of hydrocarbon column above the free water level and predict the seal capacity and reservoir quality (Vavra, et al., 1992).

Data Processing

Capillary pressure data was obtained through mercury injection of rock chips. Resultant data give injected mercury volume as a function of pressure. To apply these data to reservoir condition, mercury injection pressure in mercury/air system (Pcma) was converted to capillary pressure in gas/water system (Pcwg).

$$Pcwg = Pcma \times (\sigma_r \cos \theta_r)/(\sigma_l \cos \theta_l) \qquad (4\text{-}1)$$

σ_r and σ_l are the interfacial tensions of the gas/water and mercury/air systems, respectively and θ_r and θ_l are the contact angles of the gas/water and mercury/air systems, respectively. Most commonly, σ_l, θ_r and θ_l are assumed to be 480 dynes/cm, 0° and 140°, respectively (Vavra, et al., 1992). σ_r varies with the formation pressure, temperature and

hydrocarbon properties. The selection of σ_r is based on the study by Schowalter (1979, Figure 12) and 25 dynes/cm is used in this study.

The gas column height (H) can then be calculated as follows:

$$H = Pcwg/(0.4335\ (\rho_b-\rho_{hc})) \quad (4\text{-}2)$$

ρ_b and ρ_{hc} are the densities of brine and gas under reservoir condition, respectively. In addition to chemical composition, density is also a function of formation temperature and pressure. For the studied 9900-ft zone, ρ_b and ρ_{hc} are estimated to be 1 gm/cc and 0.295 gm/cc respectively (Personal Communication, Jay Patchett, 2000).

Mercury saturation is used to reflect the non-wetting phase saturation which is gas saturation in this study. Mercury saturation is calculated by dividing the normalized mercury volume by the total pore space per gram of rock. The normalized mercury volume is the injected mercury volume per gram of rock. The total pore space per gram of rock (Vb) is calculated by

$$Vb = Vmax + Vwb \quad (4\text{-}3)$$

$$Vwb = 0.25 \times CEC \quad (4\text{-}4)$$

Vmax is the maximum normalized mercury volume. Vwb is the volume of clay bound water per gram of rock, which is assumed not to have been removed at the drying temperature. Before mercury injection, samples were dried at 105 °C for 24 hours to remove all waters from pore space. However, some investigators believe that drying temperature on the order of 105°C for 24 hours can only remove all of the free pore water while leaving most of the clay bound water (Cebell and Chilingarian, 1972; Personal Communication, Jay Patchett, 2000). The amount of remaining clay bound water in studied samples can not be ignored as suggested by average cation exchange capacity

(CEC) values in yellow zones (0.09meq/gm rock). Therefore, Vwb must be considered in estimating total pore space (Vb).

Height of Gas Column above the Free Water Level

The height of gas column above the free water level is determined by comparing capillary pressure data with measured core water saturation (Vavra, et al., 1992). In this study, the height above the free water level is the gas column height at core water saturation (core_Sw). One example is shown in Figure 33.

Figure 34 shows the height above free water level versus subsea depth. Different colors are used to represent the variation in core porosity. The average height above the free water level can be determined for relative porous zones ($\phi > 10\%$), which is around 300 feet. Height above free water level is much higher for tight zones with ϕ between 5% to 10%. This is especially apparent for the tight point from A. T. Canales 81 (sample 81-41). Its height above free water level is around 1340 feet. Since the total cored interval of A. T. Canales 81 is only 43 feet and the structure closure is around 600 feet, the enormous variation in the height above free water level is interpreted to be generated by core_Sw errors in tight zones. In tight zones, water saturations should be higher than those from porous reservoir zones and tight zones may still have some relative permeability to water. When the core is brought to surface, some water will be expelled from the tight high water saturation zones having some relative permeability to water. As a result, the core water saturation measured is lower than the subsurface original water saturation. For example, based on the average height of 300 feet, water saturations can be

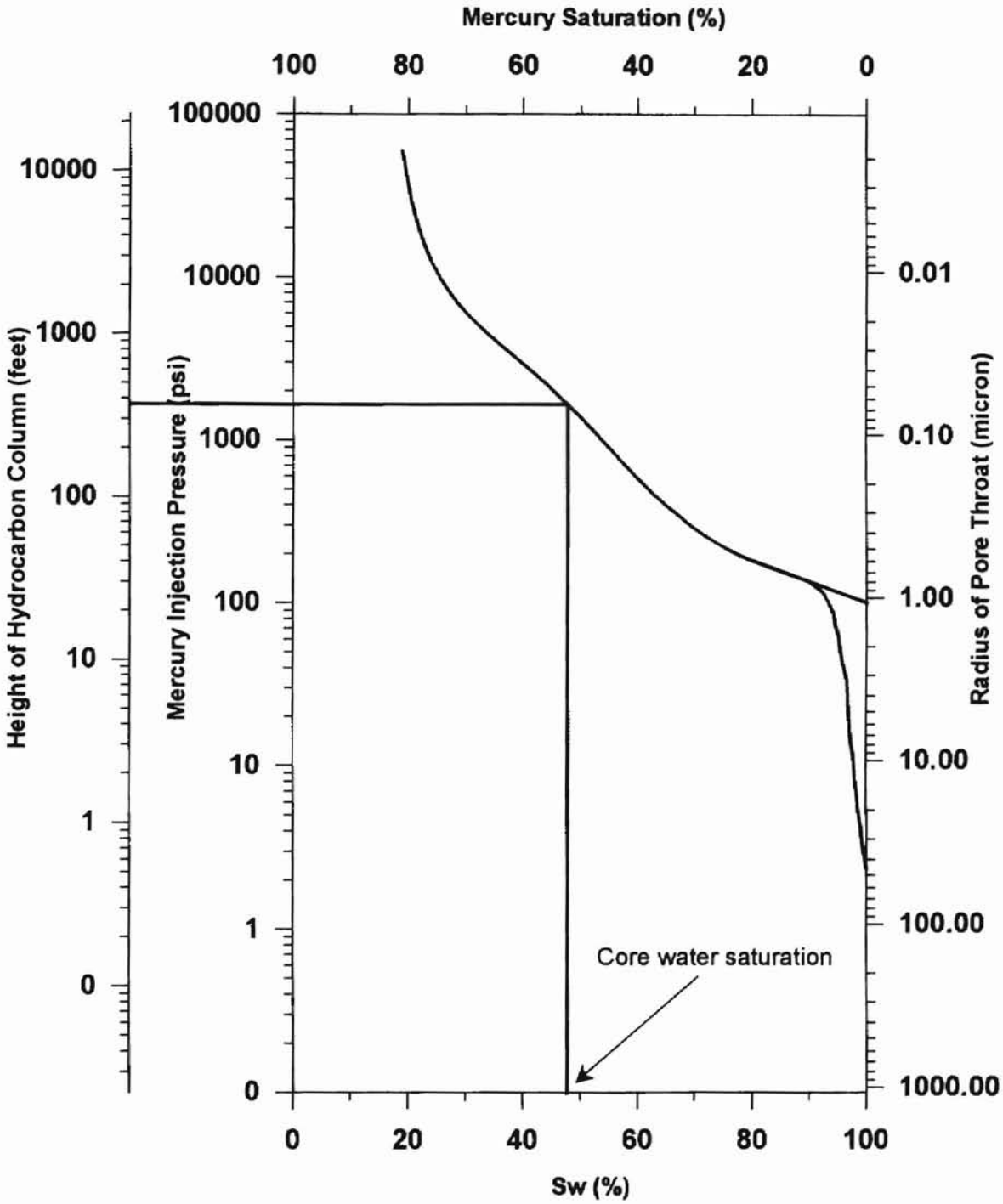

Figure 33. Capillary pressure curve for sample 85-46. Water saturation from core measurement is 47.6% for this sample and the corresponding height above free water level is 370 ft. Displacement pressure estimated by extending the slope of the plateau to 100% Sw is 100.6 psi.

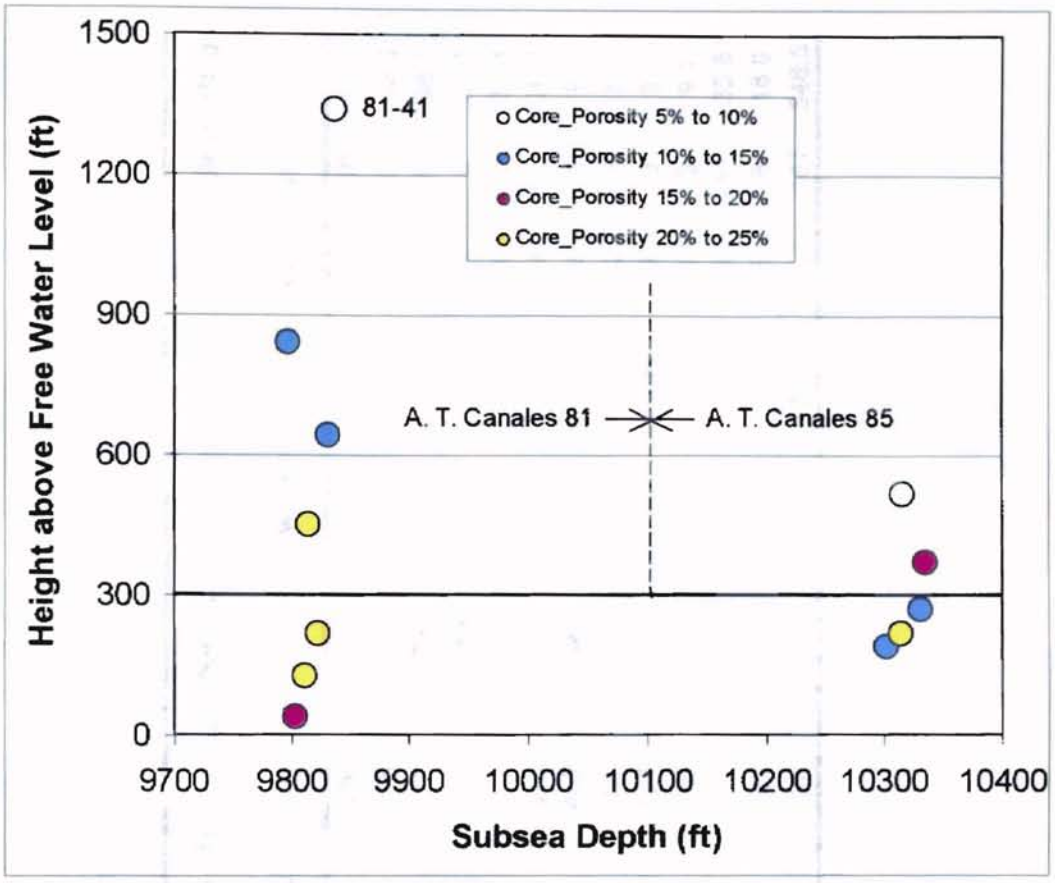

Figure 34. Height of gas column above the free water level. The average height is 300-ft for porous, potential reservoir zones.

determined from the capillary pressure data (Table II). The newly determined water saturation for sample 81-41 is 94.5% while core_Sw is 69.2%.

Figure 35 is the crossplot of permeability v.s. core_Sw and Sw determined from capillary pressure curve at 300 feet gas column. Permeability shows good correlation with Sw from capillary pressure curves. Water saturation values decrease with the increasing permeability. In comparison, core-Sw values are more scattered. The relationship established between permeability and water saturations may be used to derive water saturations if the core_Sw values are not available. Figure 36 shows the crossplot of core porosity v.s. core_Sw and Sw determined from capillary pressure curve

Table II. Petrophysical properties and capillary pressure analysis of samples studied.

Sample #	Color	ϕ	k	Core_Sw	Sorting	rc(micron)		Hg_{core_Sw}	Sw_{300ft}	Hg(ft)		Pdma	Pdwg	Hpd
		%	md	%		median	mode	ft	%	Sw=90%	Sw=50%	psi	psi	ft
85-13	y/w	10.6	0.017	57.1	0.9666	0.23	0.36	190	52	35	350	149	10	33.3
85-25	y/o	21.1	0.117	55	0.6580	0.14	0.43	218	50	43	300	171	12	38.0
85-27	w	9.1	0.003	61.8	0.9787	0.07	0.09	515	72.5	85	1100	440	30	98.0
85-42	y/w	12.1	0.065	47.8	0.9759	0.23	0.31	267	51	31	330	127	9	28.3
85-43	y	16.9	0.216	N/A	0.6986	0.19	0.5		44.5	38	214	156	11	34.8
85-46	y	16.8	0.098	47.6	0.8116	0.19	0.67	370	50.4	30	305	118	8	26.2
81-02	y/w	13.5	0.145	33.7	1.1606	0.96	1.35	842	44.5	2	165	43	3	9.5
81-09	o	17.2	0.005	76.9	1.8112	0.03	0.02	38	70	0	1080	682	46	152.0
81-17	y	23.3	3.27	48	0.9976	0.58	1.99	127	40.6	10	100	39	3	8.8
81-20	y	20.4	1.718	45	1.0386	0.2	1.07	450	50.4	12	314	41	3	9.1
81-28	y	22	0.262	54	0.6299	0.14	0.23	218	47.5	36	267	159	11	35.5
81-36	y/w	11.1	0.015	43.5	1.0167	0.11	0.31	642	54.6	20	407	85	6	18.9
81-41	w	5.9	0.001	69.2	0.6952	0.03	0.01	1340	94.5	580	2950	2454	167	546.5

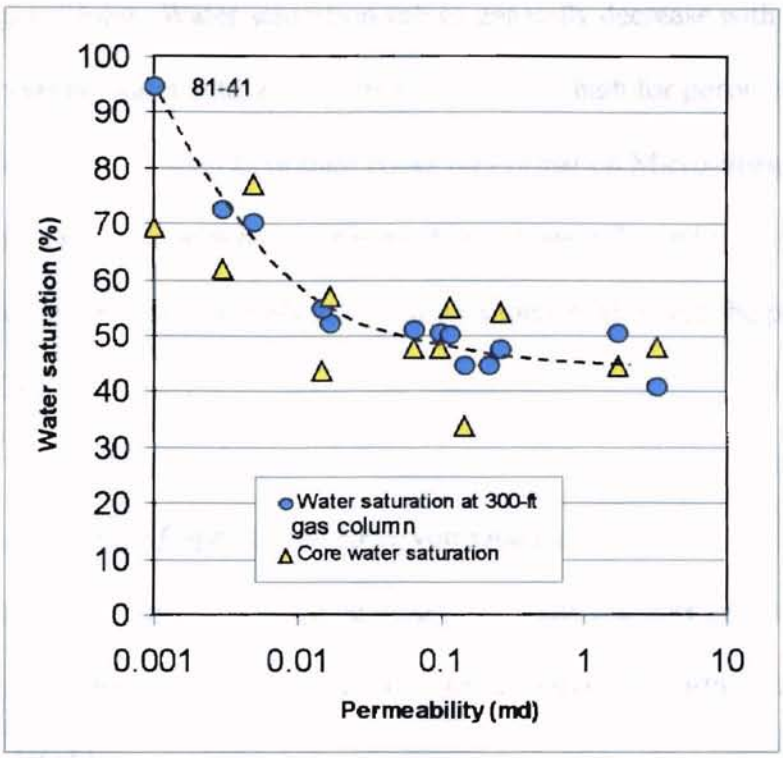

Figure 35. Permeability versus core water saturation and water saturation determined from capillary pressure curves at 300-ft gas column.

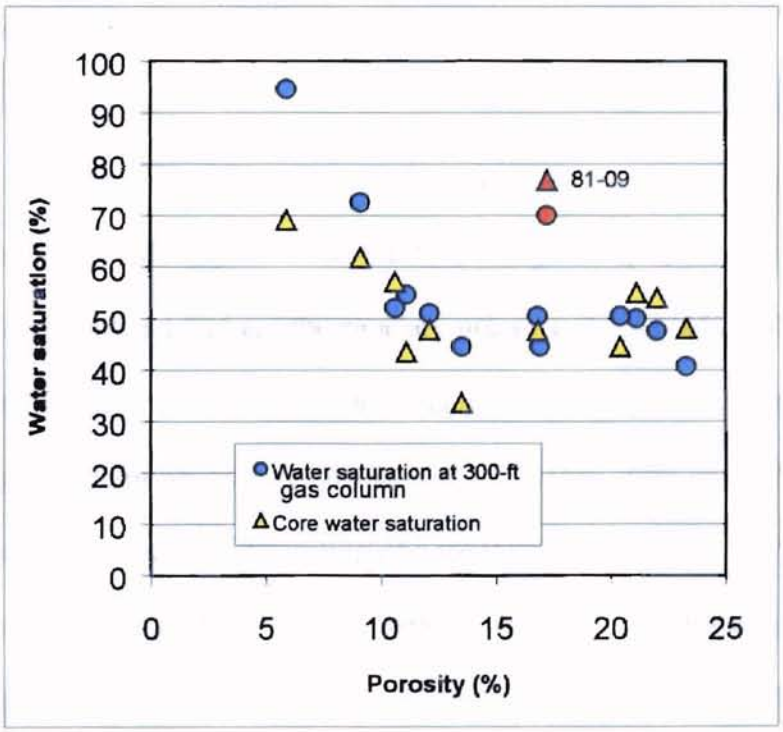

Figure 36. Core plug porosity versus core water saturation and water saturation determined from capillary pressure curves at 300-ft gas column.

at 300 feet gas column. Water saturation values generally decrease with increasing porosity. However, water saturation values can be very high for porous zones with abundant microporosity such as orange zones on Formation Micro-imager logs. Sample 81-09 is a good example which is represented by orange color in Figure 36. Radius of pore throat of this sample is mostly less than 0.08 micron although the porosity is 17.2% (Appendix C).

Pore Structure, Sealing Capacity and Reservoir Quality

Capillary pressure curves can be used to evaluate the pore structure including size, sorting, and distribution of the pore throats. The size and sorting of the pore throat (r_c) are calculated by

$$r_c = 107.6/Pcma \quad (4\text{-}5)$$

$$\text{sorting} = (P84 + P16)/4 + (P95 - P5)/6.6 \quad (4\text{-}6)$$

Where,

r_c Radius of pore throat (micron)

Pcma Capillary pressure in mercury/air system (psi)

P5, P16, P84 and P95 are the capillary pressure at 5%, 16%, 84% and 95% of the maximum mercury injection volume. This equation is similar to that used for sorting analysis of grain size in which grain diameters at 5%, 16%, 84% and 95% of cumulative weight percentage are used. The sorting of pore throat reflects the rock's ability to accept hydrocarbons (Jennings, 1987). In well-sorted rocks, hydrocarbons can rapidly saturate the available pore spaces up to the maximum capacity once a threshold buoyancy pressure is reached. Poorly-sorted rocks require a pressure increase over a much broader range to obtain the same hydrocarbon saturation (Jennings, 1987).

The sorting of pore throat ranges from moderately to poorly sorted and most of the samples are moderately sorted (Table II). The size and distribution of pore throats can be directly reflected from processed capillary pressure curves (Appendix C). Radius of pore throat at median mercury intrusion volume is listed in Table II, which ranges from 0.03 to 0.96 micron. Radius of pore throat at median mercury intrusion volume is less than 0.1 micron for white chromatic zones. The distribution of the pore throat typically shows bimodal distribution. The mode of the relatively larger pore throat contributes to the storage of gas and the mode of micro-pore throat is occupied by water as suggested by the position of the line representing 300-ft height gas column height above free water level (Appendix C).

Seal capacity is the height of hydrocarbon column a seal can hold before it leaks. Displacement pressure is most often used to reflect the seal capacity, which is the pressure required to form a connecting filament of non-wetting fluid through the largest connected pore apertures of the rocks. Schowalter (1979) defined the displacement pressure as the pressure at 10% saturation of non-wetting phase. Jennings (1987) estimated displacement pressure by extending the slope of the plateau to 100% Sw (Figure 33). The average displacement pressure from these two methods is used in this study. Table II lists the displacement pressure, the height of the gas column at 10% and 50% saturation of the non-wetting phase. White zones are characterized by the high displacement pressure (Pcma >400 psi). The gas column at displacement pressure is up to 547 ft. Yellow, yellow/white and yellow/orange mixing zones are characterized by low displacement pressure (Pdma <200 psi). The gas column at displacement pressure is less than 40 ft. Orange zone has medium displacement pressure (Pcma =682 psi) and gas column at displacement pressure is 152 ft. Therefore, white zones can act as potential

seals and yellow/white and yellow/orange mixing zones can act as potential reservoir rock. The reservoir potential of orange zones varies depending on the relative percentage of micropores.

Log Signature of Low-Contrast Zones

The studied 9900-ft sandstones display low resistivity and low contrast log signatures. These signatures for various types of wire-line logs were summarized.

Conventional Logs

Resistivity (Induction Electrical logs)

In general, the total interval is of low resistivity with sporadic sharp peaks that represent thin zones of high resistivity. The resistivity of shale intervals is predominantly between 0.6 and 1 ohm-m. The resistivity of the non-shale zones between sporadic sharp peaks is generally 1.5 to 2.5 times of the shale resistivity.

SP logs

The deviation from the shale base line is commonly less than one chart division for intervals between high resistivity peaks. However, some of the relatively thick (>2 feet) low resistivity sandstone beds have SP deflection of more than one chart division from the shale baseline. The high resistivity peaks generally exhibit depressed SP around one chart division.

Gamma ray logs

Gamma ray logs are more sensitive to variations in lithology and appear "busier" than the SP curve. The deviation from the shale base line is less than 40 API units for intervals between peaks. High resistivity peaks have gamma ray deviation of more than 30 ~ 40 API units.

Neutron and density logs

The clay-rich appearance of the LR-LC zones is also reflected in the combined neutron and density curves. Neutron porosity is generally higher than density porosity. The separation between neutron and density logs is mostly less than 12% for sandy intervals. Occasional crossover of neutron and density porosity curves indicates gas effects. A concurrent decreasing of neutron and density curves can be seen for those high resistivity tight peaks. In shale zones, the separation between neutron and density porosity is higher than 15%.

High-resolution Logs

Array induction logs

Array induction logs provide resistivity measurements for five different investigation depths: 10, 20, 30, 60 and 90 inches. These tools can resolve beds down to 1 foot in thickness (Sneider and Kulha, 1995). Shallow investigation curves (10" and 20") effectively defined boundaries for beds thicker than 1.5 ft, but the thin beds limit the effectiveness of the deeper curves in measuring resistivity in beds less than three feet thick.

High-resolution gamma ray logs

High-resolution gamma ray logs can generally resolve beds thicker than 2-3 ft. (Sneider and Kulha, 1995). In the LR/LC 9900-ft interval, gamma ray responses defined sandstones thicker than three (3) feet and detected thinner shales (approximately 1.5 ft. thick). However, in LR/LC 9900-ft zone, many beds are less than 1 foot thick as evidenced by the cores and FMI logs.

High-resolution neutron and density logs

High-resolution neutron and density logs respond sensitively to changing in rock properties. Density porosity correlates strongly with core-plug porosity measurements for beds thicker than 1 foot. Neutron values are consistently higher than density ones. This is likely a response to OH^- (hydrogen in hydroxyl ion) in clay minerals.

The vertical resolution of these high-resolution wire-line logs varies from 1 to 3 feet. Beds less than 1-ft thick can not be resolved by these logs.

Micro-imager and the Correlation with High-resolution Wire-line Logs

Micro-imaging tools measure the resistivity in the flushed zone and are generally not affected by formation fluids. They are commonly used to reveal structure dips, sedimentary structures, fractures and enhance bed boundaries to half inch. In addition, they may be used to investigate diagenetic and biogenic features. Color changes on the micro-imaging logs, which represent the relative resistivity of beds, have been shown to correspond to specific rock properties in the Vicksburg (Al-Shaieb et al., 2000). Dark gray-brown zones on the static micro-imager view represent silty claystone and shale.

White zones represent highly cemented sandstones with low porosity and permeability. Yellow zones have the highest porosity and permeability and represent the reservoir facies. Orange zones have high porosity, but may have low permeability due to high clay content. Micro-imaging logs are suitable for high-resolution correlation, and are especially useful in identifying reservoirs and seals in LR/LC intervals (Al-Shaieb et al., 2000). Many high resistivity spikes on induction electrical logs and high-resolution logs correspond to white zones. If these zones are thicker than 1.5 ft, they will exhibit low neutron/density porosities (Figure 37 and 38).

Wire-line log signatures of LR/LC intervals were compared with chromatic zones from micro-imaging logs and cores. This analysis established general characteristics of these zones on high-resolution logs. Repetitive patterns were observed and described as follows:

Yellow Zones

1. Apparent separation between shallow and deep resistivity curves (Figure 39). Shallow resistivity readings are mostly higher than medium and deep resistivity ones. Separation is generated by increased resistivity caused by the invasion of fresh water mud filtrate (high resistivity) into the zone. This invasion profile indicates permeability. The reading of deep resistivity is around 1.2 to 2 ohm-m. The ratio of shallow to deep resistivity is higher than 1.2. However, this invasion profile could be obscured by the thin bed effect and gas effect. The reversed invasion profile could be generated as a result of strong gas effect.

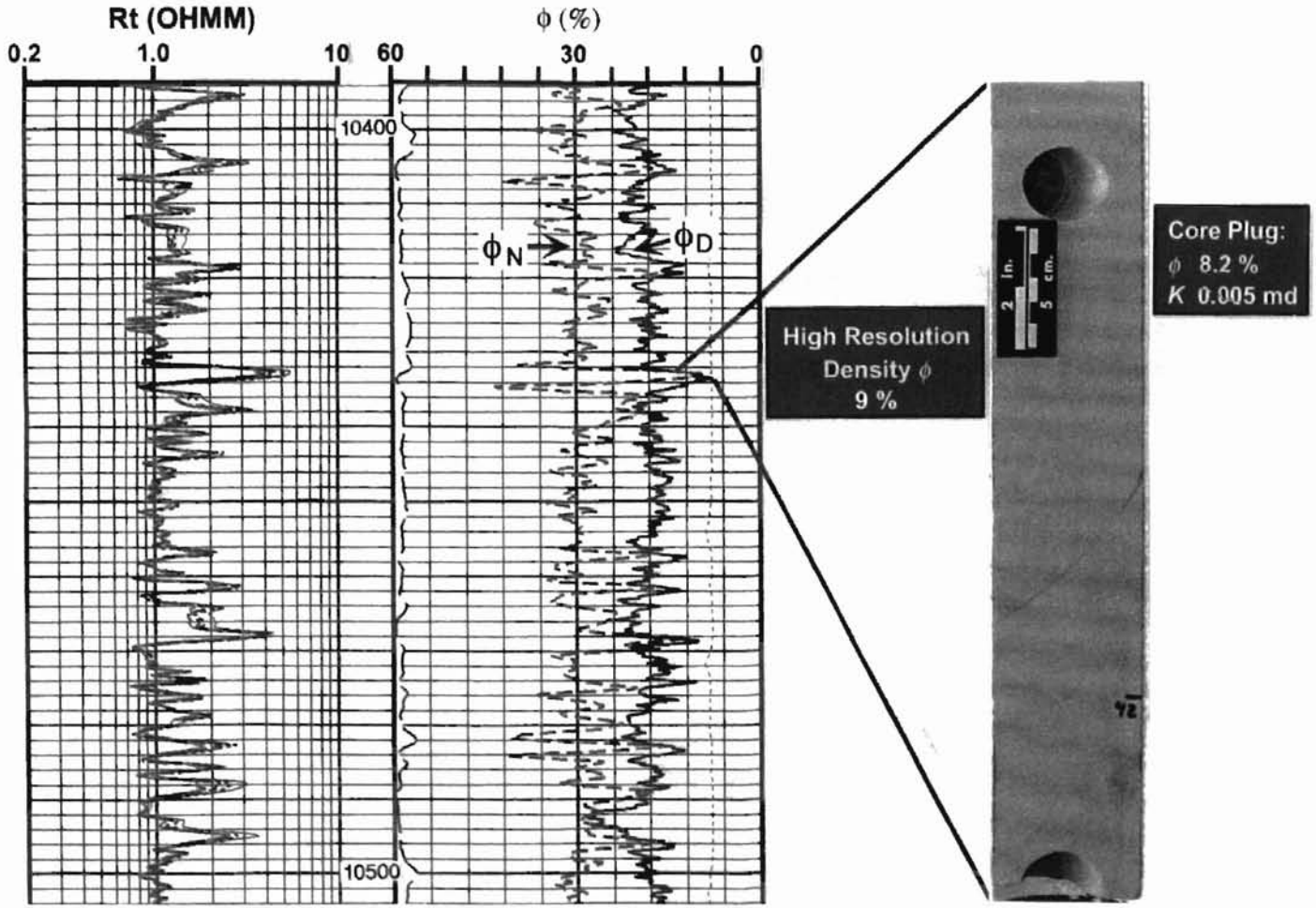

Figure 37. Comparable porosity measurements from neutron-density logs (9%) and core plug analyses (8.2%) indicate high-resolution logs determined rock properties in a 1.5-ft thick zone. High-resistivity measurement across this low-porosity zone confirms the effectiveness of these tools.

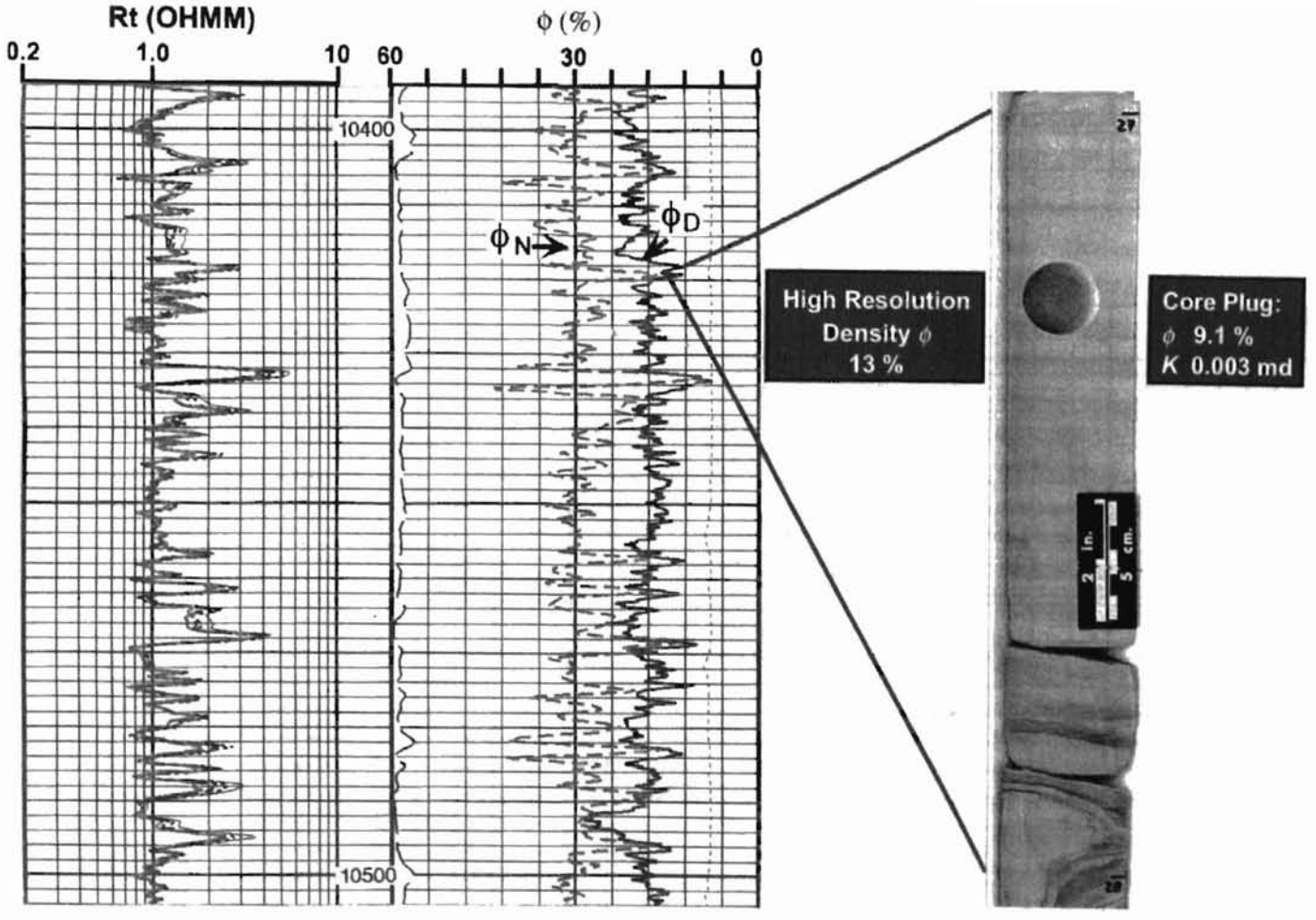

Figure 38. Discrepancy between porosity measurements from high-resolution log and core plug analyses for a thin (<1-ft) bed. These values indicate the low porosity zone in core (9.1%) was not accurately reflected by the log measurement (13%). The higher log value was affected by adjacent high porosity zones. The resistivity value also reflects the influence of adjacent beds.

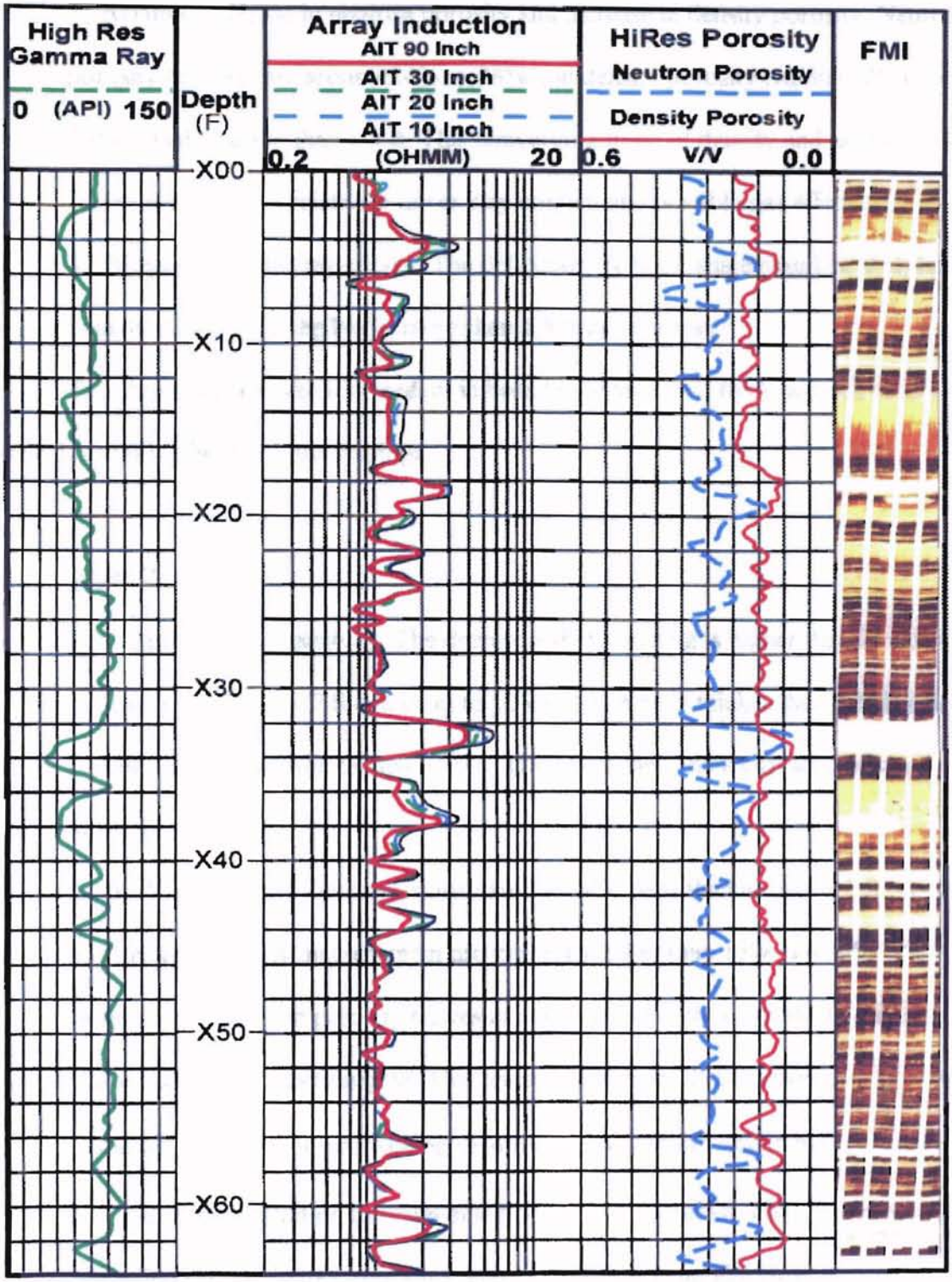

Figure 39. Wire-line log signatures of chromatic zones.

2. Relative decrease in neutron porosity and increase in density porosity. Neutron porosity readings are around 24% to 28% and density porosity readings 20% to 26% in beds thicker than 1.5 ft. This converging trend of density and neutron curves indicates the relatively lower clay content and possible gas effect.

3. "Cleaner" gamma ray curves. The deflection from the shale base line is higher than 40 API units if the bed is more than 1.5 ft in thickness.

The above features are less evident in beds less than 1 foot thick because of the vertical resolution limit of wire-line logs.

White Zones

1. Relatively high resistivity. The deep resistivity reading is higher than 2 ohm-m in beds thicker than 0.7 ft and is up to 10 ohm-m in beds thicker than 1.5 ft. All curves tend to track the shallow curve. This gives the zone a characteristic spike-like appearance.

2. Both neutron and density porosity are low. For beds thicker than 1.5 ft, neutron and density porosity measurement are generally lower than 15% and 10% respectively. Neutron porosity curves are characterized by a significant shift toward the low porosity region. This phenomenon reflects the lower clay content in the white zone. The neutron log records the OH^- (hydrogen in hydroxyl ion) in clay minerals, in addition to water-filled porosity. In contrast, clay content has less effect on density porosity since matrix density is generally close to the density of the clay minerals.

3. "Clean" gamma ray curves. The deflection from the shale base line generally is more than 40 API units for beds thicker than 1.5 ft.

Thin beds will suppress the above features.

Orange Zones

1. Minor separation between shallow and deep resistivity curves due to the lower permeability. The ratio of shallow to deep resistivity is less than 1.2.

2. Merging effect of neutron and density porosity value is less evident.

3. Relatively "dirty" gamma ray curves. Deflection from the shale base line is generally less than 37 API units (two and half chart divisions).

Nuclear Magnetic Resonance Logs

Nuclear magnetic resonance tools can provide lithology independent effective porosity, irreducible water volume and permeability estimates (Coates, et al., 1991; Lomax and Howard, 1994). Two magnetic resonance logs were available in TCB field. They are magnetic Resonance Imaging Logging (MRIL, Numar/Halliburton) and Combinable Magnetic Resonance Imager (CMR, Schlumberger).

CMR porosity is <10% and irreducible water volume is < 7% in white-colored zones thicker than 1 foot. The CMR porosity of the other zones (orange and yellow) is generally higher than 15% and irreducible water volume is 10% to 15%.

The Numar/Halliburton tool gave similar results to the CMR. MRIL porosity (MPHI) is <15% and irreducible water volume is <10% in the white zones. In yellow zones, MPHI porosity readings are relatively high (>16%). For yellow zones thicker than 4 feet, irreducible water volume decreases to less than 9% and the irreducible water

saturation will be around 40% to 60%. The irreducible water saturation generally agrees with the distribution of total water saturation determined from core and capillary pressure analysis in yellow zones which will be discussed later. This may suggest that the total water saturation is at or near the irreducible water saturation. In orange zones, irreducible water readings tend to be higher than those for yellow zones.

The vertical resolution of these tools (CMR and MRIL) limits their application in this LR/LC interval. Newer tools have enhanced vertical resolution and may expand their usage. The fifth generation of CMR tool is capable of 6-in. vertical resolution to identify very thin permeable zones (Schlumberger, 2000).

Log Interpretation of Low-Contrast Zones

Factors Generating LR-LC Reservoirs

Based on the core description and thin-section analysis, the low resistivity and shale-like appearance are generated by several factors. These are the amount, type and distribution of clay minerals, thin-bed effect, and grain size.

Three clay distribution patterns are evident in the 9900-ft zone: dispersed clays, laminated clays/shales, and structural clays (Figure 40). Dispersed clays are found between grains. They fill pore space, coat or line pores. Most of the clay minerals, especially 2:1 type, develop negative charge on their lattice. This is mainly due to the isomorphous substitution of Al^{3+} for Si^{4+} in tetrahedral sheet or Mg^{++} or Fe^{2+} for Al^{3+} in octahedral sheet (Grim, 1968). The overall balance of their (-) charge is balanced by the presence of positive ions absorbed on the surface of layers or at the edges. When placed in water, interlayer cations in clays will exchange with other cations in solution. The

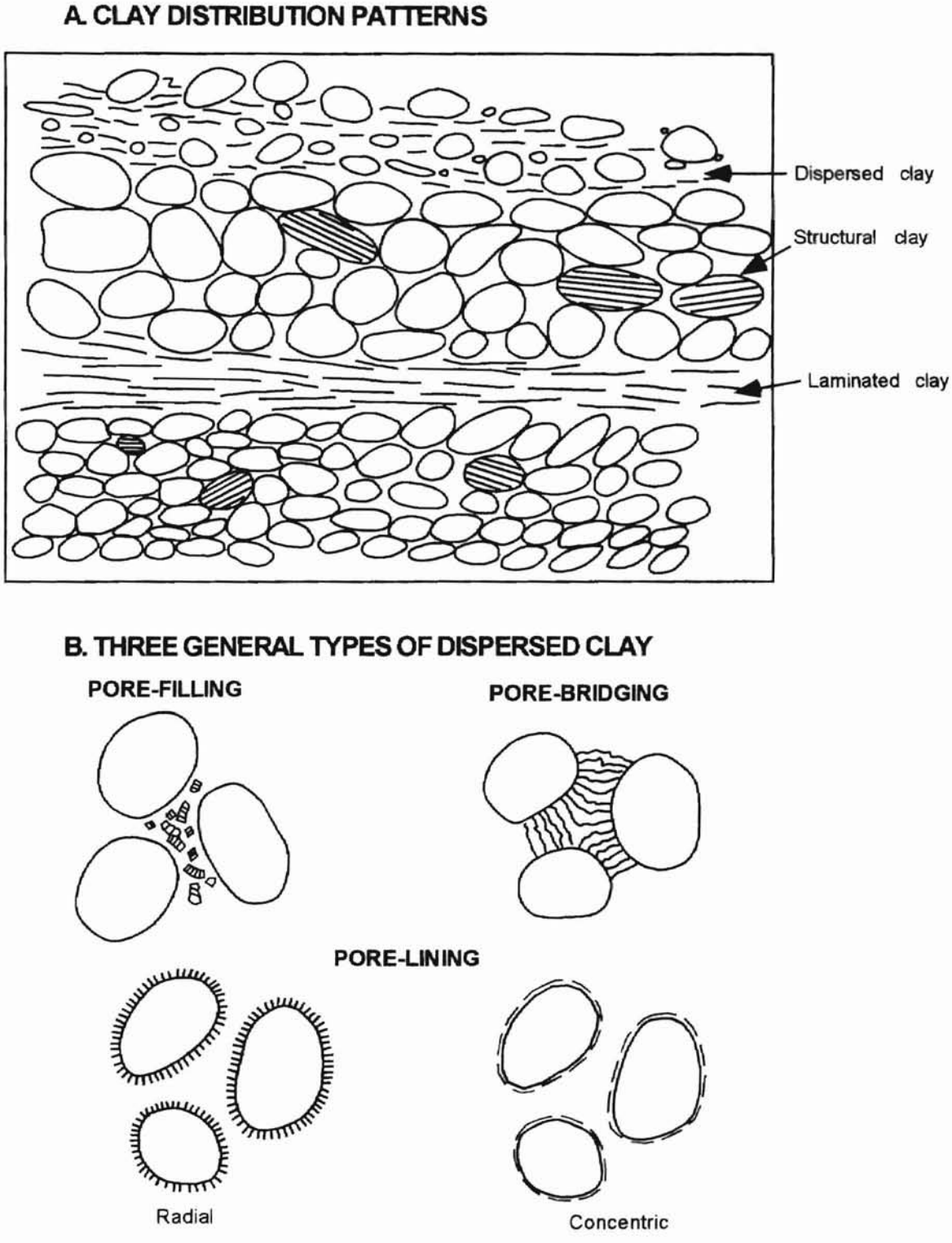

Figure 40. Clay distribution patterns (after Wilson and Pittman, 1977) and types of dispersed clay in a sandstone reservoir.

ability for clay minerals to exchange ions is quantified as cation exchange capacity (CEC). The higher the CEC, the more the clay will contribute to the conductivity. CEC values vary for different types of clay. Mixed-layered clay and smectite have relatively high CEC and significantly increase the formation conductivity. Illite has moderate CEC value while kaolinite and chlorite have even lower cation exchange capacity (Grim, 1968).

Thinly bedded and laminated clays/shales are present throughout the cored intervals. They make up 12% to 54% and average 32% of the LR/LC intervals. A laminated method for shaly sand interpretation, such as Thomas-Stieber (1975) model, is not considered to apply to less than 1-ft zones due to the irregularity of the sand streaks. Mixed-layered clay (smectite and illite) is a major constituent in shale/claystone laminae which typically have resistivity reading around 0.8 ohm-m. The vertical resolution of the deep induction log is too large to resolve the thinly bedded and laminated sandstone, siltstone and shale sequence. The resistivity values recorded in thin sandstone layers are decreased by the surrounding conductive shales. The more resistive the beds, the greater the thin bed effects will be.

Structural clays are quite common in the 9900-ft zone. They include grains, such as altered volcanic rock fragments, argillaceous rock fragments and glauconite. Vicksburg sandstones typically contain approximately 5% to 10% of structural clays that contributes to their high conductivity.

Grain size is another important factor influencing formation conductivity. The very fine- and silt-size grains of the 9900-ft zone have high surface area and contribute to the high capillary bound water content in the sandstones. Microporosity is another factor that increases surface area and bound water content.

Clay Volume Determination

Clay volume is an essential parameter in calculating effective porosity and water saturation. High-resolution gamma ray logs were used to determine the volume of clay in the LR/LC interval. Clay volume was estimated using the following formula (Dresser Atlas, 1979).

$$Vcl = 0.33\ [2^{(2 \times IR)} - 1.0] \quad \text{(Consolidated rocks)} \tag{4-7}$$

$$IR = (GR_{log} - GR_{min})/(GR_{max} - GR_{min}) \tag{4-8}$$

$$GRn = IR\ 5\ 100 \tag{4-9}$$

Where:

Vcl	Volume of clay
IR	Gamma ray index
GRlog	Gamma ray reading from formation
GRmax	Gamma ray reading from shale
GRmin	Gamma ray reading from clean sand
GRn	Normalized gamma ray readings

For sandstones in Vicksburg Formation, GRmin is commonly chosen to be 30 API. GRmax is determined here from histogram of gamma ray readings (Figure 41). GRmax is chosen where frequency in the clay-rich part decreases dramatically. Bimodal distribution is exhibited in gamma ray histogram. The mode with lower gamma ray readings (45 to 64 API) represents sand-rich intervals and high gamma ray reading mode (>64 API) represents clay-rich interval. The frequency of the gamma ray reading decreases around 90 API which is chosen to be GRmax for A. T. Canales 85. The gamma ray histogram of A. T. Canales 81 shows one major clay-rich hump and a very vague

sand-rich hump. Frequency has an apparent decrease around 110 API which is chosen to be GRmax. The very vague sand-rich hump is related to the thin bed effect and lower resolution gamma ray curve in A. T. Canales 81. Sand-rich beds shown as yellow and white color in Formation Micro-imager logs are around 30% in both wells. This illustrates the advantage of high-resolution processing.

Histograms of normalized gamma ray readings are shown in Figure 42. The studied two wells show good resemblance, especially in clay-rich part. Therefore, the selection of GRmin and GRmax is reasonable.

The calculated clay volume values were compared to petrographic data obtained from x-ray diffraction and modal thin section analysis (Table III). Calculated clay contents generally match those from x-ray diffraction and modal thin section analysis for A. T. Canales 85. The calculated value is much higher than measured value in A. T. Canales 81 due to the thin bed effect on the conventional gamma ray curve. However, even high resolution gamma ray logs have considerable limitation in determining the clay volume in 9900-ft zone. As mentioned above, sandstone beds thicker than two (2) to three (3) feet can be effectively detected by high resolution gamma ray logs while bed thickness in 9900-ft zone is typically less than two feet.

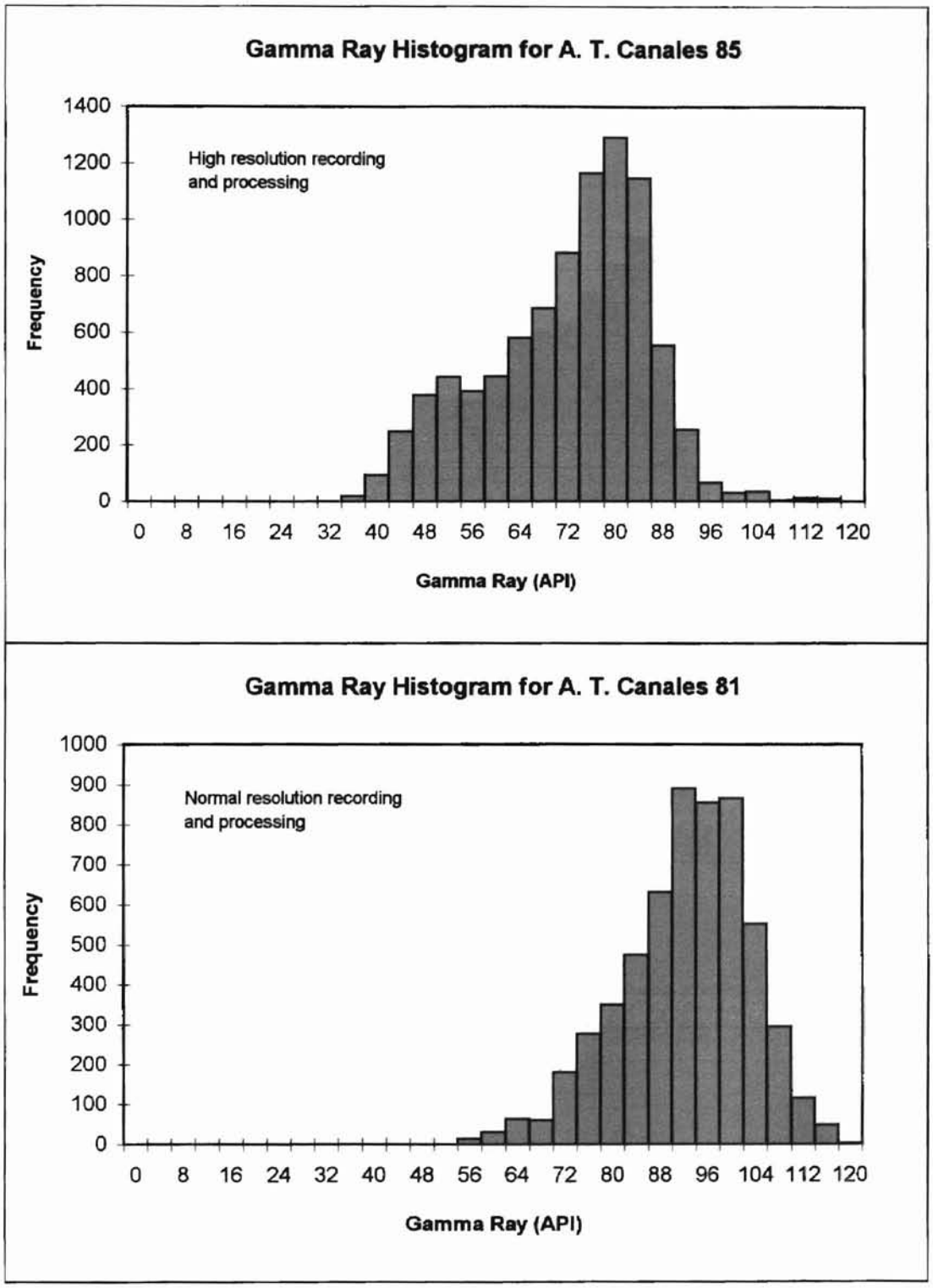

Figure 41. Gamma ray histograms for A. T. Canales 85 and A. T. Canales 81.

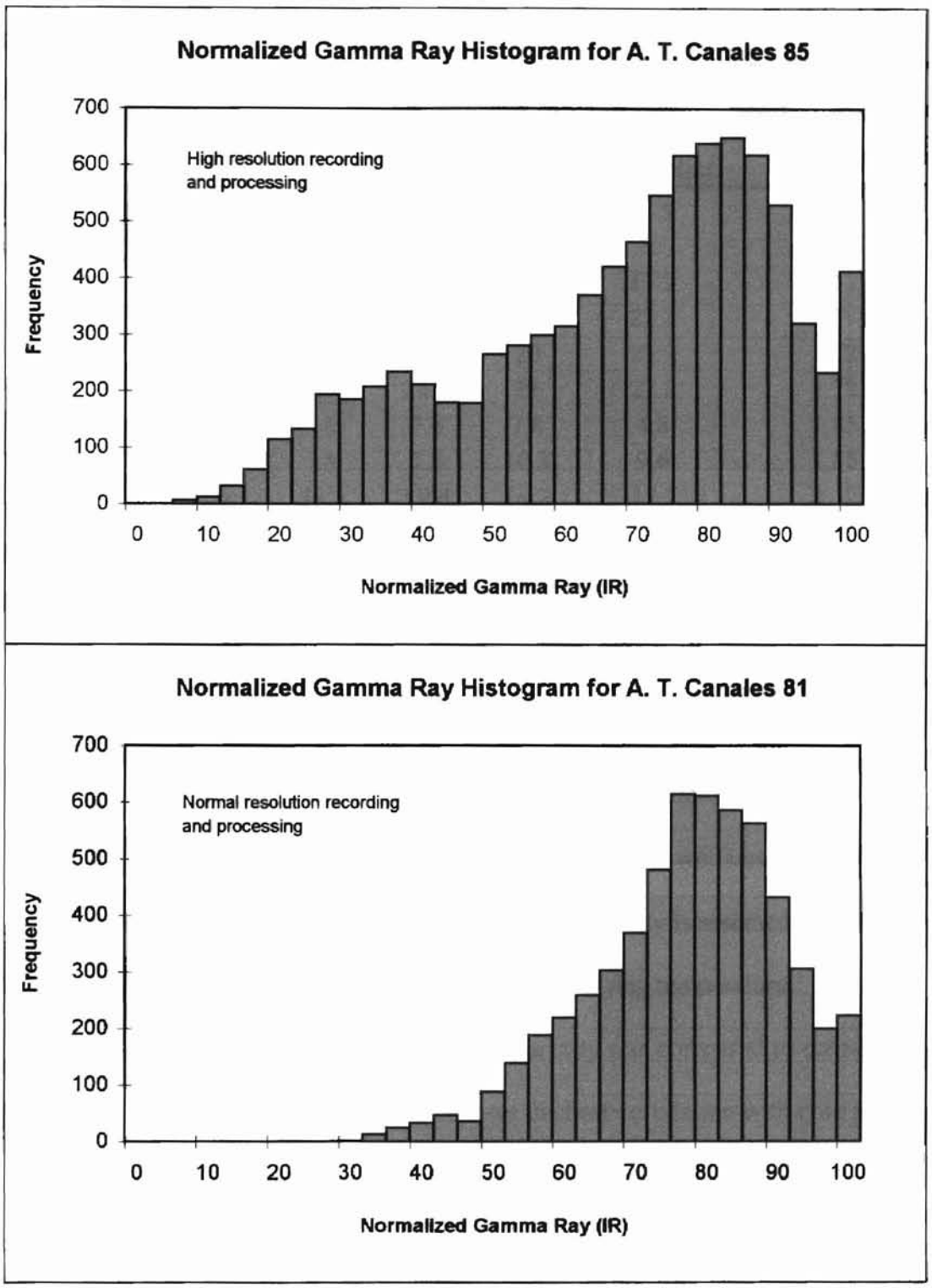

Figure 42. Normalized gamma ray histograms for A. T. Canales 85 and A. T. Canales 81. Note the very vague sand-rich hump is concluded due to the lack of high resolution recording and processing.

Table III. Comparison of clay volumes determined from gamma ray, x-ray, and thin section analysis.

Depth _Core	GR	GRn	Volume of Clay (%)			Bed Thickness
F	API		GR	x-ray	thin section	F
10412.3	60	48.4	31.5	26.3	31.9	1.32
10421.5	52	36.7	21.9	18		2
10422.4	52	36.7	21.9	17	17.7	2
10423.3	52	36.7	21.9	18.2	22.3	2
10424.3	54	40	24.5	20	23.2	1.72
10425.5	54	40	24.5	23	22.2	1.72
10441	39	15	7.6	7.8	4.8	1.85
10442	39	15	7.6	10.3	9.6	1.85
10445.3	50	33.3	19.4	16.2	17.1	2.12
10446.3	50	33.3	19.4	21.2	15.4	2.12
9927.8	90	75	60.3	30.4	29.7	1.2

Total Porosity and Effective Porosity Determination

Total porosity (ϕt) and effective porosity (ϕe) are two important parameters in interpretation of shaly sandstones. The difference between the two is mainly the space occupied by clay bound water. The conventional core porosity is assumed to represent the total porosity, although total porosity is dependent on drying temperature.

High-resolution neutron and density log porosity was compared to core-plug porosity (Figure 43, 44). Density porosity shows the best correlation with core porosity with R^2=0.6618. The square of correlation coefficient is only 0.0981 for the correlation between core porosity and neutron porosity. Point scattering in Figure 43 is primarily generated from the thin-bed effect. In Figure 44, only beds thicker than 1 ft are plotted and the square of correlation coefficient is increased to 0.9149 for density porosity. If density porosity is used to represent core porosity for all bed thickness, the standard error

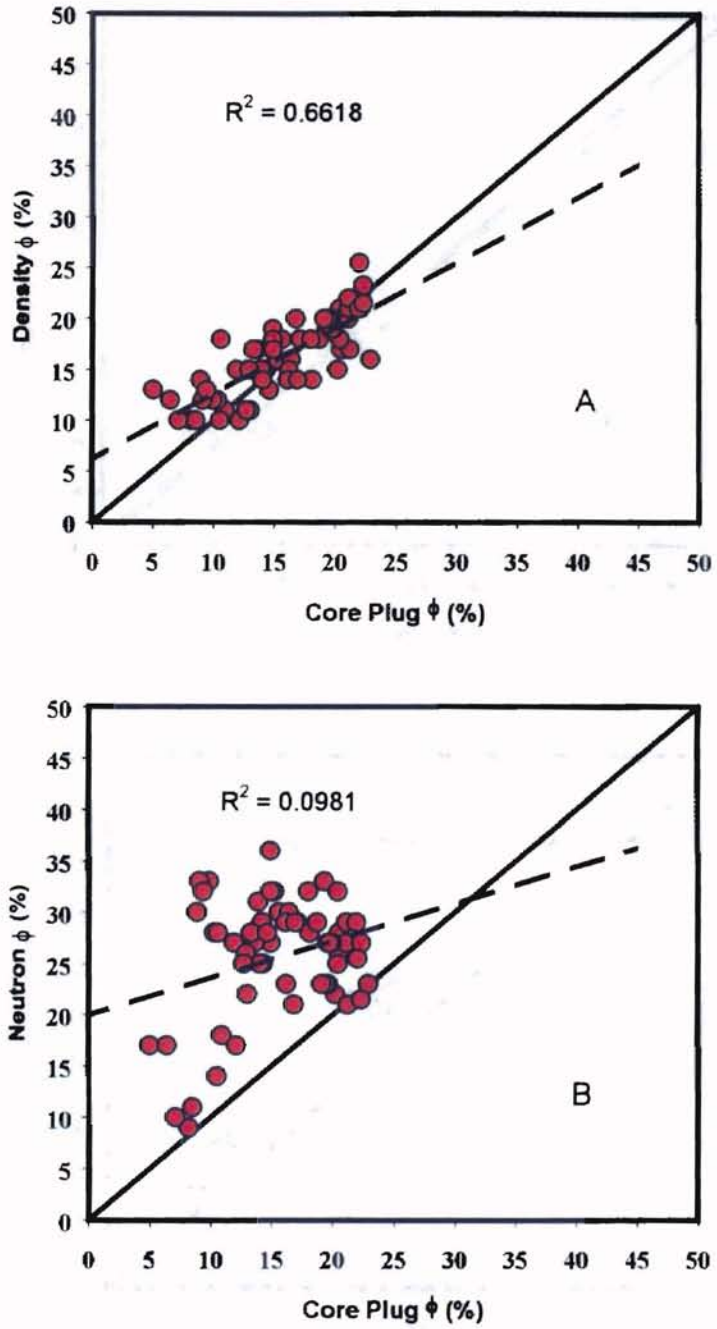

Figure 43. Correlation of E-log porosity and core porosity for all bed thickness. Solid line (45° line) represents ideal prediction and dashed line is regression line. A. Core porosity v.s. Density porosity. B. Core porosity v.s. Neutron porosity.

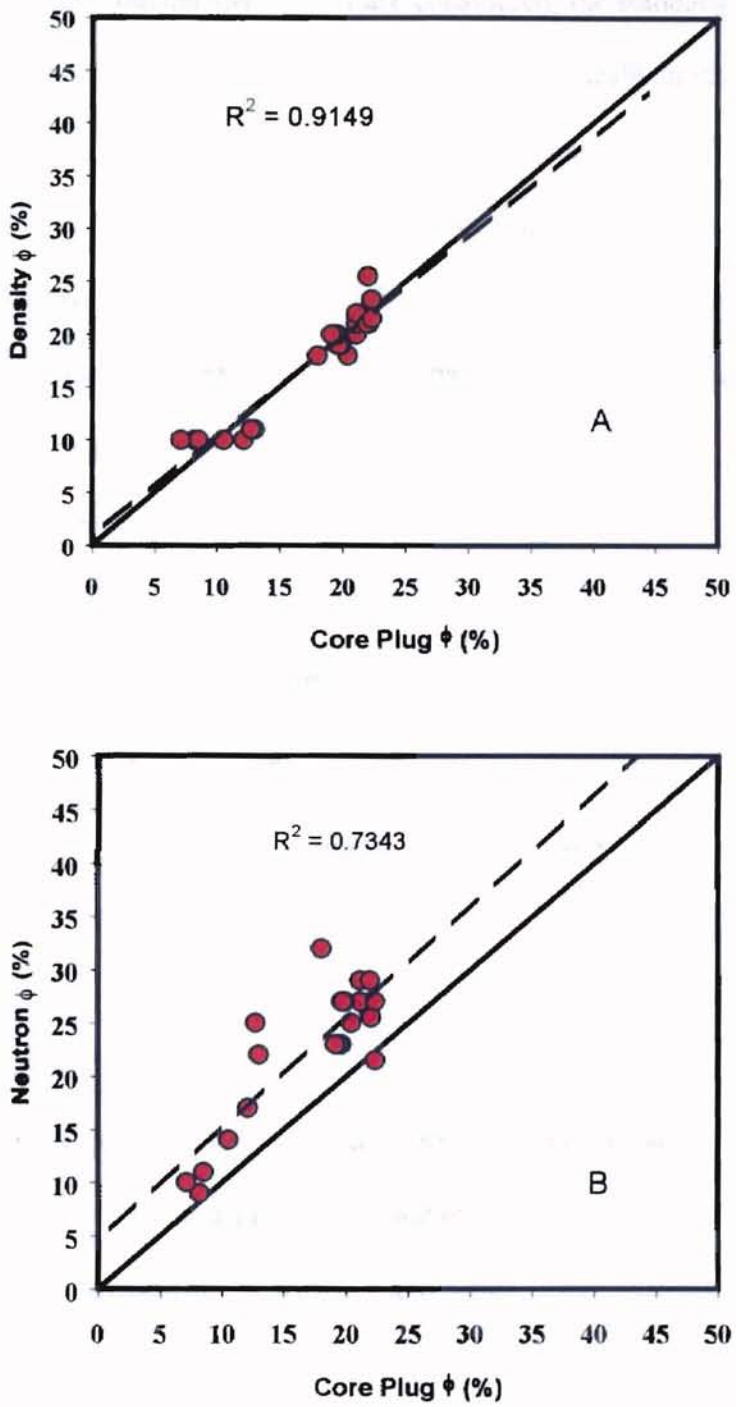

Figure 44. Correlation of E-log porosity and core porosity in beds thicker than 1 ft. Solid line (45° line) represents ideal prediction and dashed line is regression line. A. Core porosity v.s. Density porosity. B. Core porosity v.s. Neutron porosity.

is 2.8%. By comparison, the standard error is 11.5% between neutron porosity and core porosity. If only beds thicker than 1 foot are considered, the standard error between density porosity and core porosity decreases to 1.5%. Typically, a standard error of 2% indicates good results (Personal Communication, Jay Patchett, 2000). Since core porosity was considered the more accurate measurement of total porosity, density porosity was used to represent total porosity in this study.

Effective porosity used in Modified Simandoux and Indonesia equations was calculated as follows:

$$\phi e = \phi t - Vcl \times \phi sh \qquad (4\text{-}10)$$

Where,

ϕe Effective porosity

ϕt Total porosity

ϕsh is the porosity of nearby shale read on the density log. A value of 0.17 is used in this study.

Water Saturation Calculations

A variety of methods were used to estimate water saturation. They include Archie (Archie, 1941), Modified Simandoux (Schlumberger, 1972), Indonesia (Poupon and Leveaux, 1971), Waxman-Smits (Waxman and Smits, 1968; Waxman and Thomas, 1974), Dual-Water (Clavier, et al., 1977, 1984) and Modified Dual-Water models. The effectiveness of the various water saturation calculation methods were tested by comparing calculated water saturations with those from routine core analysis that were assumed to represent true total water saturations. The effective water saturations

calculated from Modified Simandoux and Indonesia models were converted into total water saturations (Sw_T) to ensure a consistent comparison of all models. High-resolution array induction logs (AIT), and neutron/density logs were used for log calculations. Sw measurements from core were conducted by Core Laboratories, Inc., Houston, Texas. It was assumed that, in this gas prone area, only gas was expelled from the core as it was brought to the surface, leaving the largely irreducible water. Using the core-calibrated FMI log, it was possible to accurately correlate core sample locations to the high-resolution logs and ensure that measurement locations were the same.

Formation temperature in this study was determined from the bottom hole temperature data in the study area (Figure 45). As shown in this figure, temperature increases apparently around 8500 ft, forming a plateau. This plateau may correspond to the top of the overpressure zone. From Figure 45, the formation temperature (Tf) below 8500 ft can be calculated using the following formula.

$$Tf = (Depth + 5800)/61.458 \quad (4\text{-}11)$$

Calculated formation temperature is around 255°F to 270°F in 9900-ft zone of the studied wells.

Archie equation

$$Sw_T^n = F \times Rw/Rt \quad (4\text{-}12)$$

$$F = a/\phi t^m \quad (4\text{-}13)$$

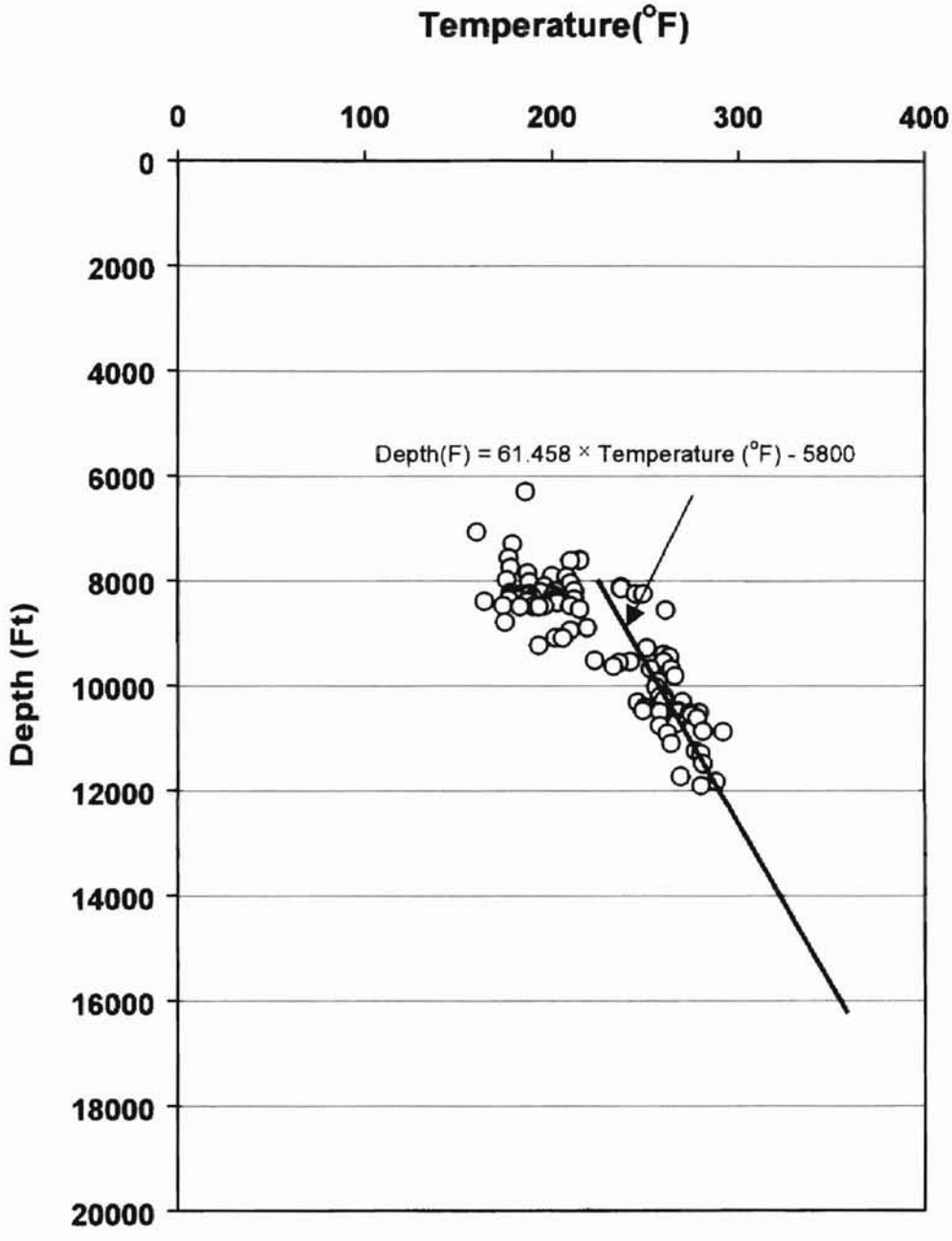

Figure 45. Depth and temperature profile in TCB field.

Where,

F	Formation factor
Rw	Formation water resistivity
Rt	True formation resistivity
a	Tortuosity factor
m	Cementation exponent
n	Saturation exponent

Commonly for sandstones, a is 0.81and m=n=2, i.e. $Sw_T^2=0.81*Rw/(\phi t^m*Rt)$ (Asquith, 1982). The reported formation water salinity is 32747 ppm in 9900-ft zone (ORYX, 1993) and the corresponding Rw at formation temperature is around 0.057 ohm-m. This yielded calculated Sw results mostly higher than 70% for this LR/LC reservoir, suggesting that this interval is non-economic (Figure 46). However, 83% of water saturation values from core measurements are lower than 70%. Most of them are around 50~60% (Figure 47). The calculated high water saturation can be generated by high Rw and/or m and n values.

In this study, Pickette crossplot of density porosity and deep resistivity was established to obtain the Rw and m values (Figure 48). To minimize the thin bed effect, only thicker beds (>1 ft) were used. The left most line is the 100% water saturation line. The slope of this line is m value, which is around 1.68. One thick continuous sandstone bed from 10487-10496 ft was found to have big variation in density porosity and resisvitity, which was plotted as yellow dots. The distribution of these yellow dots is basically parallel to 100% water saturation line. This suggests that the water saturation of this zone is relatively constant. Therefore, it may be feasible to get constant water

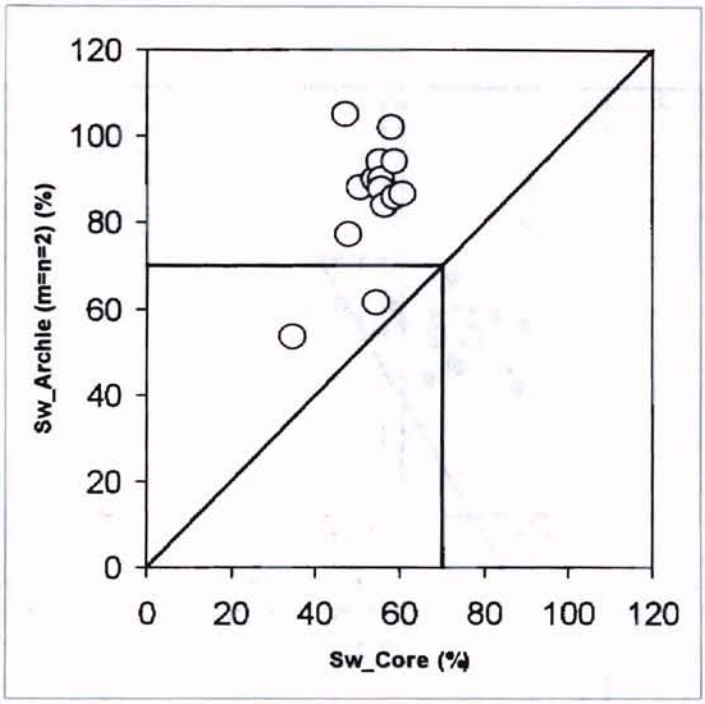

Figure 46. Calculated water saturation values from Archie equation versus those from core measurements. Solid line (45° line) represents ideal prediction.

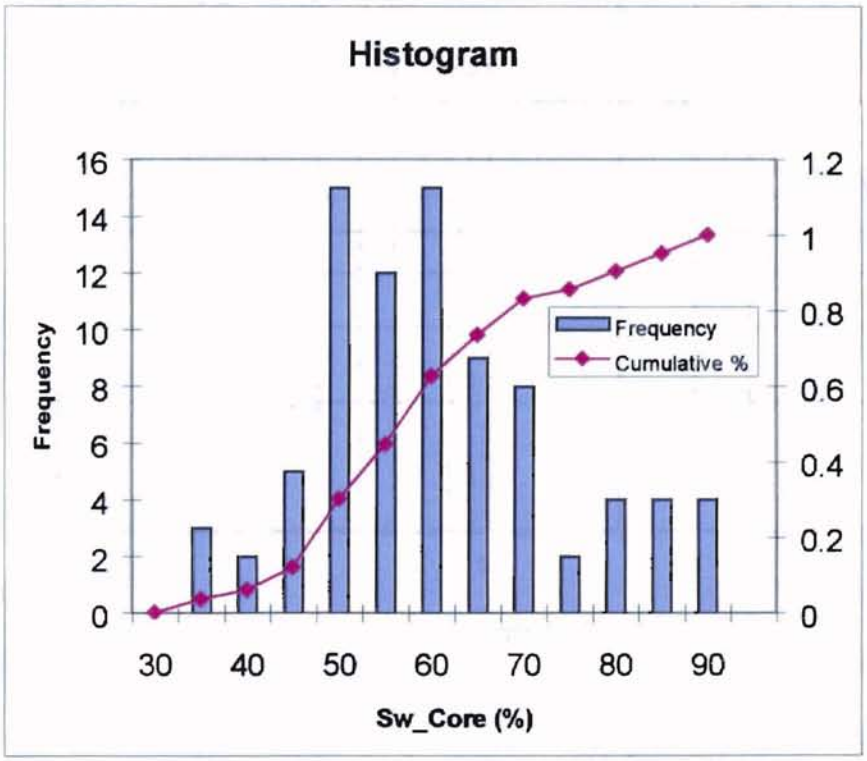

Figure 47. Distribution of water saturation from core measurement. 83% of water saturation values are lower than 70%. Most of them are around 50 to 60%.

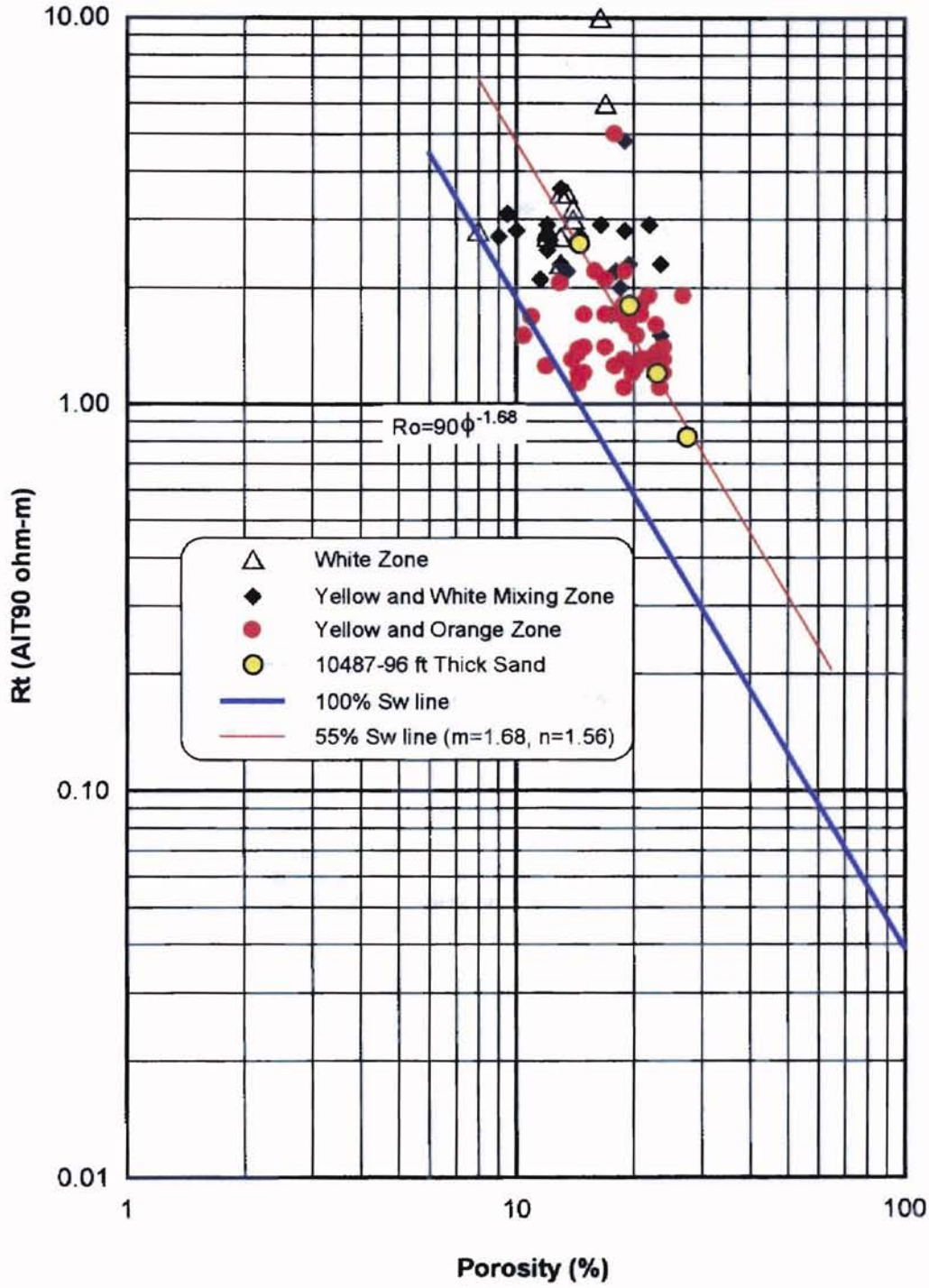

Figure 48. Pickette crossplot of resistivity versus density porosity for all thick sandstone beds (>1ft) in 9900-ft zone. m and Rw can be determined from Ro line, which are 1.68 and 0.039 ohm-m, respectively.

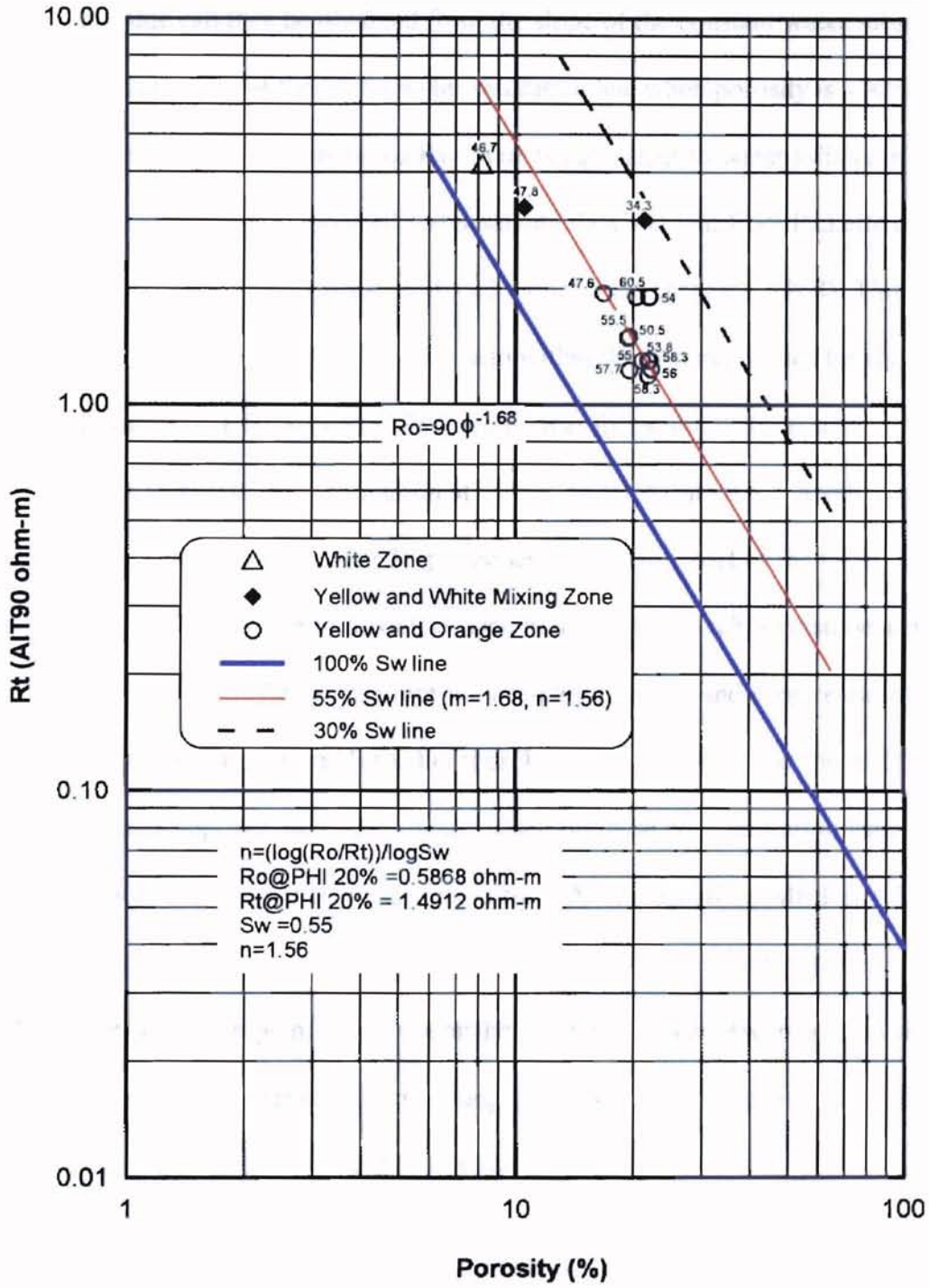

Figure 49. Pickette crossplot of resistivity versus core porosity for all thick sandstone beds (>1ft) in cored interval of 9900-ft zone. 55% Sw line is drawn based on the distribution of core water saturation values. n can be calculated from 100% and 55% Sw lines.

saturation line from single thick porous sandstone bed with great variation in porosity and resistivity. m value can then be obtained from the slope of the constant water saturation line. Rw is the resistivity of the 100% water saturation line when porosity is 100%, which is 0.039 ohm-m. The newly determined Rw value is equivalent to water salinity of 50,000 ppm. The difference between reported water salinity data and that from Pickette crossplot may be caused by the water distillate produced with the gas (Magara, 1968). This Rw value determined from Pickette crossplot is also within the regional values for the Vicksburg Formation in Texas. Fett (1980) stated that formation water resistivity normally ranges from 0.03 to 0.12 ohm-m at formation temperature and a value as low as 0.035 ohm-m is used to interpret the deeper zones in the south part of the trend. Tortuosity factor (a) is chosen to be one as used in most of the shaly sandstone analysis.

Figure 49 is the Pickette crossplot of core-plug porosity and deep resistivity in the cored interval. Only sandstone beds thicker than 1 ft are used here. The line of 55% water saturation is approximately determined based on these core saturation values. Saturation exponent (n) can then be calculated from Archie equation, which is 1.56. Line of 30% water saturation is drawn using the new m and n values, which matches well with the 34% water saturation point from core analysis. The improved Rw, m and n values can be further demonstrated by resistivity modeling using Waxman-Smits, and Modified Dual-Water methods, which will be discussed later.

Archie equation for common sandstones was then modified using these newly estimated m, n, and Rw values. The calculated water saturation values from Modified Archie equation have a good match with core measurements (Figure 50 and 51). Therefore, these m, n and Rw values can yield reasonable Sw values with the simple Archie equation, i.e. Modified Archie equation.

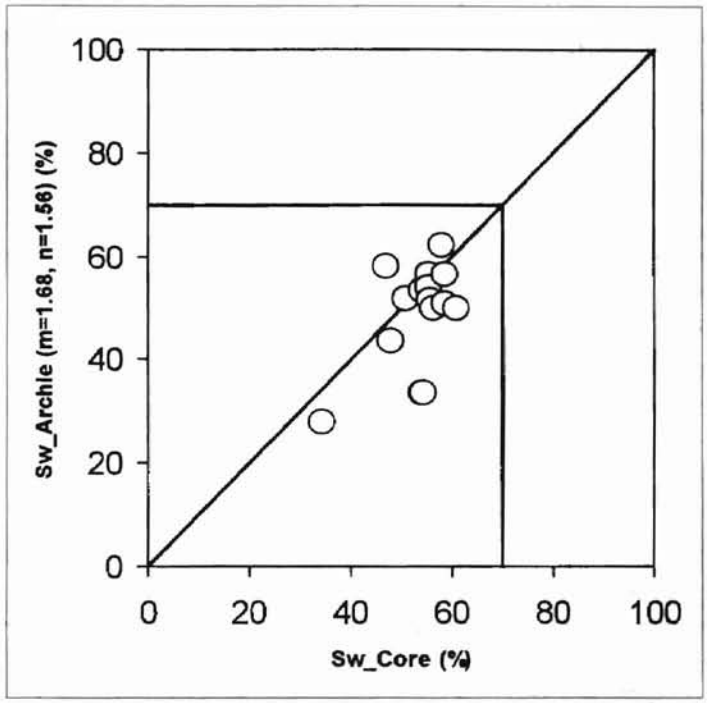

Figure 50. Calculated water saturation values from Modified Archie equation versus those from core measurements. Solid line (45° line) represents ideal prediction.

The Modified Archie equation not only gives good results, but also needs fewer parameters from wire-line logs. High resolution resistivity and porosity are the only parameters required from the wire-line logs. Gamma ray and SP logs are not needed to estimate clay volume in Modified Archie equation. Therefore, the calculated water saturations from Modified Archie equation will not be affected by the poor vertical resolution problem of gamma ray and SP logs.

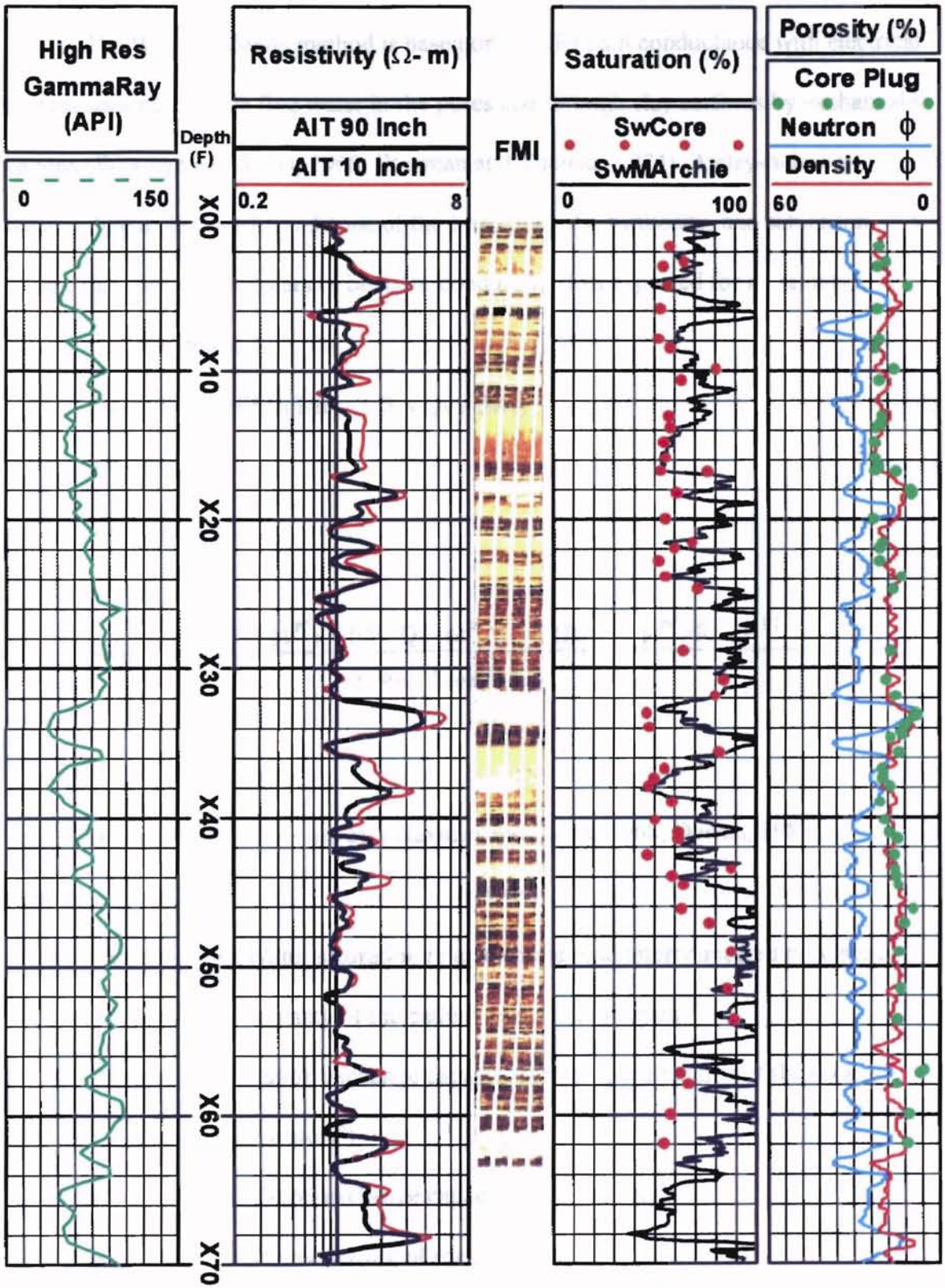

Figure 51. Water saturation (Sw) curve derived from Modified Archie equation. Solid dots in Sw track are the measured core water saturation values. Calculated Sw curve has a good match with those from core measurements.

Waxman-Smits method

The Waxman-Smits method is based on parallel path conductance with electrical current passing through free water in the pores and through clay surfaces by exchangable cations (Waxman and Smits, 1968; Waxman and Thomas, 1974). A clay-rich rock behaves like a clean rock/sandstone of the same porosity, turtuosity, and saturation, except that the water appears to be more conductive than expected for its salinity. Equations are as follows:

$$1/Rt = Sw_T^{n^*}/F^* \times(1/Rw + B \times Qv / Sw_T) \quad (4\text{-}14)$$

$$F^* = 1/\phi t^{m^*} \quad (4\text{-}15)$$

for $n^* = 2$,

$$Sw_T = \frac{-(B\times Qv\times\phi t^{m^*}) + ((B\times Qv\times\phi t^{m^*})^2 + 4\,(Rw^{-1}\times\phi t^{m^*}\times Rt^{-1}))^{1/2}}{2\times Rw^{-1}\times\phi t^{m^*}} \quad (4\text{-}16)$$

$$Qv = CEC\times\rho_{ma}\times(1-\phi t)/\phi t \quad \text{(Waxman and Smith, 1968; Dewan, 1983)} \quad (4\text{-}17)$$

Where,

Sw_T	Water saturation related to the total interconnected pore space
B	Mobility of the cations ($ohm^{-1}.m^{-1}.ml.meq^{-1}$)
Qv	Cation exchange capacity per unit pore volume of the rock (meq/cm^3)
CEC	Cation exchange capacity (meq/g rock)
ρ_{ma}	Matrix density of rock (gm/cc)
ϕt	Total interconnected porosity

m* Apparent cementation factor

n* Apparent saturation exponent

Two (2) is used for m* and n* in this study. B is a function of temperature and water resistivity. B was estimated from Figure 16 in Waxman and Smits (1974). Based on estimated Rw and formation temperature, B will be around 20.

CEC measurement was conducted by Plant and Soil Science Department at Oklahoma State University. The results are shown in Table IV. In order to obtain CEC in other intervals without core measurements, various kinds of crossplots were established (Figure 52). To minimize the thin bed effects, only data from beds thicker than 1-ft are plotted in Figure 52 A, B, D. Gamma ray and (ϕ_N- ϕ_D) show poor correlation with CEC as a result of thin bed effects. The square of correlation coefficients are 0.2684 and 0.1504 respectively for gamma ray and (ϕ_N- ϕ_D). Core porosity and density porosity have better correlation with CEC values with the square of correlation coefficients being 0.5935 and 0.532 respectively. The regression equation between density porosity and CEC values is then adopted to calculate CEC values in the following water saturation calculation. One important prerequisite for this equation is the small gas effect as suggested by the close match of density porosity with core porosity in Figure 43 and 44.

$$CEC\ (meq/g) = 0.1802 \times \phi_D + 0.052728 \qquad (4\text{-}18)$$

Water saturations were calculated for beds thicker than 1-ft in the cored intervals. The majority of calculated water saturation values from Waxman-Smits equation match well with core water saturations (Figure 53, 54).

Table IV. Cation exchange capacity analysis and corresponding petrophysical properties of the analyzed interval. Note that $\Delta(\phi_N-\phi_D)$ value of sample 85-51.2 is 12% which is much higher than the other samples although this sample still has moderate porosity and permeability values. This high $\Delta(\phi_N-\phi_D)$value is erroneous, generated by thin bed effect.

Sample #	GR	GRn	k	ϕ_core	Rt	Sw_core	ϕ_D	ϕ_N	$\Delta(\phi_N-\phi_D)$	CEC	Thickness	FMI Color
	API		md	%	Ω-m	%	%	%	%	meq/100g	F	
81-10.8	81	64	0.023	20.3	1.70	69.1	24.0	26.5	2.5	10.0	0.90	y
81-17.5	81	64	3.270	23.3	1.90	47.9	24.0	28.0	4.0	9.5	0.80	y
81-27.8	90	75	0.132	22.0	2.00	54.0	25.5	25.5	0.0	9.1	1.20	y
85-15.7	55	42	0.066	20.5	1.50	52.9	20.0	26.0	6.0	9.7	0.83	y
85-22.4	52	37	0.156	21.9	1.23	58.3	21.0	29.0	8.0	9.3	2.00	y
85-23.3	52	37	0.126	22.3	1.23	55.3	21.5	27.0	5.5	10.7	2.00	y
85-24.8	54	40	0.094	21.1	1.40	54.0	21.0	28.0	7.0	8.5	1.72	o
85-27.3	51	35	0.003	9.1	2.80	61.8	12.0	16.0	4.0	7.8	0.90	w
85-30.3	68	63	0.218	20.4	1.90	60.5	18.0	25.0	7.0	8.4	1.00	y
85-41.4	39	15	0.005	8.2	4.20	46.7	10.0	10.0	0.0	6.9	1.85	w
85-44.5	50	33	0.301	19.6	1.33	55.5	20.0	23.0	3.0	9.3	2.12	y
85-46.3	50	33	0.098	16.8	1.94	47.6	20.0	21.0	1.0	8.4	2.12	ly
85-51.2	75	75	0.033	15.6	1.60	47.2	18.0	30.0	12.0	9.2	0.13	ly

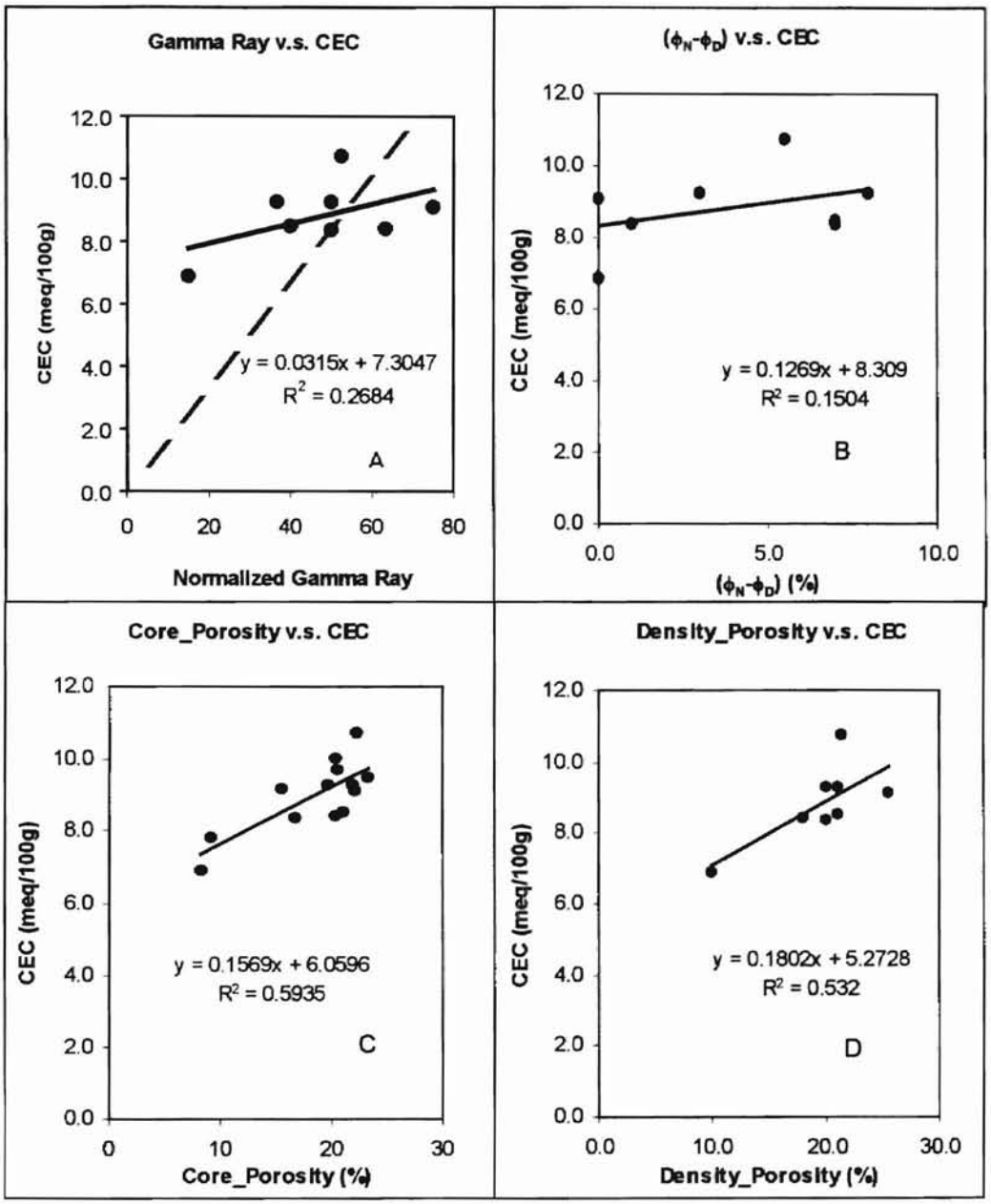

Figure 52. Correlation of measured CEC values with various petrophysical properties. A. Gamma Ray v.s. CEC. B. ($\phi_N - \phi_D$) v.s. CEC. C. Core_Porosity v.s. CEC. D. Density_Porosity v.s. CEC.

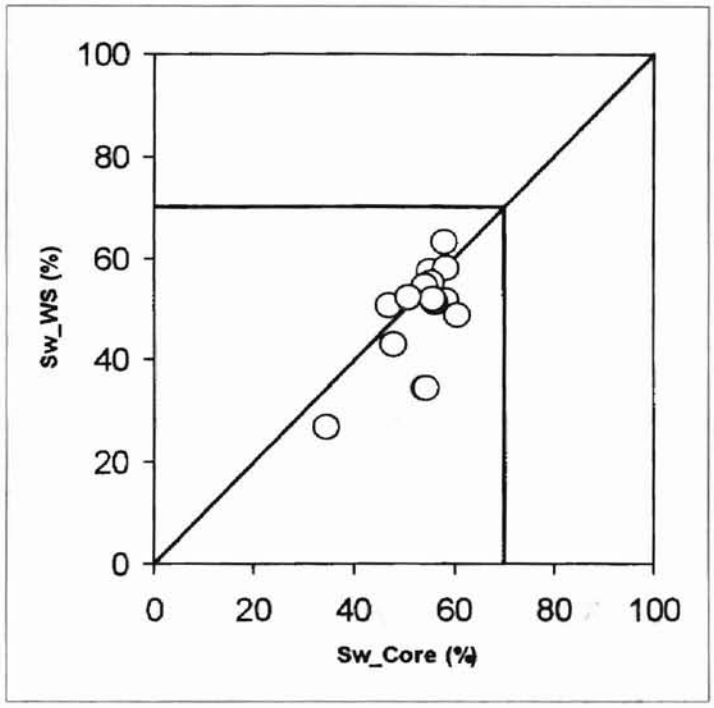

Figure 53. Calculated water saturation values from Waxman-Smits equation versus those from core measurements. Solid line (45° line) represents ideal prediction.

Dual-Water and Modified Dual-Water method

In Dual-Water model, water in the pore space is partitioned into two types: bound water surrounding clay minerals and free or far water at a distance from the surface of the clay minerals (Clavier, et al., 1977, 1984). The conductance of these two kinds of water is different. Bound water resistivity (Rwb) is taken as a universal parameter that only depends on temperature. Rwb was calculated using the following formula by Clavier, et al. (1984).

$$1/Rwb = 7.10^{(-4)} \times (T°C + 8.5) \times (T°C + 298) \quad (4\text{-}19)$$

Far water resistivity is equal to formation water resistivity, i.e. 0.039ohm-m. Water saturations are calculated using the following equations:

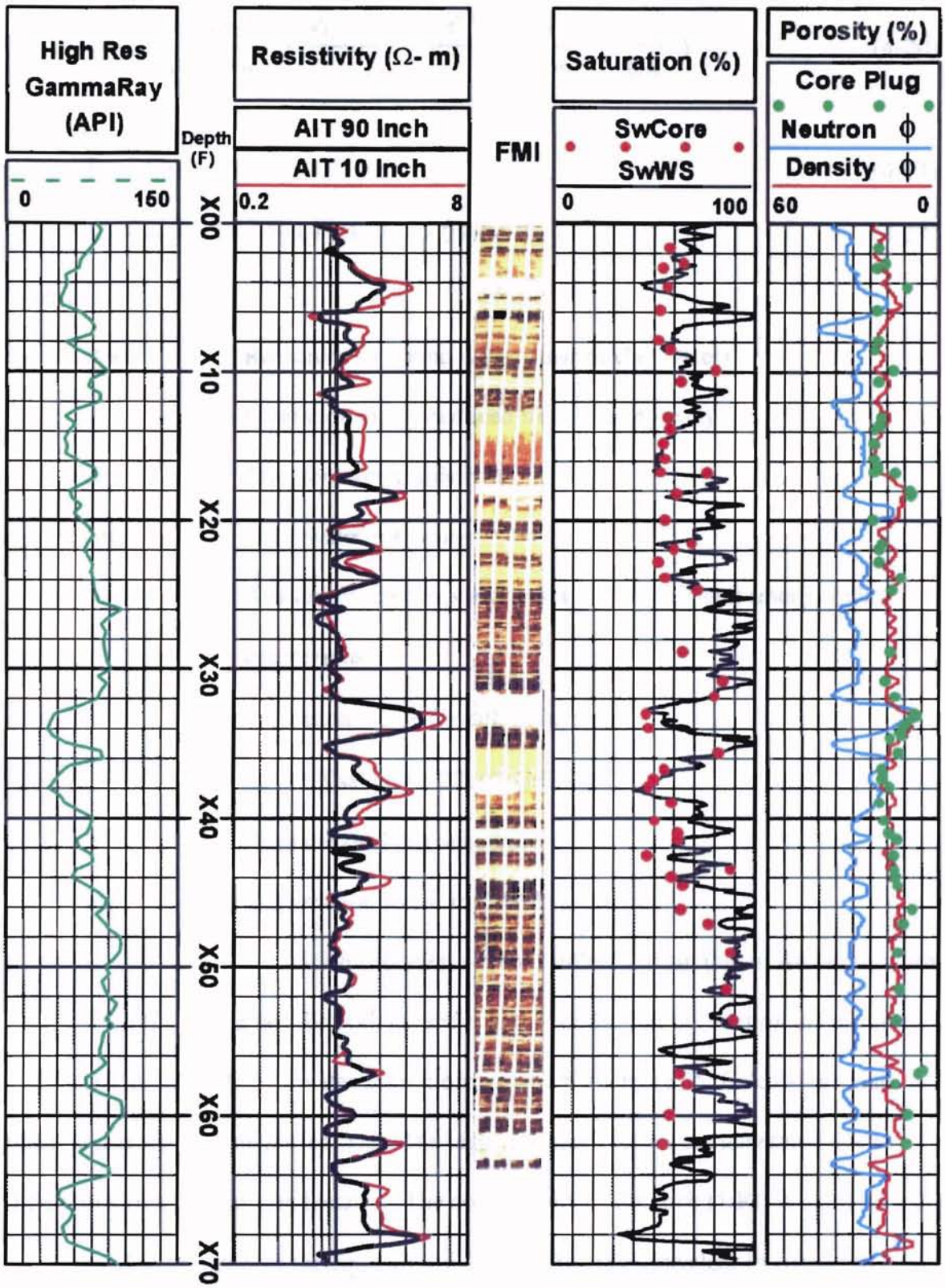

Figure 54. Water saturation (Sw) curve derived from Waxman-Smits equation. Solid dots in Sw track are the measured core water saturation values. Calculated Sw curve has a good match with those from core measurements.

$$\frac{1}{Rt} = \frac{Sw_T{}^n}{Fo \times Rw} + \frac{V_Q \times Qv \times Swt^{n-1}}{Fo}\left(\frac{1}{Rwb} - \frac{1}{Rw}\right) \quad (4\text{-}20)$$

$$Fo = 1/\phi t^{mo} \quad (4\text{-}21)$$

$$V_Q = \alpha \times 0.3 \times (295 + 25)/(Tk + 25) \quad (4\text{-}22)$$

Where,

Rwb	Resistivity of bound water (near or clay water)
Fo	Formation factor deduced from total porosity
Rt	True formation resistivity
Sw_T	Total water saturation
V_Q	Amount of the clay water associated with 1 unit (meq) of clay counterions
α	Expansion factor for diffuse layer (α = 1 if salinity > 22107ppm NaCl)
Tk	Absolute (Kelvin) temperature
m_o	Cementation factor in Dual-Water model
n	Saturation exponent which is different from that in Archie equation

Two (2) is assumed for both m_o and n in this study. The correlation of calculated water saturations with core water saturations is shown in Figure 55. Calculated values are much higher than the measured ones. The high calculated values are generated due to little correction for clay conductance. The conductivity of the rock (1/Rt) is composed of two parts. The first part of the equation ($Sw^n/(Fo \times Rw)$) is equivalent to Archie equation, which is called Archie term below. The latter part of the equation accounts for the

additional conductance from clays. If Rwb is equal to Rw, the latter part of the equation is equal to zero. There will be no correction for clay conductance. Only when clay bound water is much more conductive than free water (1/Rwb > 1/Rw) can the correction be evident. Calculated Rwb at formation temperature is around 0.042 to 0.05ohm-m in 9900-ft zone while Rw is 0.039ohm-m. Therefore, Dual-Water model is not applicable to the studied LR/LC sandstones. This model should perform better in shaly sandstone with very fresh formation water, i.e. Rw >> Rb.

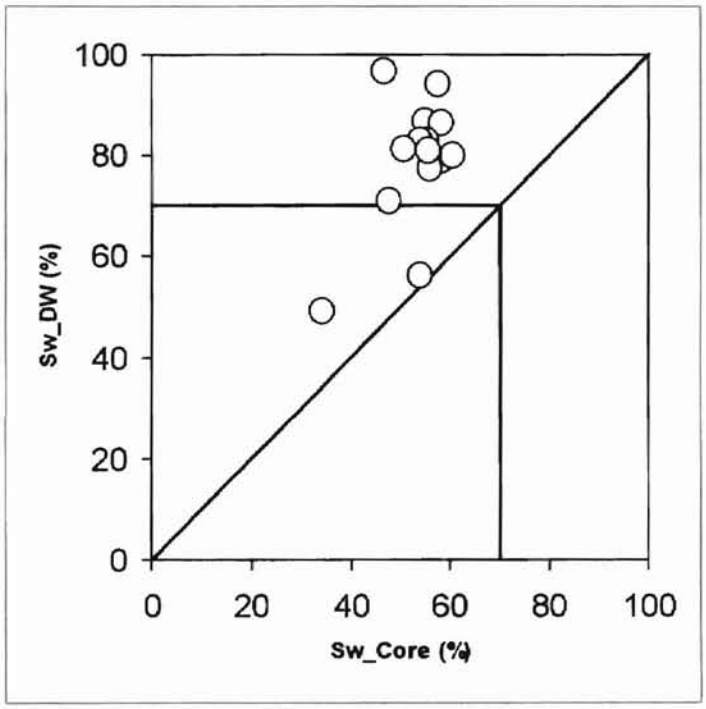

Figure 55. Calculated water saturation from Dual-Water equation versus those from core measurements. Solid line (45° line) represents ideal prediction.

To adopt the concept of the Dual-Water model and overcome the problem discussed above, Jay Patchett (Personal Communication, 2000) modified the Dual-Water model as follows.

$$1/Rt = Sw_T^{\,2}/Fo \times ((1-Swb)/Rw + B \times Qv / Sw_T) \quad (4\text{-}23)$$

$$Swb = 0.25 \times Qv \quad (4\text{-}24)$$

Where:

Swb Bound water saturation

This model uses $B \times Qv/Sw_T$ to correct the additional conductance from clays which is the same as Waxman-Smits model. However, the Archie term is corrected by the fraction of pore space that is not occupied by bound water, i.e. (1-Swb). The constant 0.25 in the equation is equivalent to the V_Q in the Dual-Water model. It assumes that the volume of clay bound water associated with 1 unit of clay counterions is $0.25cm^3$. Qv is the cation exchange capacity per unit pore volume of the rock. Therefore, Swb represents the volume of clay bound water per unit pore volume.

The calculated water saturation generally shows a close match to core water saturations (Figure 56, 57).

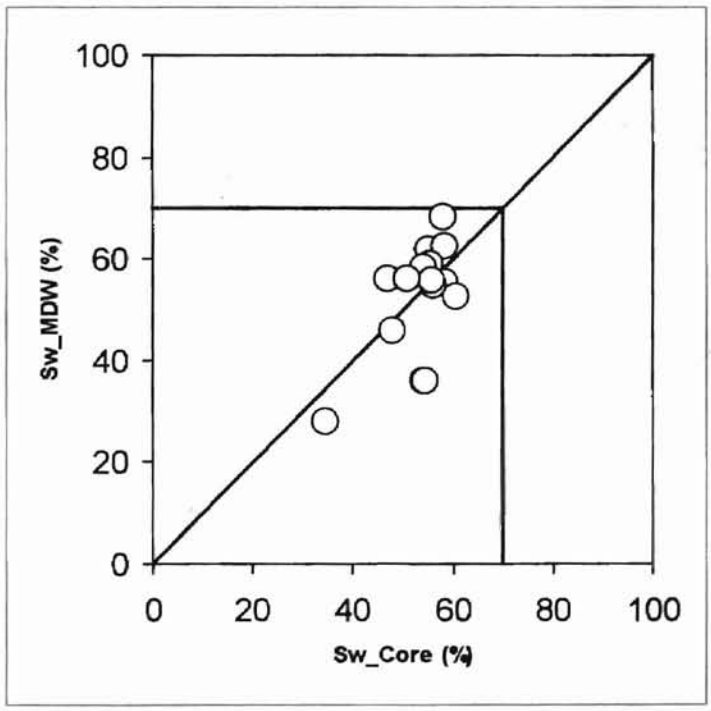

Figure 56. Calculated water saturation from Modified Dual-Water equation versus those from core measurements. Solid line (45° line) represents ideal prediction.

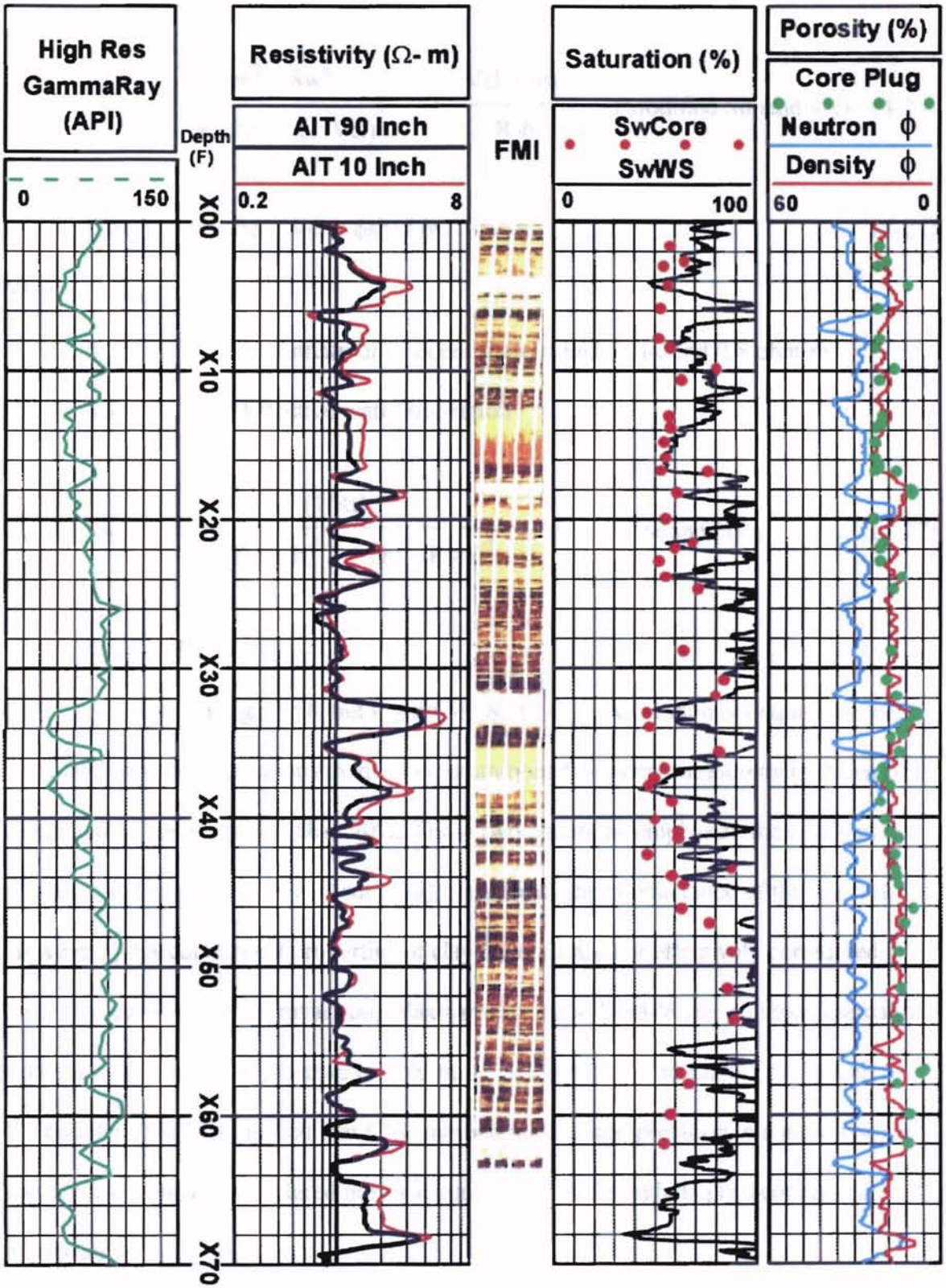

Figure 57. Water saturation (Sw) curve derived from Modified Dual-Water equation. Solid dots in Sw track are the measured core water saturation values. Calculated Sw curve has a good match with those from core measurements.

Modified Simandoux and Indonesia equations

$$\frac{1}{Rt} = \frac{\phi e^2 \times Sw^n}{a \times Rw \times (1\text{-}Vcl)} + \frac{Vcl \times Sw}{Rsh} \quad \text{(Modified Simandoux)} \quad (4\text{-}25)$$

$$Sw_T = (Sw \times \phi e + Vcl \times \phi sh) / \phi t \quad (4\text{-}26)$$

Where,

Rsh Resistivity of adjacent shale, which is around 0.8 ohm-m.

Sw Effective water saturation

$$Sw = \frac{(1/Rt)^{1/2}}{(Vcl)^d/(Rsh)^{1/2} + (\phi e^2 /Rw)^{1/2}} \quad \text{(Indonesia)} \quad (4\text{-}27)$$

Where,

$d = 1\text{-}Vcl/2$

As shown in Figure 58 and Figure 59, Simandoux and Indonesia equations yield much higher water saturations than water saturations from core measurement. Most of the calculated values are higher than 70%. These two equations emphasize the conductance of clay. The higher the clay content (Vcl), the greater the conductance of the interval. However, physicochemical properties of clay minerals are not effectively considered in these two equations. In comparison, Waxman-Smits and Dual-Water methods use cation exchange capacity (CEC) instead of volume of clay. Johnson and Linke (1977) and Desbrandes (1985) suggested that CEC method tackles interpretation in a more correct way since clay is not considered not by its quantity, but through its physicochemical properties.

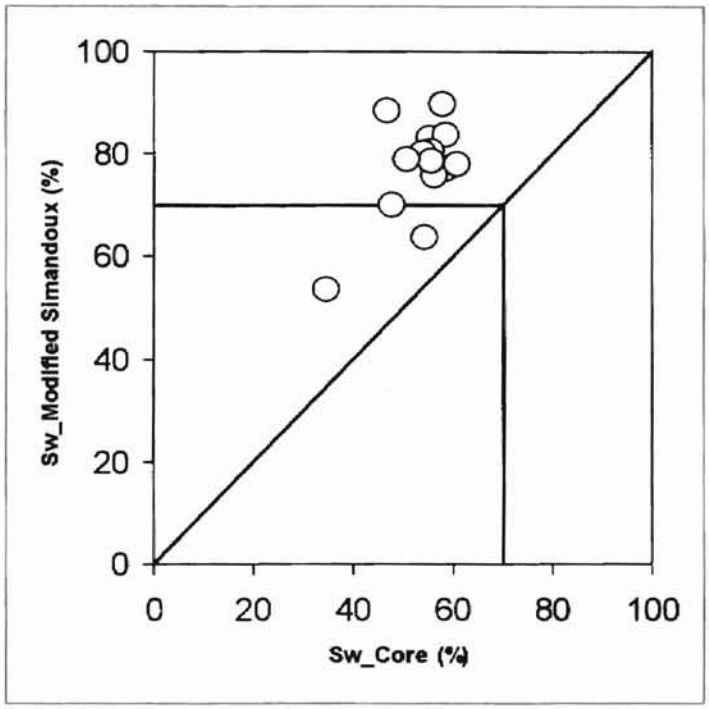

Figure 58. Calculated water saturation values from Modified Simandoux equation versus those from core measurements. Solid line (45° line) represents ideal prediction.

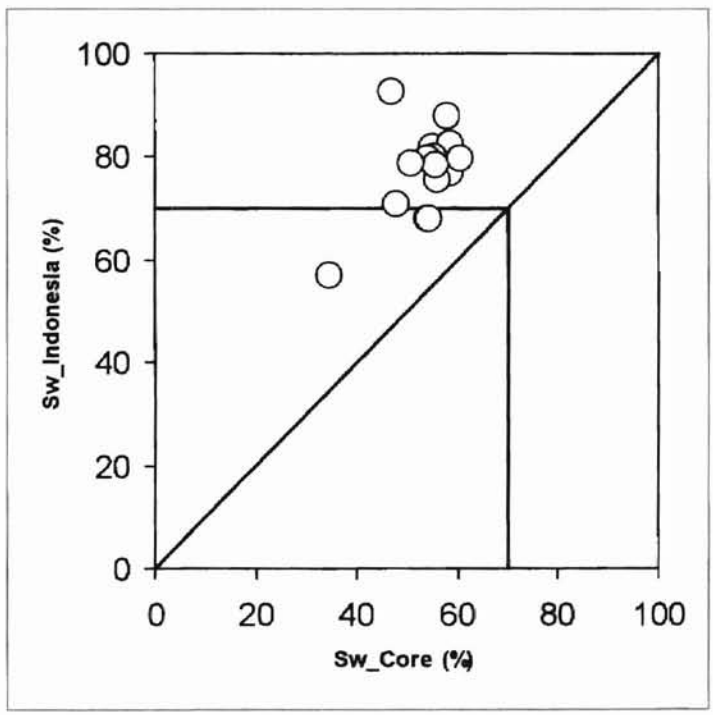

Figure 59. Calculated water saturation values from Indonesia equation versus those from core measurements. Solid line (45° line) represents ideal prediction.

To summarize, the models examined show high variability in predicting Sw. Archie, Dual-Water, Modified Simandoux and Indonesia equations all yield much higher water saturations (i.e. large systematic error) than those from core measurement. Modified Archie equation, Waxman-Smits and Modified Dual-Water equations greatly improved the calculated results.

In addition to calculating water saturation, Waxman-Smits and Modified Dual-Water techniques were also used in this study to derive formation water resistivity (Rw) and m and n values in Archie equation. Rw was calculated from core water saturation, core porosity and deep resistivity from AIT log. Equations are as follows:

$$Rw = Sw^2 / (F/Rt - Qv \times B \times Sw) \quad \text{(Waxman-Smits)} \quad (4\text{-}28)$$

$$Rw = (Sw^2 \times (1- Swb)) / (F/Rt - Qv \times B \times Sw) \quad \text{(Modified Dual-Water)} \quad (4\text{-}29)$$

CEC values required in Qv calculation is obtained from the regression equation between density porosity and measured CEC values (equation 4-18). To minimize the thin bed effects, only core data from thick yellow and orange zones (> 1 ft) are selected. Deep resistivity readings suffer more from thin bed effects in white zone and yellow/white mixing zone due to the higher resistivity contrast. The modeled Rw values are shown in Figure 60. Rw values from Waxman-Smits equation are mostly around 0.04-0.05 ohm-m and those from Modified Dual-Water equation around 0.03 to 0.04 ohm-m. The average Rw would be around 0.04 ohm-m which is similar to 0.039 ohm-m from Pickette crossplot technique.

Rt modeling from Waxman-Smits and Modified Dual-Water (MDW) equations was used in this study to derive m and n values in Archie equation.

$$Ro = 1/(1 /(F^* \times Rw) + B \times Qv/F^*) \quad \text{(Waxman-Smits)} \quad (4\text{-}30)$$

$$Rt = 1/(Sw_T^2/(F^* \times Rw) + Sw_T \times B \times Qv/F^*) \quad \text{(Waxman-Smits)} \qquad (4\text{-}31)$$

$$Ro = 1/((1\text{-}Swb)/(Fo \times Rw) + B \times Qv/Fo) \quad \text{(MDW)} \qquad (4\text{-}32)$$

$$Rt = 1/(Sw_T^2 \times (1\text{-}Swb)/(Fo \times Rw) + Sw_T \times B \times Qv/Fo) \quad \text{(MDW)} \qquad (4\text{-}33)$$

$$F^* \text{ (or Fo)} = 1/\phi t^2$$

$$Qv = CEC \times \rho_{ma} \times (1- \phi t)/ \phi t \qquad (4\text{-}17)$$

$$CEC = 0.1802 \times \phi t + 0.052728 \qquad (4\text{-}18)$$

$$n \text{ (Archie)} = \log (Ro/Rt)/\log (Sw)$$

Where,

Ro Wet resistivity when Sw = 100%

Rw is 0.039 ohm-m and B is 20 in modeling. Porosity is modeled from 8% to 55%. Rt value at given Sw and porosity can be calculated. Results were presented in Pickette crossplots (Figure 61 and Figure 62). Six constant Sw lines are generated (100%, 80%, 70%, 60%, 50%, 30%). The slope of the 100% Sw line should represent m value in Archie equation. Value m is 1.64 and 1.72 respectively from Waxman-Smits and Modified Dual-Water techniques, which is close to 1.68 used in Modified Archie equation. Value n in Archie equation is reflected by the distance between the constant Sw line. As shown in Figure 61 and Figure 62, the distance between constant Sw lines increases with the porosity. Therefore, n increases with porosity under constant Sw (Figure 63). Besides, value n generated from different Sw lines is different. For Sw = 50% and porosity = 20%, n values are 1.49 and 1.42 respectively from Waxman-Smits and Modified Dual-Water techniques, which are also close to the n value used in Modified Archie equation (1.56). Therefore, m and n values in Modified Archie equation can be used to approximate Waxman-Smits and/or Modified Dual-Water techniques.

Waxman-Smits

Rw *0hm-m*	*Frequency*
0.01	0
0.02	0
0.03	0
0.04	3
0.05	6
0.06	1
0.07	0
0.08	0

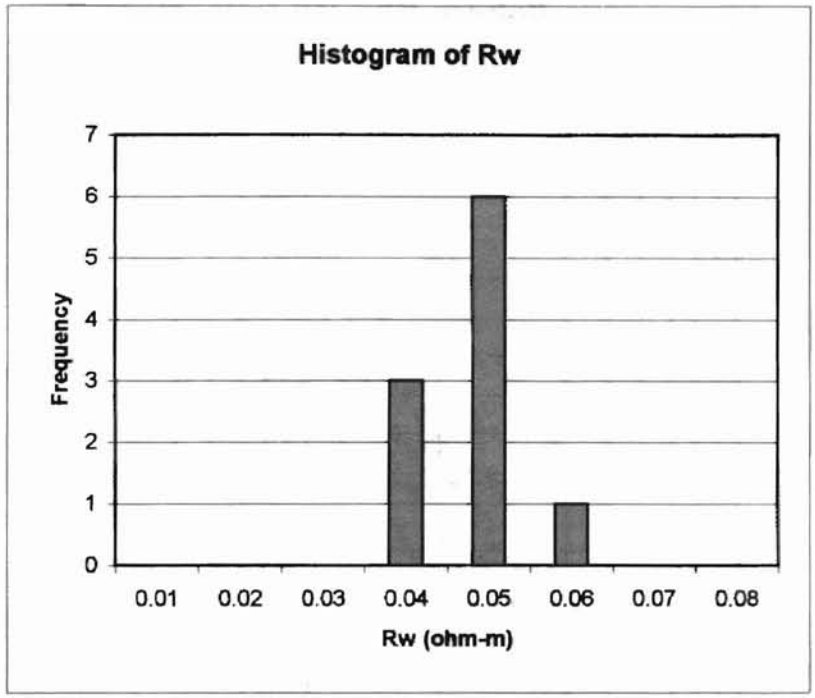

Modified Dual-Water

Rw *0hm-m*	*Frequency*
0.01	0
0.02	0
0.03	3
0.04	6
0.05	1
0.06	0
0.07	0
0.08	0

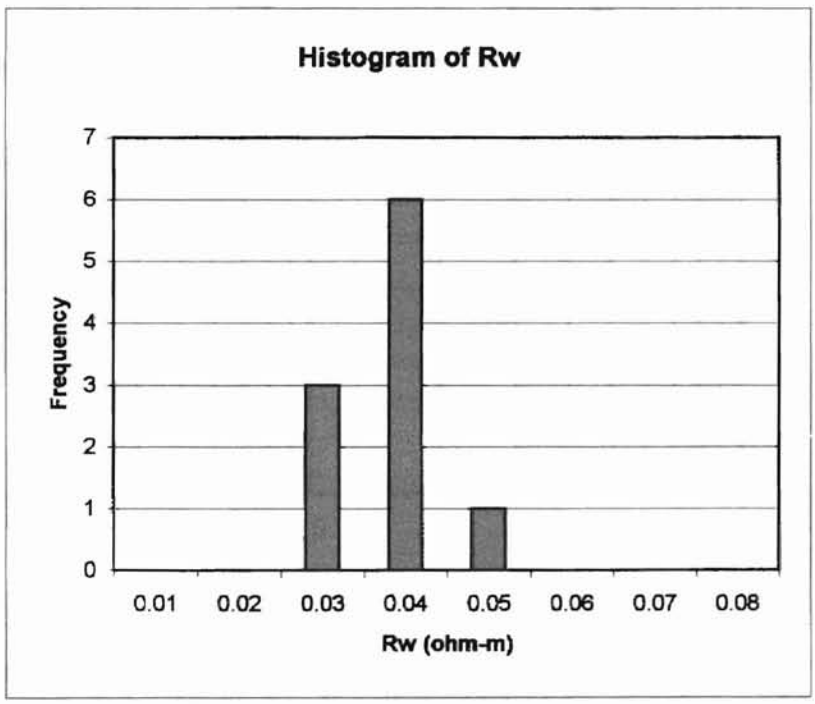

Figure 60. Histogram of Rw calculated from Waxman-Smits and Modified Dual-Water equations in the cored interval.

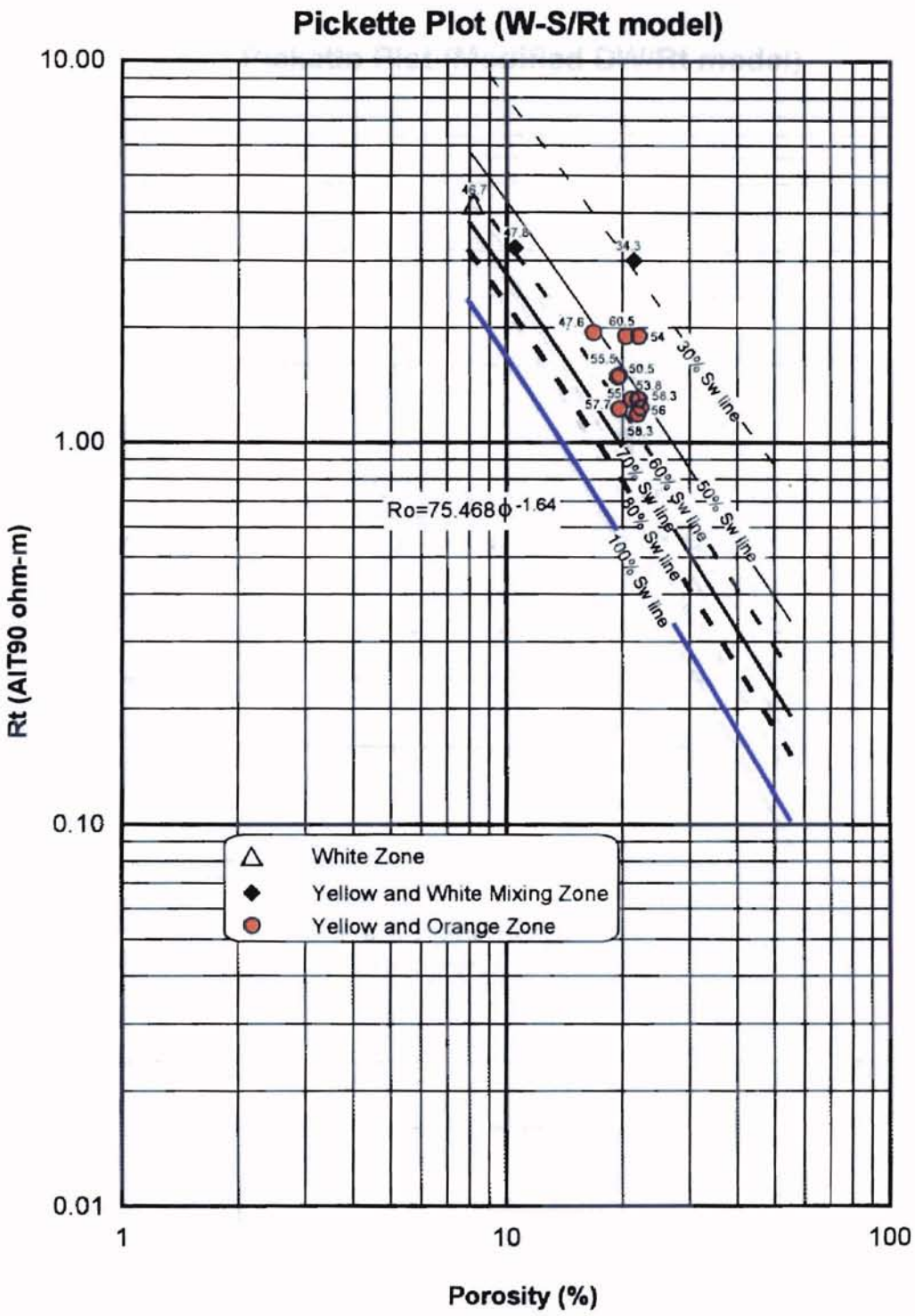

Figure 61. Pickette crossplot of porosity and modeled Rt value from Waxman-Smits model. The slope of the 100% Sw line is equivalent to m value in Archie equation which is 1.64. Saturation exponent (n) in Archie equation is reflected by the distance between constant Sw lines which increases with the porosity.

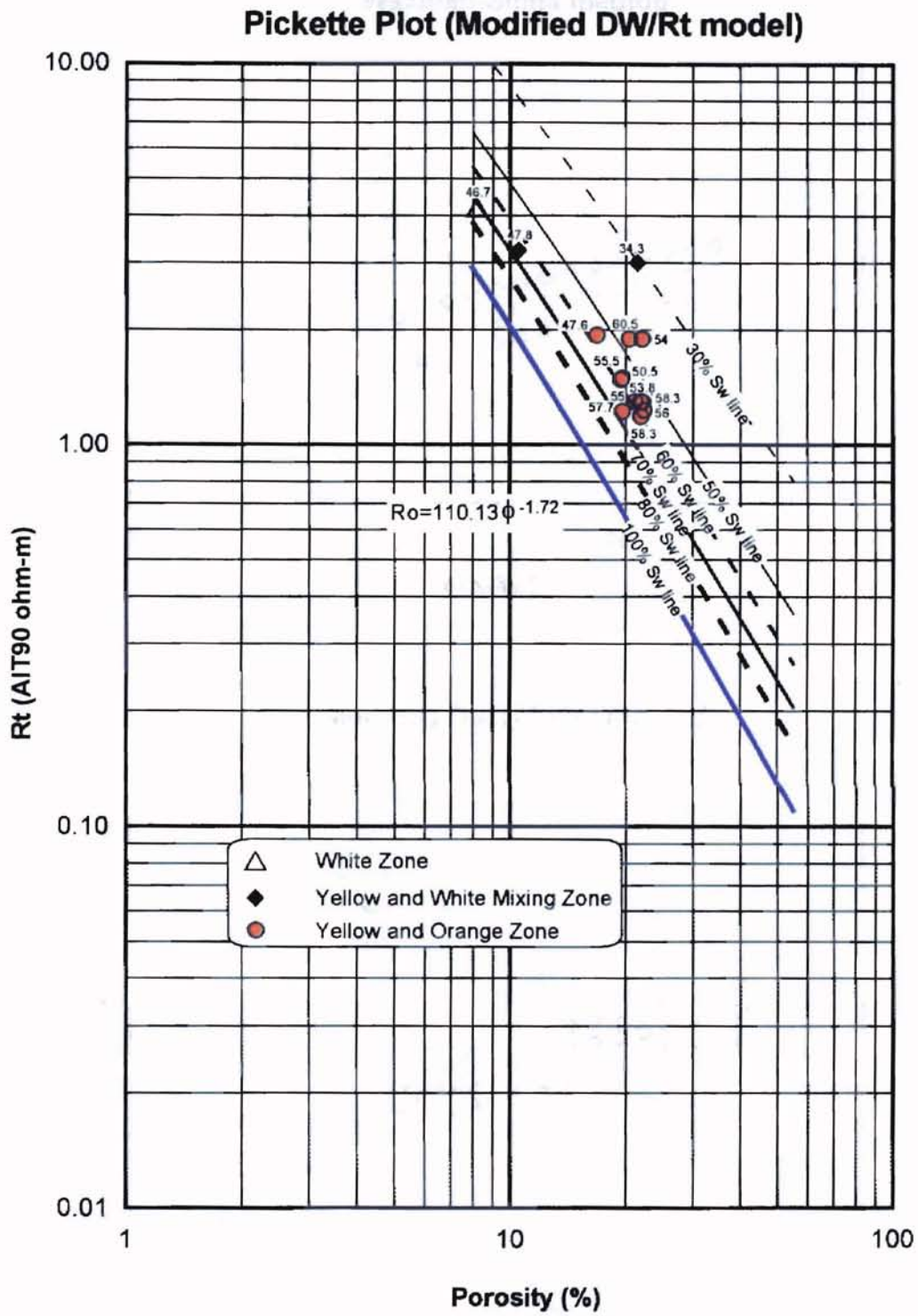

Figure 62. Pickette crossplot of porosity and modeled Rt value from Modified Dual-Water model. The slope of the 100% Sw line is equivalent to m value in Archie equation which is 1.72. Saturation exponent (n) in Archie equation is reflected by the distance between constant Sw lines which increases with the porosity.

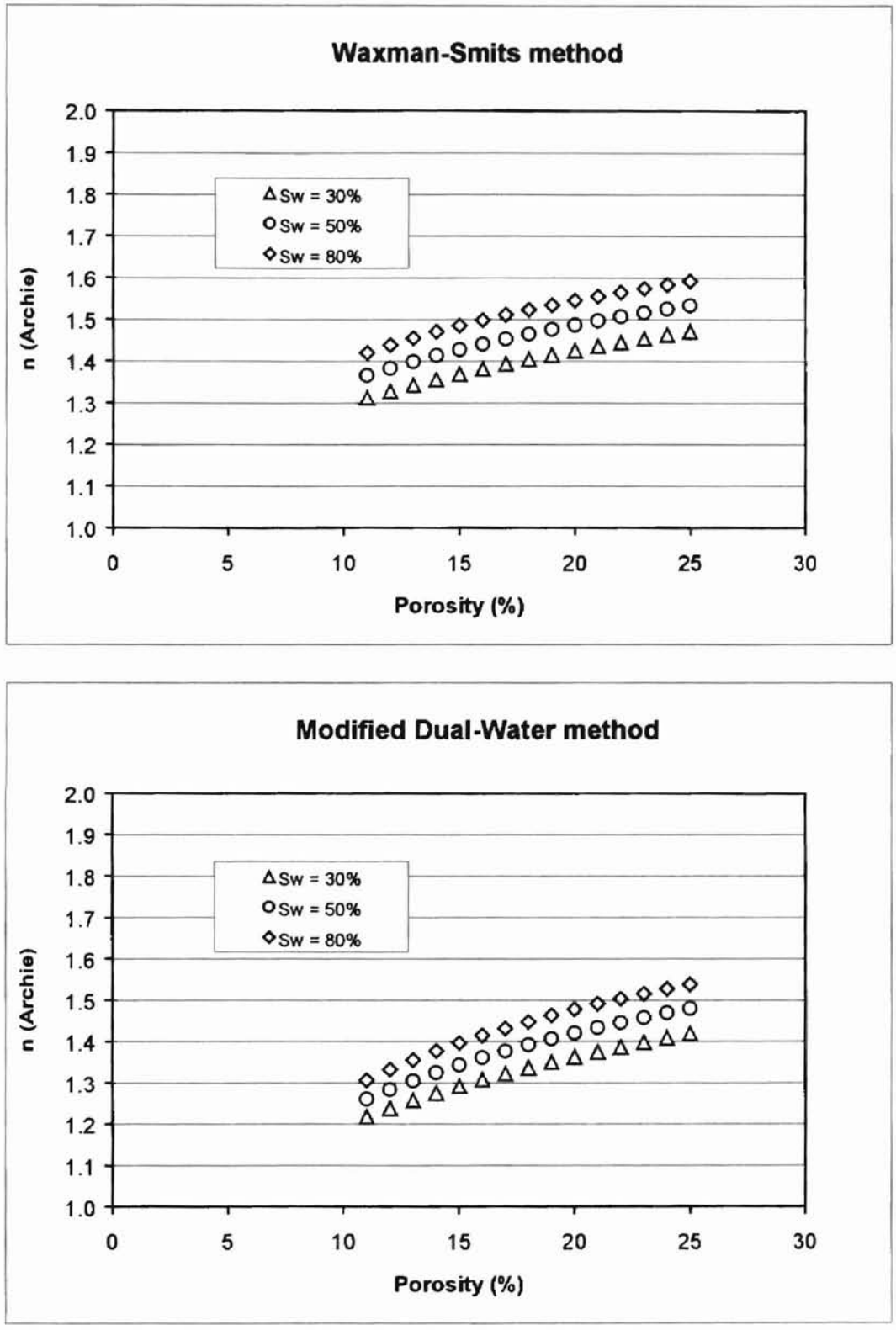

Figure 63. Saturation exponents (n) in Archie equation derived from Waxman-Smits and Modified Dual-Water equations. They vary with porosity and Sw.

CHAPTER V

CONCLUSIONS

Based on the integrated core, petrographic and petrophysical studies on the LR/LC 9900-ft zone, several conclusions are drawn as follows:

1. 9900-ft zone was deposited in a shallow marine shelf environment.
2. The average sandstone compositions were plotted as feldspathic litharenites using the Folk (1974) (QRF) ternary diagram.
3. Vicksburg sandstones have undergone extensive diagenetic modification. The primary diagenetic products are the various kinds of cements and diagenetic clays. Calcite and silica cements are common, which can drastically reduce porosity and permeability in some sandstones. Diagenetic clays include illite-smectite mixed layer clay, illite, kaolite and chlorite, with illite-smectite mixed layer clays being the most abundant.
4. Porosity is dominantly secondary and resulted primarily from the dissolution of feldspar and rock fragments. Micropores are important as revealed by thin section and capillary pressure analysis.
5. High-resolution logs allow the recognition of reservoir and non-reservoir facies greater than 1-ft thick while Formation Micro-imager logs can resolve beds down to inch scale.

6. High-resolution density porosity measurements were very similar to measured core porosity and may be used to estimate total porosity.
7. The low resistivity signatures of the 9900-ft sandstone are mainly generated by the presence of abundant clays, especially I/S mixed-layer clays.
8. Pickette crossplot technique can be used to derive m, n and even Rw values for water saturation interpretation. Resistivity modeling using Waxman-Smits and Modified Dual-Water methods also yields m and n values which are in good agreement with those from Pickette crossplot technique. Reliable results can be achieved using the simple Archie equation modified using the newly determined m, n and Rw values. These m and n values incorporate the average clay correction. Rw value derived from Pickette crossplot may be more reliable than that from measured salinity data. Water samples gathered from gas-bearing zones can be diluted by gas distillate, i.e. fresher.
6. Modified Archie, Waxman-Smits and Modified Dual-Water methods yielded water saturations that match best with those from core analyses. The combination of these three techniques should be effective for the analysis of these sandstones.

REFERENCES

Al-Shaieb, Z., Puckette, J., Blubaugh, P., Deyhim, P. and Li, H.,1998, Characterization of the low-Contrast 9900-ft sandstone, Vicksburg Formation, TCB field, Kleberg County, Texas: Report for the Gas Research Institute.

Al-Shaieb, Z., Puckette, J., Blubaugh, P., Deyhim, P. and Li, H., 2000, Identification of reservoir and intra-seal facies in the Vicksburg Formation, TCB Field, Kleberg Co, TX : using Formation Micro-imaging logs (FMI), fluid inclusion stratigraphy (FIS) and capillary pressure measurements: Report for the Gas Research Institute.

Archie, G. E., 1942, The electrical resistivity log as an aid in determining some reservoir characteristics: Petroleum Technology, v. 5, no. 1, p. 54-62.

Asquith, G., 1982, Basic well log analysis for geologists, AAPG Methods in Exploration Series Number 3, p. 5.

Berg, R. R., Marshall, W. D., and Shoemaker, P. W., 1979, Structural and depositional history, McAllen Ranch Field, South Texas: GCAGS Transactions, v. 29, p. 24-28.

Cebell, W. A., and Chilingarian, G. V., 1972, Some data on compressibility and density anomalies in halloysite, hectorite, and illite clays: AAPG Bulletin, v. 56, p. 796 – 802.

Clavier, C., Coates, G., and Dumanoir, J., 1977, The theoretical and experimental bases for the "dual water" model for the interpretation of shaly sands: SPE Paper No. 6859.

Clavier, C., Coates, G., and Dumanoir, J., 1984, Theoretical and experimental bases for the dual-water model for interpretation of shaly sands: SPEJ, v. 24, p. 153-168.

Coates, G. R., Miller, M., Gillen, M., Henderson, G., 1991, The MRIL in Conoco 33-1 — An investigation of a new magnetic resonance imaging log: SPWLA, 24p.

Coleman, J. M. C., 1990, Depositional systems and tectonic/eustatic history of the Oligocene Vicksburg episode of the Northern Gulf Coast: Ph.D. dissertation, The University of Texas at Austin.

Darling, H. L., and Sneider, R. M., 1992, Production of low resistivity, low contrast reservoirs, offshore Gulf of Mexico basin: Gulf Coast Association of Geological Societies Transactions, v. 42, p. 73-88.

Desbrandes, R., 1985, Encyclopedia of well logging, Gulf Publishing Company, p. 280.

Dewan, J. T., 1983, Essentials of modern open-hole log interpretation: Tulsa, Oklahoma, PennWell Publishing Co.

Dresser Atlas, 1979, Log interpretation charts: Houston, Dresser Industries, Inc., 107 p.

Fett, T. H., 1980, Evaluating and logging of tight rocks of south Texas: World Oil, v. 190, p. 63-72.

Fisher, W. L., Proctor Jr., C. V., Galloway, W. E., and Nagle, J. S., 1970, Depositional systems in the Jackson Group of Texas — their relationship to oil, gas, and uranium: GCAGS transactions, v. 20, p. 234-261.

Grim, R. E., 1968, Clay mineralogy (2d edition), New York and London, McGraw-Hill Book Co.

Han, J. H., 1981, Genetic stratigraphy and associated growth structures of the Vicksburg Formation, South Texas: Ph.D. dissertation, University of Texas, Austin, Texas.

Humphrey, J., 1986, Depositional environments and diagenesis of the Oligocene Vicksburg Formation in Lyda and North Rincon fields, Starr County, Texas: GCAGS Transactions, v. 36, p. 171-179.

International Oil Scouts Association, 1997: International Oil and Gas Development Yearbook, Review of 1995 Production, v. 66, 1071p.

Jennings, J. B., 1987, Capillary pressure techniques: application to exploration and development geology: AAPG Bulletin, v. 71, p. 1196 – 1209.

Johnson, W. L., and Linke, W. A., 1977, Some practical application to improve formation evaluation of sandstones in the Mackenzie delta: Transactions of the CWLS Sixth formation evaluation symposium.

Klass, M. J, 1981, Diagenesis and development of secondary porosity in the Vicksburg Sandstone, McAllen Ranch Field, Hidalgo County, Texas: Master thesis, Texas A & M University, College Station, Texas.

Klass, M. J., Kersey, D. G., Berg, R. R., and Tieh, T. T., 1981, Diagenesis and secondary porosity in Vickburg sandstones, McAllen Ranch Field, Hidalgo County, Texas: GCAGS Transactions, v. 31, p. 115-123

Langford, R. P. and Combes, J. M., 1994, Depositional environments of unstable shelf-margin deltas of the Oligocene Vicksburg Formation, McAllen Ranch Field, South Texas: University of Texas at Austin, Bureau of Economic Geology, Report of Investigation No. 219.

Langford, R. P., and Lynch, F. L., 1990, Diagenesis and cement fabric of gas reservoirs in the Oligocene Vicksburg Formation, McAllen Ranch Field, Hidalgo County, Texas: GCAGS Transactions, v. 40, p. 451-458.

Lomax, J., and Howard, A., 1994, New logging tool identifies permeability in shaley sands: Technology, Oil and Gas Journal, v. 92, p. 104-108

Loucks, R. G., 1978, Sandstone distribution and potential for geopressured geothermal energy production in the Vicksburg Formation along the Texas Gulf Coast: GCAGS Transactions, v. 28, p. 239-271.

Magara, K., 1968, Compaction and migration of fluids in Miocene mudstones, Nagaoka Plain, Japan: AAPG Bulletin, v. 52, p. 2466 – 2501.

Miller, K. G., 1989, Aspects of Middle Eocene – Early Oligocene Marine stable isotopes, planktonic biostratigraphy, and magnetostratigraphy: G. S. A. Abstracts with Programs, 1989 Annual Meeting, v. 21/6, p. A87.

Miller, K. G., Fairbanks, R. G., and Mountain, G. S., 1987, Tertiary oxyen isopope synthesis, sea level history, and continental margin erosion: Paleoceanography, v. 2/1, p. 1-19.

Pasley, M.A., and Hazal, J. E., 1990, Use of organic petrology and graphic correlation of biostratigraphic data in sequence stratigraphic interpretation: example from the Eocene-Oligocene boundary section, St Stephen Quarry, Alabama: GCAGS Transactions, v. 40, p. 661-683.

Petroleum Information/Dwights, 1998: Natural Gas Well Production Histories.

Pomerol, C., and Premoli-Silva, I., 1986, The Eocene-Oligocene transition: events and boundary, *in* Pomerol, C. and Premoli-Silva, I., (eds.), Terminal Eocene Events: New York, Elsevier, p. 1-24.

Poupon, A., and Leveaux, J., 1971, Evaluation of water saturation in shaly formations: The Log Analyst, v. 12, no. 4, p. 3-8.

Richman, D. L., Milliken, K. K., Loucks, R. G., and Dodge, M. M., 1980, Mineralogy, diagenesis, and porosity in Vicksburg sandstones, McAllen Ranch Field, Hidalgo County, Texas: GCAGS Transactions, v. 30, p. 473-481.

Ricou, L. E., deLepinay, B. M., and Marcoux, J., 1986, Evolution of the Tethyan seaways and implications for the oceanic circulation around the Eocene-Oligocene boundary, *in* Pomerol, C. and Premoli-Silva, I., (eds.), Terminal Eocene Events: New York, Elsevier, p. 387-394.

Schlumberger, 1972, Log interpretation, Volume 1-Principles: Schlumbger Ltd., New York, p. 113.

Schlumberger, 2000, Combinable Magnetic Resonance tool reliably indicates water-free production and reveals hard-to-find pay zones: CMR brochure.

Schowalter, T. T., 1979, Mechanics of Secondary Hydrocarbon Migration and Entrapment: AAPG Bulletin, v. 63 , p. 723 - 760.

Sneider, R. M. and Kulha, J. T., 1995, Low-resistivity, low contrast productive sands, workshop.

Taylor, D. A. and Al-Shaieb, Z., 1986, Oligocene Vicksburg sandstones of the Tijirina-Canales- Blucher Field: a south Texas geologic Jambalaya: GCAGS transactions, v. 36, p. 315-339.

Thomas, E. C., and Stieber, S. J., 1975, The distribution of shale in sandstones and its effect upon porosity: Paper T, Society of Professional Well Log Analysts 16th Annual Logging Symposium, 15 p.

Thomeer, J. H. M., 1960, Introduction of a pore geometrical factor defined by the capillary pressure curve: AIME Petroleum Transactions, v. 219, p. 354 – 358.

Vavra, C. L., Kaldi, J. G., and Sneider, R. M., 1992, Geological applications of capillary pressure: AAPG Bulltin, v. 76, p. 840 – 850.

Waxman, M. H. and Smits, L. J. M., 1968, Electrical conductivities in oil-bearing shaly sands: Society of Petroleum Engineers Journal, v. 8, no. 2, p. 107-122.

Waxman, M. H. and Thomas, E. C., Feb. 1974, Electrical conductivities in shaly sands: JPT, p. 213-225.

Wilson, M. D. and Pittman, E. D., 1977, Authigenic clays in sandstones: recognition and influence on reservoir properties and paleoenvironmental analysis: J. sediment. Petrol 47, p 3-31.

Winker, C. D. and Edwards, M. B., 1983, Unstable progradational clastic shelf margins, *in* Stanley, D. J., and Moore, G. T. (eds.), The Shelfbreak Critical Interface on Continental Margins, p. 139-157.

Winker, C. D., 1982, Cenozoic shelf margins, northwestern Gulf of Mexico: GCAGS Transactions, v. 32, p. 427-448.

APPENDIX A

CORE PETROLOGS

A. T. Canales 81
OLIGOCENE VICKSBURG
AGE/STRATIGRAPHIC UNIT
Shallow Marine Shelf
ENVIRONMENT
9920
9915
9910
9905
DEPTH/THICKNESS
S.P.
LITHOLOGY
SEDIMENTARY STRUCTURES
SPECIFIC
DK GRAY
GRAY
BROWN
GREEN
RED
VARIEGATED
COLOR
CLAY/MUD/F SILT
C. SILT
VF SAND
F SAND
M SAND
C SAND
VC SAND
GRAN.-PEBBLE
COBBLE-BOULDER
Sandstone
GRAIN SIZE
POOR
FAIR
GOOD
SORTING
POROSITY %
10 20 30
Core Injection
Neutron
Density
Thin Section
TYPE
QUARTZ
FELDSPAR
ROCK FRAG
CLAY(C)CARB(CA)CLAST
DETRITAL/ ALLOGENIC
PLANT
INVERT
FOSSILS
GLAUCONITE
CLAY MINERALS
CARBONATE
SILICA
SULFATE
SULFIDES
PENE-CONTEMPORANEOUS AUTHOGENIC
CONSTITUENTS
ROCK CLASSIFICATION
SA
FL
LAM
SL
SL
SA
SL
SL
Siderite
SAMPLE
REMARKS

A. T. Canales 81
AGE/STRATIGRAPHIC UNIT
OLIGOCENE VICKSBURG
ENVIRONMENT
Shallow Marine Shelf
DEPTH/THICKNESS
9925
9930
9935
9940
S.P.
LITHOLOGY
SEDIMENTARY STRUCTURES
COLOR
SPECIFIC
DK GRAY
GRAY
BROWN
GREEN
RED
VARIEGATED
GRAIN SIZE
CLAY/MUD/F SILT
C. SILT
VF SAND
F SAND
M SAND
C SAND
VG SAND
GRAN.-PEBBLE
COBBLE-BOULDER
Sandstone
SORTING
POOR
FAIR
GOOD
POROSITY %
Core Injection
Neutron
Density
Thin Section
10
20
30
TYPE
CONSTITUENTS
DETRITAL/ ALLOGENIC
QUARTZ
FELDSPAR
ROCK FRAG
CLAY/CCARB(CA)CLAST
FOSSILS
PLANT
INVERT
AUTHIGENIC
PENE-CONTEMPORANEOUS
CLAY MINERALS
CARBONATE
SILICA
SULFATE
SULFIDES
ROCK CLASSIFICATION
SAMPLE
REMARKS
SA
FL
S
O
Minor burrowing
Siderite
The upper part is coarser and is cemented by calcite.

A. T. Canales 85
OLIGOCENE VICKSBURG
AGE/STRATIGRAPHIC UNIT
Shallow Marine Shelf
ENVIRONMENT
10440
10430
10420
DEPTH/THICKNESS
S.P.
LITHOLOGY
SEDIMENTARY STRUCTURES
COLOR
SPECIFIC
DK GRAY
GRAY
BROWN
GREEN
RED
VARIEGATED
GRAIN SIZE
CLAY/MUD/F SILT
C. SILT
VF SAND
F SAND
M SAND
C SAND
VC SAND
GRAN.-PEBBLE
COBBLE-BOULDER
Sandstone
SORTING
POOR
FAIR
GOOD
POROSITY %
10
20
30
Core Injection
Neutron
Density
Thin Section
TYPE
CONSTITUENTS
DETRITAL/ ALLOGENIC
QUARTZ
FELDSPAR
ROCK FRAG
CLAY(C)CARB(CA)CLAST
FOSSILS
PLANT
INVERT
PENE-CONTEMPORANEOUS AUTHOGENIC
GLAUCONITE
CLAY MINERALS
CARBONATE
SILICA
SULFATE
SULFIDES
ROCK CLASSIFICATION
SAMPLE
REMARKS
BURROWING
FLOWAGE

A. T. Canales 85

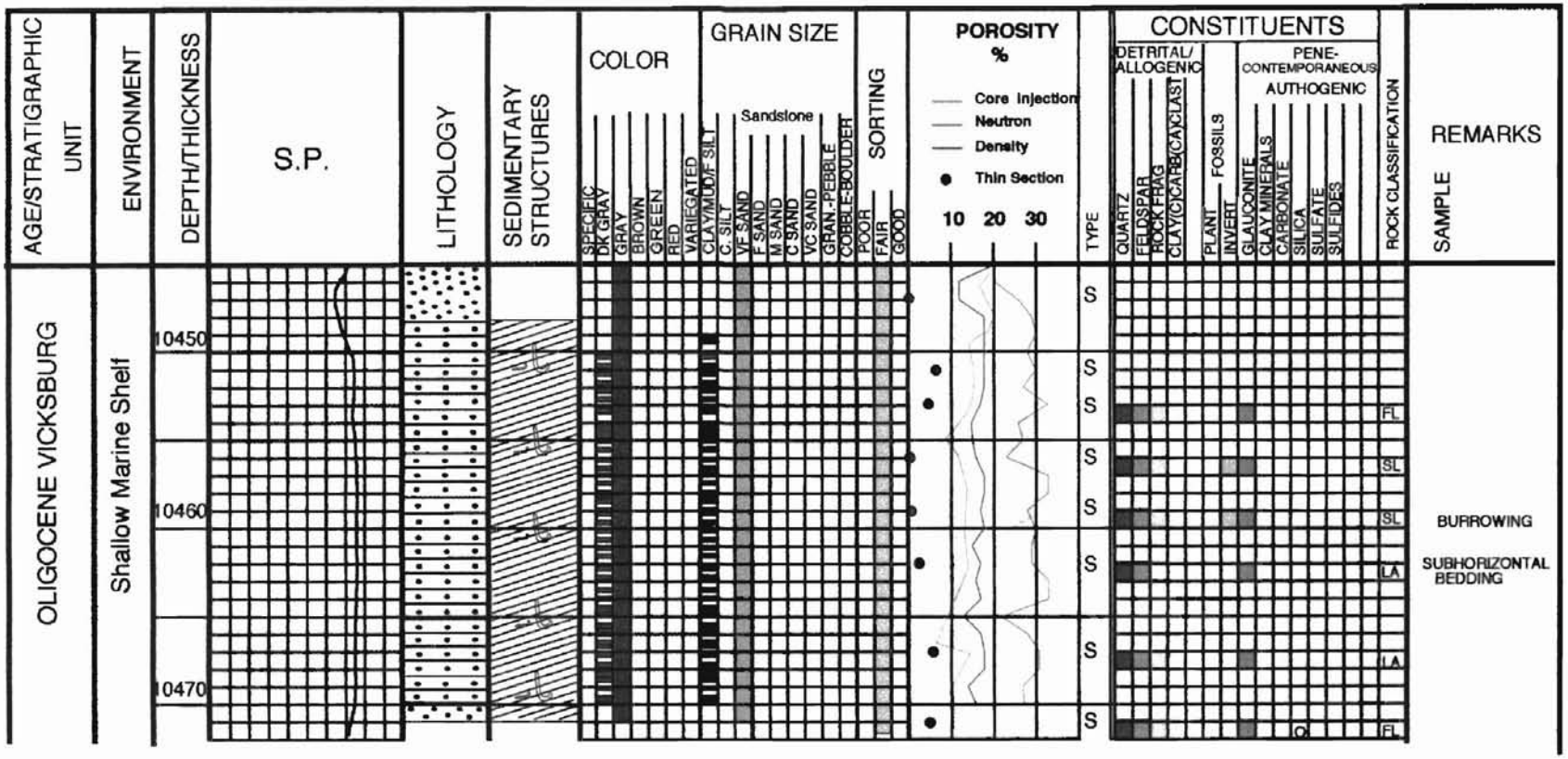

APPENDIX B

PETROGRAPHY

THIN SECTION ANALYSES

Well Name: A.T. Canales #81 **Field: TCB** **Company: ORYX Energy**
County: Kleberg **Location: Survey 341, A-81**

	Thin Section ID	*OV9901*	*OV9905*	*OV9908*	*OV9910*	*OV9912*	*OV9916*	*OV9917*
	Core Depth (feet)	*9901*	*9905*	*9908*	*9910*	*9912*	*9916*	*9917*
	Logging Depth (feet)	*9889*	*9893*	*9896*	*9898*	*9900*	*9904*	*9905*
DETRITAL CONSTITUENTS	**Quartz**							
	Monocrystalline	43.2	43.0	54.3	43.2	43.4	39.7	36.1
	Polycrystalline	tr	tr	tr	tr	tr	tr	tr
	Feldspar							
	Microcline	0.0	0.0	0.0	0.0	0.0	0.0	0.0
	Orthoclase	0.0	0.0	0.0	0.0	0.0	0.0	0.0
	Plagioclase	2.9	4.7	5.3	3.7	2.9	11.3	8.8
	Rock Fragments							
	Argillaceous	0.4	0.0	0.1	0.6	7.3	9.7	4.1
	Chert	0.9	1.0	0.2	0.5	0.1	0.5	0.2
	Carbonate	0.0	0.0	0.0	0.0	0.0	0.0	0.0
	Metamorphic	0.2	0.3	0.4	0.0	0.1	0.2	tr
	Volcanic	6.5	7.7	4.2	5.9	1.3	0.4	8.2
	Other Grains							
	Shell Fragments	0.0	0.0	tr	0.0	tr	0.0	0.0
	Crinoids	0.0	0.0	tr	0.0	tr	0.0	0.0
	Forams	0.0	0.0	0.0	0.0	0.0	0.0	0.0
	Glauconite	1.2	1.1	0.6	0.8	1.1	0.9	0.2
	Phosphate	0.0	0.0	0.0	0.0	0.0	0.0	0.0
	Muscovite	0.0	tr	0.2	0.2	0.5	0.2	0.5
	Biotite	0.0	tr	0.0	0.0	0.0	tr	tr
	Pyrite	0.1	0.6	0.0	0.5	0.0	0.0	0.0
	Zircon	0.1	0.0	0.0	0.0	0.0	0.1	0.1
	Tourmaline	0.0	0.1	0.6	tr	0.0	0.1	0.3
DETRITAL MATRIX								
	Clayey	0.0	0.0	0.0	3.1	0.0	0.0	2.5
	Silty	0.0	0.0	0.0	0.0	0.0	0.0	0.0
	Limy	0.0	0.0	0.0	0.0	0.0	0.0	0.0
DIAGENETIC CONSTITUENTS	**Cements**							
	Quartz Overgrowth	0.6	0.0	1.1	0.0	0.0	0.0	0.0
	Chalcedony	0.0	0.0	0.0	0.0	0.0	0.0	0.0
	Calcite	31.4	39.9	4.0	1.7	2.1	4.0	1.3
	Dolomite	0.0	0.0	0.0	0.0	0.0	0.0	0.0
	Siderite	0.0	0.0	0.0	0.0	0.0	0.0	0.0
	Hematite	0.0	0.0	0.0	0.0	0.0	0.0	0.0
	Phosphate	0.0	0.0	0.0	0.0	0.0	0.0	0.0
	Anhydrite	0.0	0.0	0.0	0.0	0.0	0.0	0.0
	Authigenic Clays							
	Kaolinite	0.3	0.0	2.0	1.4	0.5	7.4	12.2
	Illite	0.0	0.0	0.0	0.0	0.0	0.0	0.0
	Smectite	0.0	0.0	0.0	0.0	0.0	0.0	0.0
	Chlorite	0.0	0.0	0.0	0.0	0.0	0.0	0.0
	I/S Mixed Layer	8.6	1.3	14.9	26.6	26.0	9.7	12.0
	OTHERS							
	Organics							

THIN SECTION ANALYSES

Well Name: A.T. Canales #81 **Field: TCB** **Company: ORYX Energy**
County: Kleberg **Location: Survey 341, A-81**

	Thin Section ID	*OV9920*	*OV9925*	*OV9929*	*OV9934*	*OV9936.5*	*OV9940*	*OV9941.5*
	Core Depth (feet)	*9920*	*9925*	*9929*	*9934*	*9936.5*	*9940*	*9941.5*
	Logging Depth (feet)	*9908*	*9913*	*9917*	*9922*	*9924.5*	*9928*	*9929.5*
DETRITAL CONSTITUENTS	**Quartz**							
	Monocrystalline	45.2	49.2	42.6	33.7	36.1	35.6	49.8
	Polycrystalline	tr	tr	tr	tr	tr	tr	tr
	Feldspar							
	Microcline	0.0	0.0	0.0	0.0	0.0	0.0	0.0
	Orthoclase	0.0	0.0	0.0	0.0	0.0	0.0	0.0
	Plagioclase	7.4	7.7	4.8	9.3	8.6	7.4	4.0
	Rock Fragments							
	Argillaceous	2.2	0.7	5.8	8.6	7.0	4.7	0.5
	Chert	0.7	0.2	0.4	0.8	0.3	0.3	0.0
	Carbonate	0.0	0.0	0.0	0.0	0.0	0.0	0.0
	Metamorphic	0.0	0.7	0.0	0.2	tr	0.1	0.0
	Volcanic	4.0	5.0	6.4	3.8	4.4	2.9	3.2
	Other Grains							
	Shell Fragments	0.0	0.0	0.0	tr	0.0	tr	0.0
	Crinoids	0.0	0.0	0.0	tr	0.0	0.0	0.0
	Forams	0.0	0.0	0.0	tr	0.0	tr	0.0
	Glauconite	0.6	0.9	0.8	0.5	0.3	0.1	0.7
	Phosphate	0.0	0.0	0.0	0.0	0.0	0.0	0.0
	Muscovite	0.2	0.2	tr	0.1	0.3	0.4	tr
	Biotite	0.0	0.0	tr	tr	0.1	tr	tr
	Pyrite	0.0	0.0	0.0	0.0	0.1	0.4	0.0
	Zircon	0.0	0.0	0.0	tr	tr	0.0	0.2
	Tourmaline	tr	tr	0.8	0.2	0.6	0.1	0.0
DETRITAL MATRIX								
	Clayey	4.9	2.8	0.0	5.2	4.6	9.3	0.0
	Silty	0.0	0.0	0.0	0.0	0.0	0.0	0.0
	Limy	0.0	0.0	0.0	0.0	0.0	0.0	0.0
DIAGENETIC CONSTITUENTS	**Cements**							
	Quartz Overgrowth	0.0	0.2	0.0	0.0	tr	0.0	0.0
	Chalcedony	0.0	0.0	0.0	0.0	0.0	0.0	0.0
	Calcite	7.7	9.9	1.9	6.8	5.4	3.4	37.3
	Dolomite	0.0	0.0	0.0	0.0	0.0	0.0	0.0
	Siderite	0.1	0.0	tr	0.0	0.0	0.0	0.0
	Hematite	0.0	0.0	0.0	0.0	0.0	0.0	0.0
	Phosphate	0.0	0.0	0.0	0.0	0.0	0.0	0.0
	Anhydrite	0.0	0.1	0.0	0.0	0.0	0.0	0.0
	Authigenic Clays							
	Kaolinite	6.1	5.1	tr	0.2	tr	2.1	4.3
	Illite	0.0	0.0	0.0	0.0	0.0	0.0	0.0
	Smectite	0.0	0.0	0.0	0.0	0.0	0.0	0.0
	Chlorite	0.0	0.0	0.0	0.0	0.0	0.0	0.0
	I/S Mixed Layer	9.8	10.1	29.3	27.3	24.7	21.1	0.0
	OTHERS							
	Organics							

THIN SECTION ANALYSES

Well Name: A.T. Canales #85 **Field: TCB** **Company: ORYX Energy**
County: Kleberg **Location: Survey 341, ABS-81**

	Thin Section ID	*OV10424*	*OV10427*	*OV10431*	*OV10432*	*OV10442*	*OV10447*	*OV10451*
	Core Depth (feet)	*10424*	*10427*	*10431*	*10432*	*10442*	*10447*	*10451*
	Logging Depth (feet)	*10414*	*10417*	*10421*	*10422*	*10432*	*10437*	*10441*
DETRITAL CONSTITUENTS	**Quartz**							
	Monocrystalline	48.0	54.0	51.5	40.1	58.5	32.0	49.6
	Polycrystalline	tr	tr	tr	tr	tr	tr	tr
	Feldspar							
	Microcline	0.0	tr	tr	0.0	0.0	0.0	0.0
	Orthoclase	0.0	0.0	0.0	0.0	0.0	0.0	0.0
	Plagioclase	8.0	5.3	4.4	3.9	5.3	2.3	6.2
	Rock Fragments							
	Argillaceous	0.2	0.0	0.1	10.9	0.0	tr	0.5
	Chert	1.1	0.8	1.2	0.1	1.3	tr	0.1
	Carbonate	0.0	0.0	0.0	0.0	0.0	0.0	0.0
	Metamorphic	0.0	0.1	0.0	0.0	0.0	0.0	0.0
	Volcanic	7.1	9.3	10.4	6.8	7.9	7.9	8.1
	Other Grains							
	Shell Fragments	tr	0.0	tr	0.0	0.0	0.0	tr
	Crinoids	tr	0.0	tr	0.0	0.0	0.0	tr
	Forams	tr	0.0	0.0	0.0	0.0	0.0	0.0
	Glauconite	0.2	0.8	0.6	1.5	0.6	1.4	1.1
	Phosphate	0.0	0.0	0.0	0.0	0.0	0.0	0.0
	Muscovite	tr	0.3	0.1	0.4	tr	0.1	0.1
	Biotite	0.0	tr	0.0	0.3	tr	tr	0.2
	Pyrite	0.0	0.0	0.1	0.0	0.1	0.0	0.0
	Zircon	0.0	0.1	0.0	0.3	0.0	0.0	0.0
	Tourmaline	0.1	0.0	0.1	0.0	0.1	0.0	0.1
DETRITAL MATRIX								
	Clayey	0.0	0.0	0.0	0.0	0.0	0.0	2.9
	Silty	0.0	0.0	0.0	0.0	0.0	0.0	0.0
	Limy	0.0	0.0	0.0	0.0	0.0	0.0	0.0
DIAGENETIC CONSTITUENTS	**Cements**							
	Quartz Overgrowth	0.0	1.3	0.0	0.0	3.8	0.0	0.0
	Chalcedony	0.0	0.0	0.0	0.0	0.0	0.0	0.0
	Calcite	1.6	25.9	6.7	9.6	14.1	55.1	4.2
	Dolomite	0.0	0.0	0.0	0.0	0.0	0.0	0.0
	Siderite	0.3	0.0	0.2	0.0	0.1	0.9	0.0
	Hematite	0.0	0.0	0.0	0.0	0.0	0.0	0.0
	Phosphate	0.0	0.0	0.0	0.0	0.0	0.0	0.0
	Anhydrite	0.0	0.0	0.0	0.0	0.0	0.0	0.0
	Authigenic Clays							
	Kaolinite	0.1	tr	0.0	0.0	0.4	0.0	0.0
	Illite	0.0	0.0	0.0	0.0	0.0	0.0	0.0
	Smectite	0.0	0.0	0.0	0.0	0.0	0.0	0.0
	Chlorite	0.0	0.0	0.0	0.0	0.0	0.0	0.0
	I/S Mixed Layer	23.1	tr	8.9	16.6	0.0	0.0	20.4
	OTHERS							
	Organics							

THIN SECTION ANALYSES

Well Name: A.T. Canales #85 **Field: TCB** **Company: ORYX Energy**
County: Kleberg **Location: Survey 341, ABS-81**

	Thin Section ID	*OV10453*	*OV10456*	*OV10459*	*OV10462*	*OV10467*	*OV10471*
	Core Depth (feet)	*10453*	*10456*	*10459*	*10462*	*10467*	*10471*
	Logging Depth (feet)	*10443*	*10446*	*10449*	*10452*	*10457*	*10461*
DETRITAL CONSTITUENTS	**Quartz**						
	Monocrystalline	39.5	32.0	19.9	47.1	37.9	46.1
	Polycrystalline	tr	tr	tr	tr	tr	tr
	Feldspar						
	Microcline	0.0	0.0	0.0	0.0	0.0	0.0
	Orthoclase	0.0	0.0	0.0	0.0	0.0	0.0
	Plagioclase	5.5	1.9	0.9	1.8	4.2	4.8
	Rock Fragments						
	Argillaceous	0.1	0.0	0.0	6.6	1.4	0.8
	Chert	0.3	0.0	tr	0.0	0.5	0.3
	Carbonate	0.0	0.0	0.0	0.0	0.0	0.0
	Metamorphic	0.0	0.0	0.0	0.0	0.0	0.0
	Volcanic	10.8	4.1	1.6	11.0	10.9	12.0
	Other Grains						
	Shell Fragments	0.0	tr	tr	0.0	0.0	0.0
	Crinoids	0.0	tr	tr	0.0	0.0	0.0
	Forams	0.0	tr	0.0	0.0	0.0	0.0
	Glauconite	1.0	1.0	0.5	0.5	0.9	0.8
	Phosphate	0.0	0.0	0.0	0.0	0.0	0.0
	Muscovite	tr	0.1	0.1	0.0	0.1	tr
	Biotite	tr	0.2	0.1	0.3	0.1	0.1
	Pyrite	0.0	0.0	0.0	0.0	0.0	0.0
	Zircon	0.1	0.0	0.0	0.0	0.0	0.1
	Tourmaline	0.5	tr	tr	0.0	0.2	0.4
DETRITAL MATRIX							
	Clayey	22.4	55.1	32.3	27.9	0.0	0.0
	Silty	0.0	0.0	0.0	0.0	0.0	0.0
	Limy	0.0	0.0	0.0	0.0	0.0	0.0
DIAGENETIC CONSTITUENTS	**Cements**						
	Quartz Overgrowth	0.0	0.0	0.0	0.0	0.0	0.9
	Chalcedony	0.0	0.0	0.0	0.0	0.0	0.0
	Calcite	6.6	5.3	1.0	2.0	1.1	28.8
	Dolomite	0.0	0.0	0.0	0.0	0.0	tr
	Siderite	0.5	0.0	42.6	0.0	0.0	0.0
	Hematite	0.0	0.0	0.0	0.0	0.0	0.0
	Phosphate	0.0	0.0	0.0	0.0	0.0	0.0
	Anhydrite	0.0	0.0	0.0	0.0	0.0	0.0
	Authigenic Clays						
	Kaolinite	0.0	0.0	0.0	0.0	0.0	0.0
	Illite	0.0	0.0	0.0	0.0	0.0	0.0
	Smectite	0.0	0.0	0.0	0.0	0.0	0.0
	Chlorite	0.0	0.0	0.0	0.0	0.0	0.0
	I/S Mixed Layer	8.1	0.0	0.0	0.6	36.7	0.0
	OTHERS						
	Organics						

THIN SECTION ANALYSES

Well Name: A.T. Canales #81 **Field: TCB** **Company: ORYX Energy**
County: Kleberg **Location: Survey 341, A-81**

Thin Section ID	*OV9901*	*OV9905*	*OV9908*	*OV9910*	*OV9912*	*OV9916*	*OV9917*
Core Depth (feet)	*9901*	*9905*	*9908*	*9910*	*9912*	*9916*	*9917*
Logging Depth (feet)	*9889*	*9893*	*9896*	*9898*	*9900*	*9904*	*9905*
TOTAL DETRITAL	55.5	58.6	65.9	55.4	56.6	63.1	58.5
TOTAL QUARTZ	43.8	43.0	55.4	43.2	43.4	39.7	36.1
Quartz Grains	43.2	43.0	54.3	43.2	43.4	39.7	36.1
TOTAL Q, F, R	54.1	56.7	64.5	53.9	55.0	61.8	57.4
Quartz (%)	79.9	75.8	84.2	80.1	78.9	64.2	62.9
Feldspar (%)	5.4	8.3	8.2	6.9	5.2	18.3	15.3
Rock Fragments (%)	14.8	15.9	7.6	13.0	15.9	17.5	21.8
Total (%)	100.0	100.0	100.0	100.0	100.0	100.0	100.0
TOTAL CLAYS	8.9	1.3	16.9	31.1	26.5	17.1	26.7
TOTAL CEMENTS	32.0	39.9	5.1	1.7	2.1	4.0	1.3
Carbonate cements	31.4	39.9	4.0	1.7	2.1	4.0	1.3
Quartz Cements	0.6	0.0	1.1	0.0	0.0	0.0	0.0
POROSITY							
Primary Porosity	tr	tr	tr	tr	tr	tr	tr
Secondary Porosity	3.6	0.3	12.1	11.8	14.8	15.8	13.5

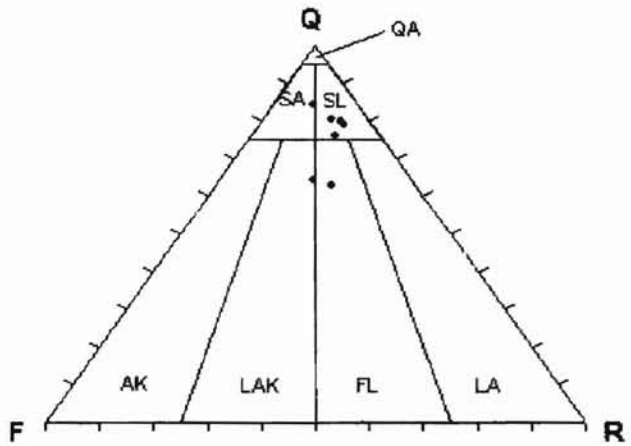

EXPLANATION

Q= Mono- and Poly-cystalline Quartz
F= All Feldspars
R= All Rock Fragments: argillaceous, chert, carbonate, metamorphic, volcanic

QA= Quartz Arenite; SA= Subarkose; SL= Sublitharenite; AK= Arkose; LAK= Lithic Arkose; LA= Litharenite; FL= Feldspathic Litharenite

THIN SECTION ANALYSES

Well Name: A.T. Canales #81 **Field: TCB** **Company: ORYX Energy**
County: Kleberg **Location: Survey 341, A-81**

Thin Section ID	*OV9920*	*OV9925*	*OV9929*	*OV9934*	*OV9936.5*	*OV9940*	*OV9941.5*
Core Depth (feet)	*9920*	*9925*	*9929*	*9934*	*9936.5*	*9940*	*9941.5*
Logging Depth (feet)	*9908*	*9913*	*9917*	*9922*	*9924.5*	*9928*	*9929.5*
TOTAL DETRITAL	60.3	64.6	61.6	57.2	57.9	52.1	58.3
TOTAL QUARTZ	45.2	49.4	42.6	33.7	36.1	35.6	49.8
Quartz Grains	45.2	49.2	42.6	33.7	36.1	35.6	49.8
TOTAL Q, F, R	59.6	63.5	60.0	56.4	56.4	51.0	57.5
Quartz (%)	75.9	77.5	71.0	59.8	64.1	69.7	86.7
Feldspar (%)	12.5	12.1	8.0	18.5	15.2	14.6	7.0
Rock Fragments (%)	11.6	10.4	21.0	23.8	20.8	15.7	6.4
Total (%)	100.0	100.0	100.0	100.0	100.0	100.0	100.0
TOTAL CLAYS	20.8	18.0	29.3	32.7	29.3	32.8	4.3
TOTAL CEMENTS	7.8	10.2	1.9	6.8	5.4	3.4	37.3
Carbonate cements	7.8	9.9	1.9	6.8	5.4	3.4	37.3
Quartz Cements	0	0.2	0	0	0	0	0
POROSITY							
Primary Porosity	tr	tr	tr	tr	tr	tr	tr
Secondary Porosity	11.1	7.2	7.2	3.3	7.5	11.9	0.0

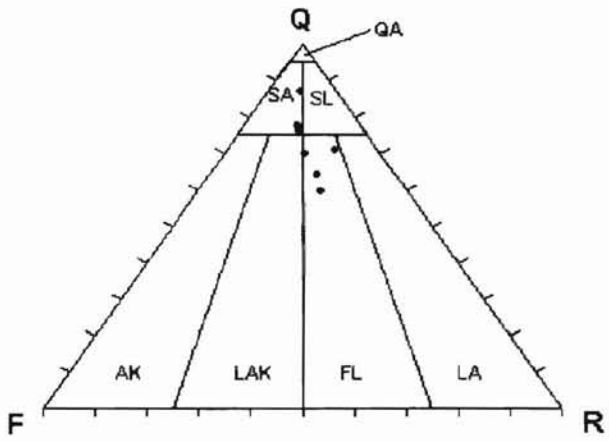

EXPLANATION

Q= Mono- and Poly-cystalline Quartz
F= All Feldspars
R= All Rock Fragments: argillaceous, chert, carbonate, metamorphic, volcanic

QA= Quartz Arenite; SA= Subarkose;
SL= Sublitharenite; AK= Arkose;
LAK= Lithic Arkose; LA= Litharenite;
FL= Feldspathic Litharenite

THIN SECTION ANALYSES

Well Name: A.T. Canales #85 **Field: TCB** **Company: ORYX Energy**
County: Kleberg **Location: Survey 341, ABS-81**

Thin Section ID	*OV10424*	*OV10427*	*OV10431*	*OV10432*	*OV10442*	*OV10447*	*OV10451*
Core Depth (feet)	*10424*	*10427*	*10431*	*10432*	*10442*	*10447*	*10451*
Logging Depth (feet)	*10414*	*10417*	*10421*	*10422*	*10432*	*10437*	*10441*
TOTAL DETRITAL	64.8	70.5	68.5	64.1	73.8	43.7	66.0
TOTAL QUARTZ	48.0	55.3	51.5	40.1	62.3	32.0	49.6
Quartz Grains	48.0	54.0	51.5	40.1	58.5	32.0	49.6
TOTAL Q, F, R	64.4	69.4	67.6	61.8	72.9	42.1	64.5
Quartz (%)	74.5	77.8	76.2	65.0	80.3	75.9	76.9
Feldspar (%)	12.4	7.6	6.5	6.3	7.2	5.4	9.6
Rock Fragments (%)	13.1	14.6	17.3	28.7	12.5	18.6	13.5
Total (%)	100.0	100.0	100.0	100.0	100.0	100.0	100.0
TOTAL CLAYS	23.2	0.0	8.9	16.6	0.4	0.0	23.3
TOTAL CEMENTS	1.9	27.1	6.9	9.6	18.0	56.0	4.2
Carbonate cements	1.9	25.9	6.9	9.6	14.3	56.0	4.2
Quartz Cements	0.0	1.3	0.0	0.0	3.8	0.0	0.0
POROSITY							
Primary Porosity	tr	tr	tr	tr	tr	tr	tr
Secondary Porosity	10.1	2.4	15.7	9.6	7.9	0.3	6.5

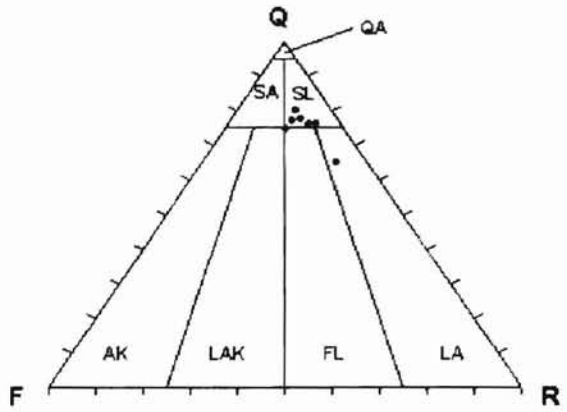

EXPLANATION

Q= Mono- and Poly-cystalline Quartz
F= All Feldspars
R= All Rock Fragments: argillaceous, chert, carbonate, metamorphic, volcanic

QA= Quartz Arenite; SA= Subarkose;
SL= Sublitharenite; AK= Arkose;
LAK= Lithic Arkose; LA= Litharenite;
FL= Feldspathic Litharenite

THIN SECTION ANALYSES

Well Name: A.T. Canales #85 **Field: TCB** **Company: ORYX Energy**
County: Kleberg **Location: Survey 341, ABS-81**

Thin Section ID	*OV10453*	*OV10456*	*OV10459*	*OV10462*	*OV10467*	*OV10471*
Core Depth (feet)	*10453*	*10456*	*10459*	*10462*	*10467*	*10471*
Logging Depth (feet)	*10443*	*10446*	*10449*	*10452*	*10457*	*10461*
TOTAL DETRITAL	57.8	39.3	23.1	67.3	56.2	65.3
TOTAL QUARTZ	39.5	32.0	19.9	47.1	37.9	47.0
Quartz Grains	39.5	32.0	19.9	47.1	37.9	46.1
TOTAL Q, F, R	56.1	38.0	22.4	66.5	54.9	63.9
Quartz (%)	70.4	84.2	88.8	70.9	69.0	72.2
Feldspar (%)	9.8	5.0	4.0	2.6	7.7	7.4
Rock Fragments (%)	19.8	10.8	7.1	26.5	23.3	20.4
Total (%)	100.0	100.0	100.0	100.0	100.0	100.0
TOTAL CLAYS	30.5	55.1	32.3	28.5	36.7	0.0
TOTAL CEMENTS	7.1	5.3	43.6	2.0	1.1	29.6
Carbonate cements	7.1	5.3	43.6	2.0	1.1	28.8
Quartz Cements	0.0	0.0	0.0	0.0	0.0	0.9
POROSITY						
Primary Porosity	tr	tr	tr	tr	tr	tr
Secondary Porosity	4.6	0.3	1.0	2.3	6.0	5.1

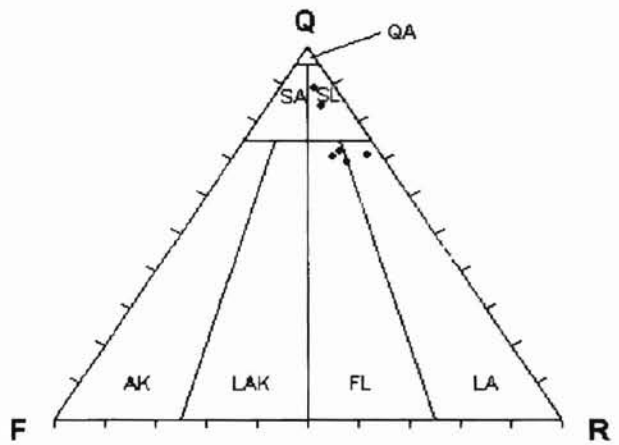

EXPLANATION

Q= Mono- and Poly-cystalline Quartz
F= All Feldspars
R= All Rock Fragments: argillaceous, chert, carbonate, metamorphic, volcanic

QA= Quartz Arenite; SA= Subarkose; SL= Sublitharenite; AK= Arkose; LAK= Lithic Arkose; LA= Litharenite; FL= Feldspathic Litharenite

APPENDIX C

CAPILLARY PRESSURE CURVES

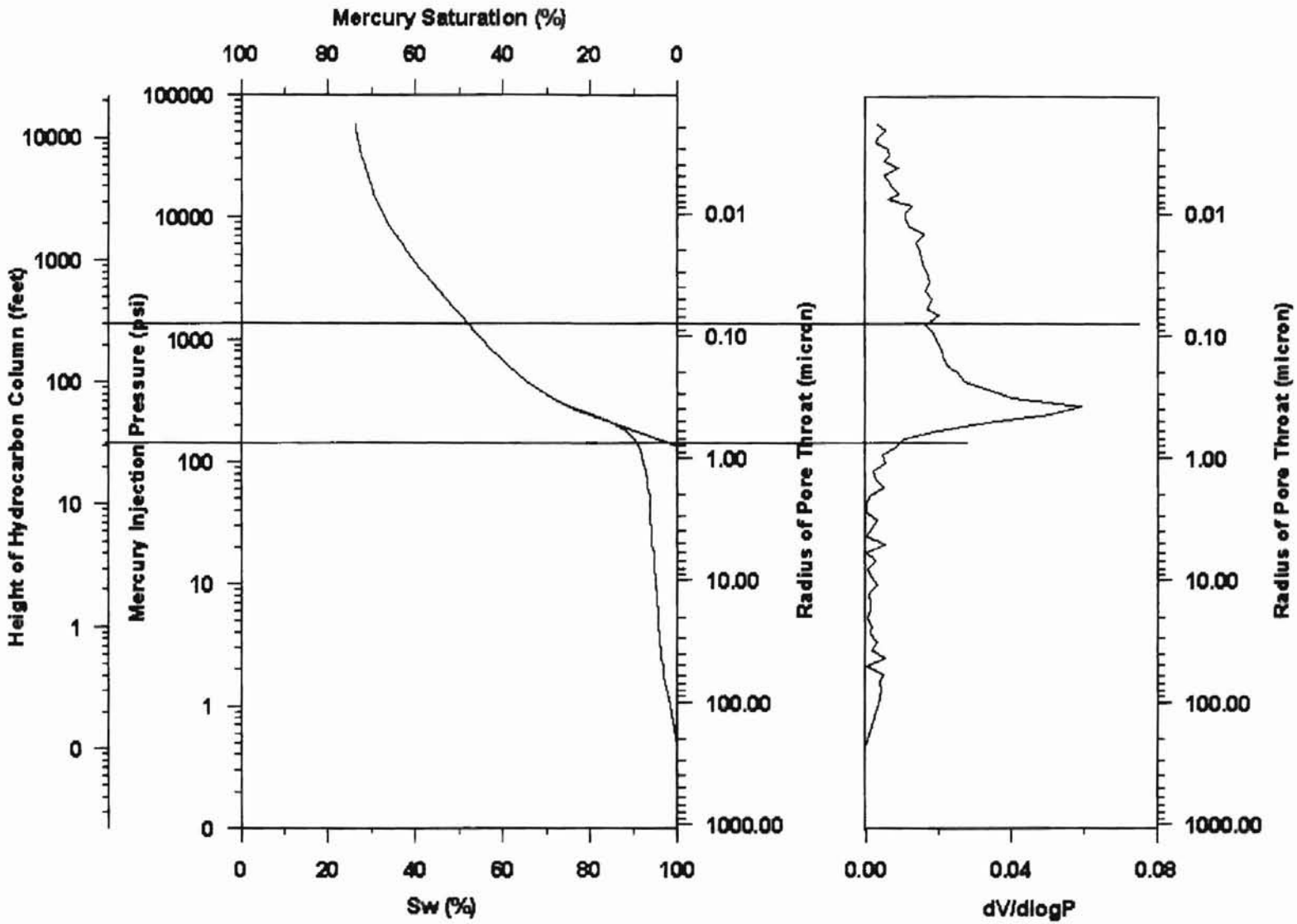

Capillary pressure curve of Sample 85-13.

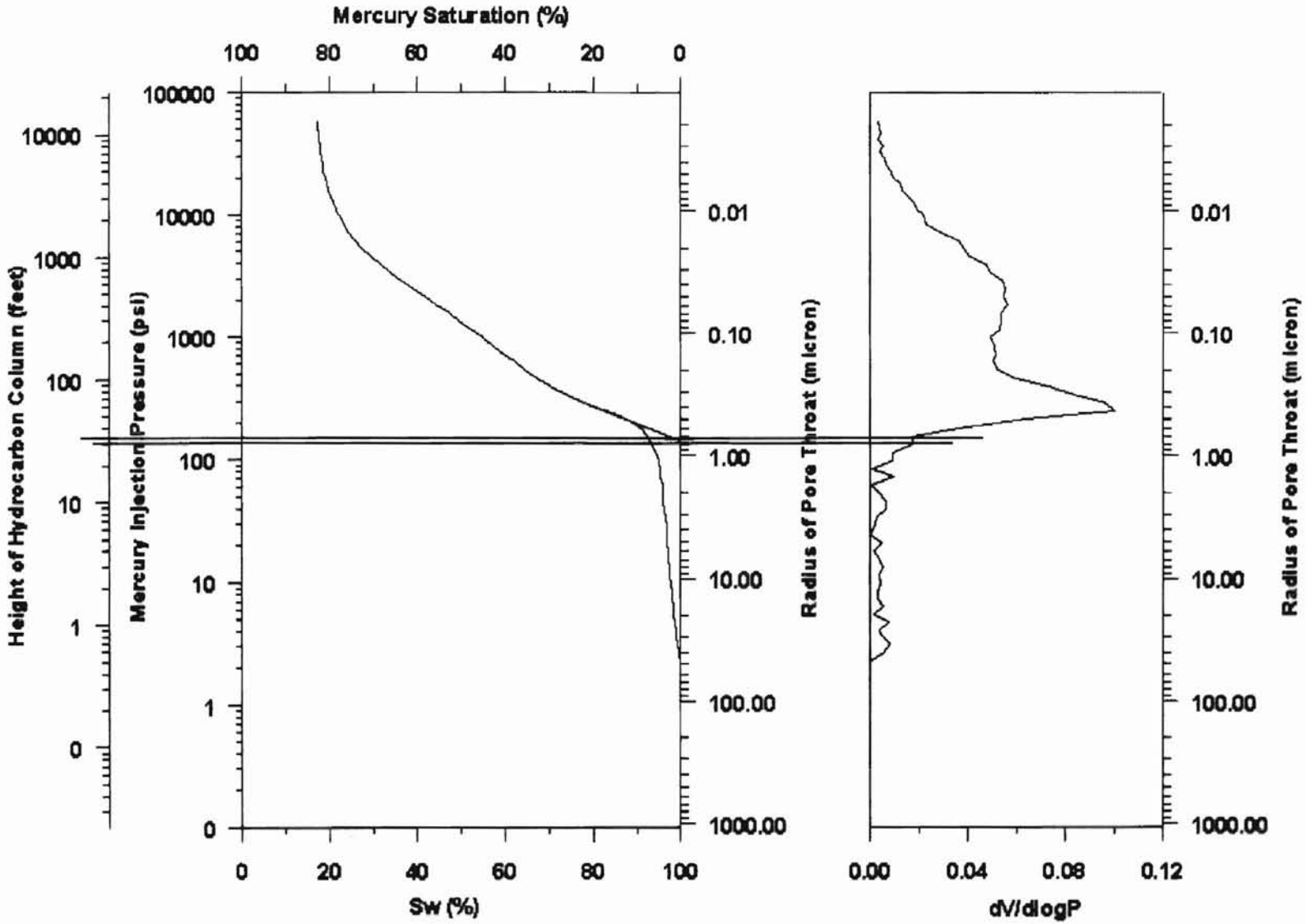

Capillary pressure curve of Sample 85-25.

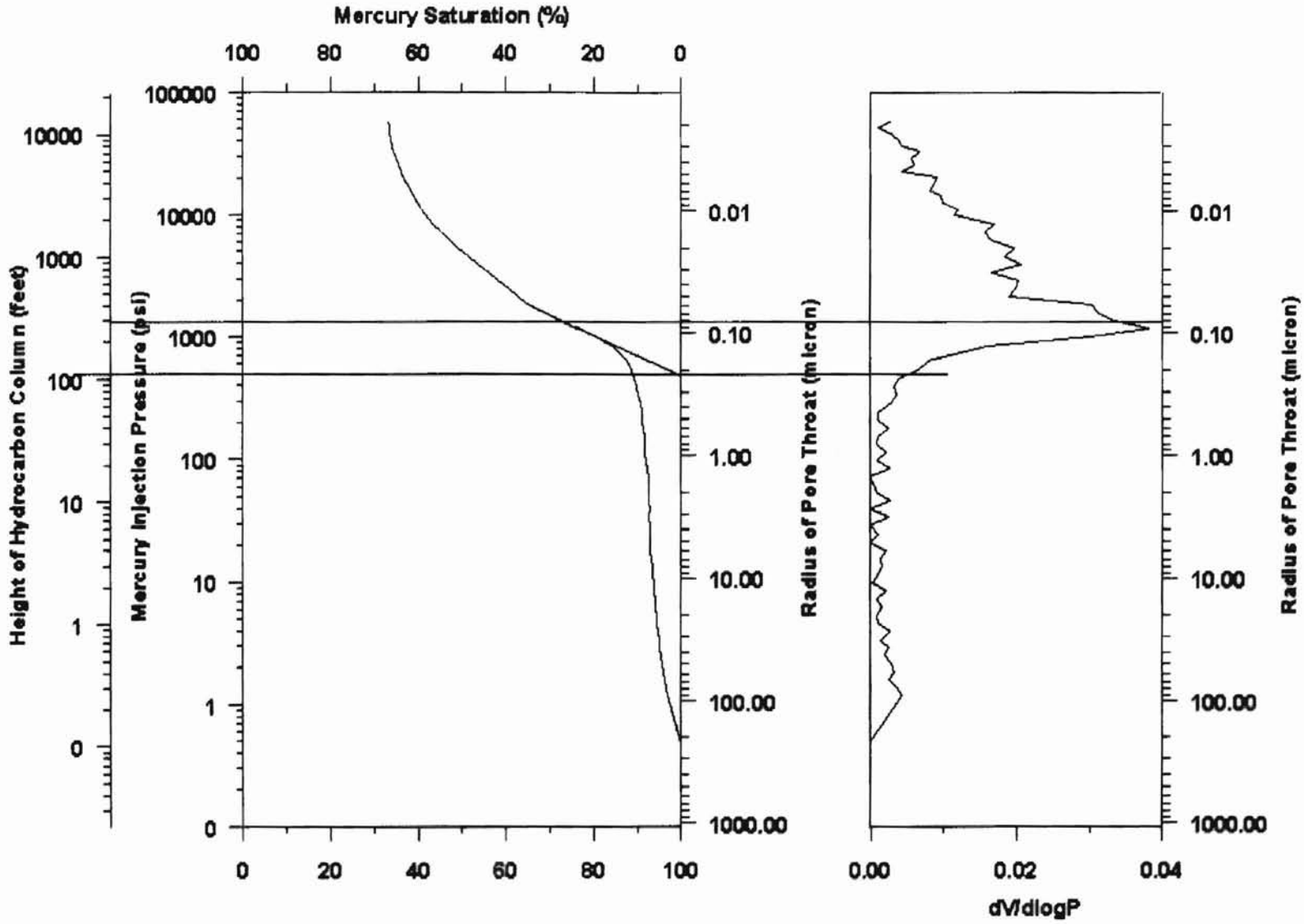

Capillary pressure curve of Sample 85-27.

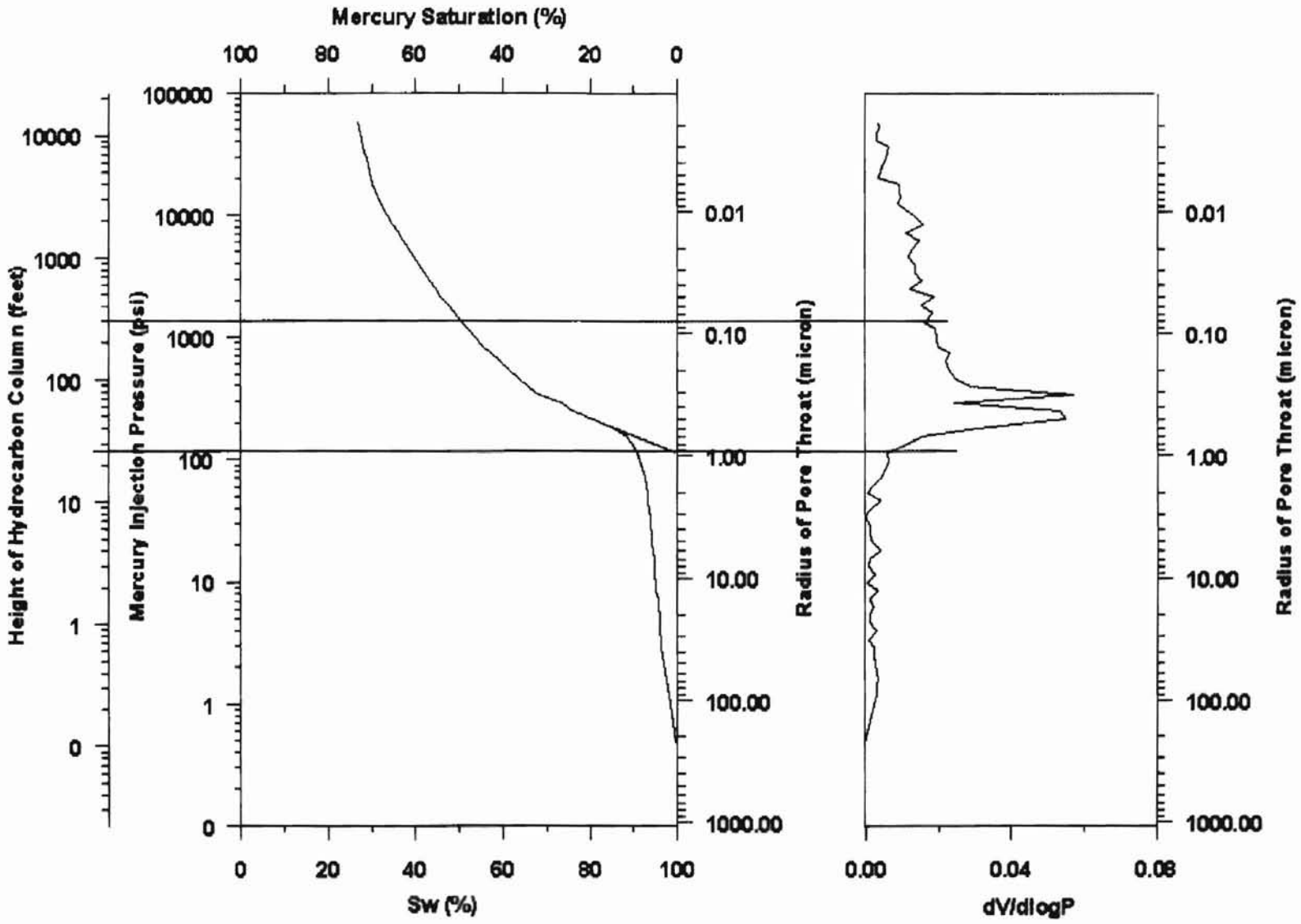

Capillary pressure curve of Sample 85-42.

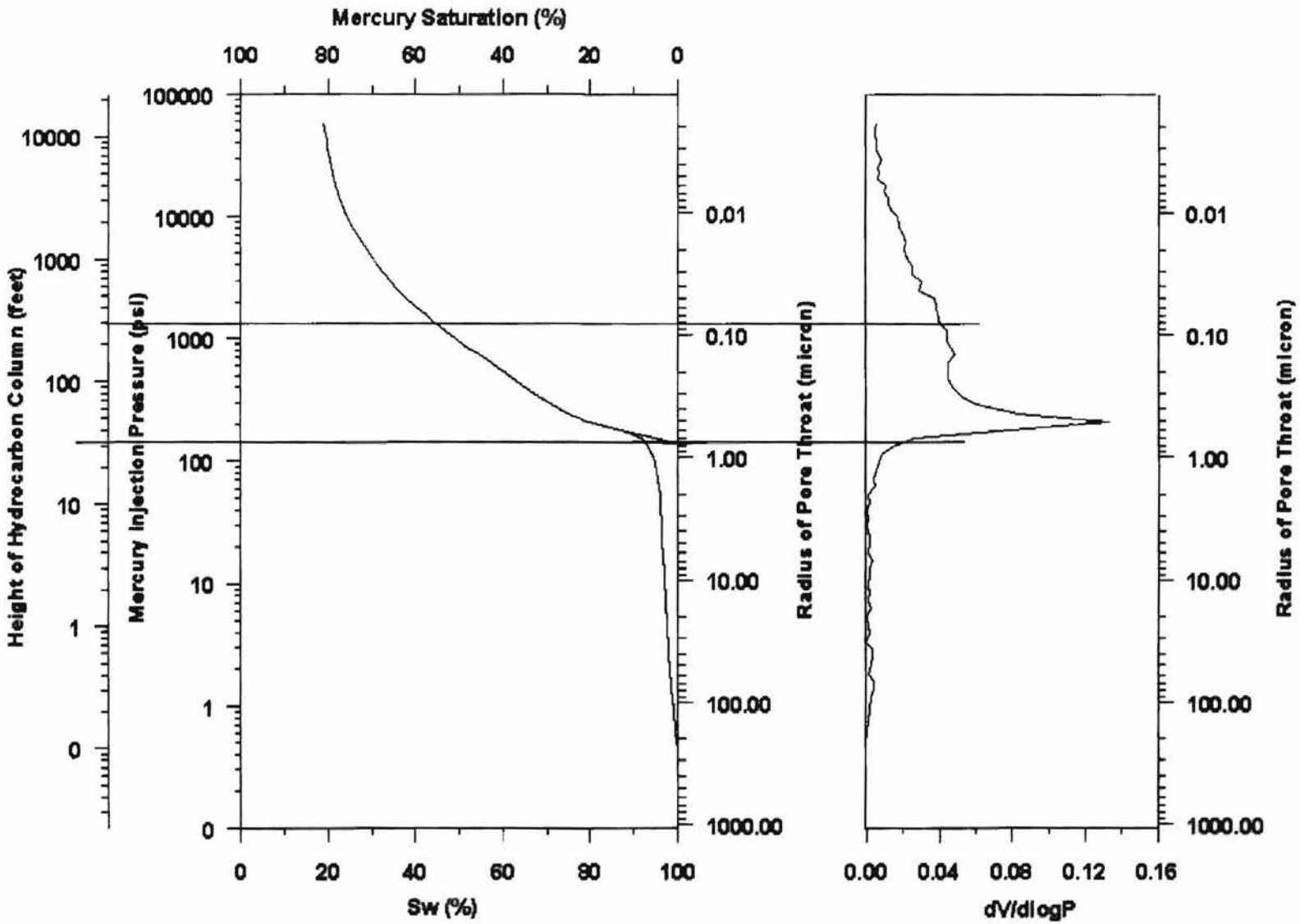

Capillary pressure curve of Sample 85-43.

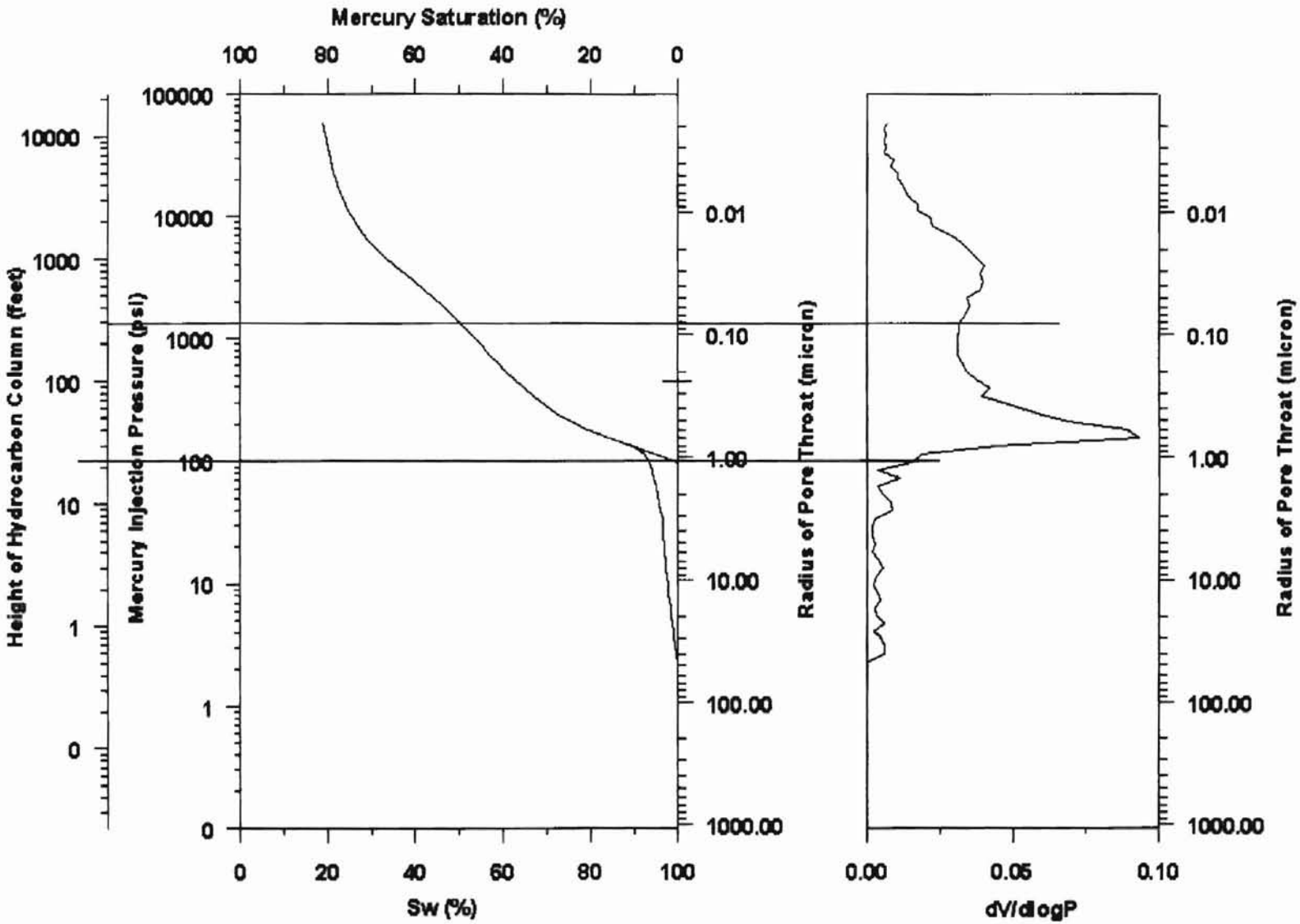

Capillary pressure curve of Sample 85-46.

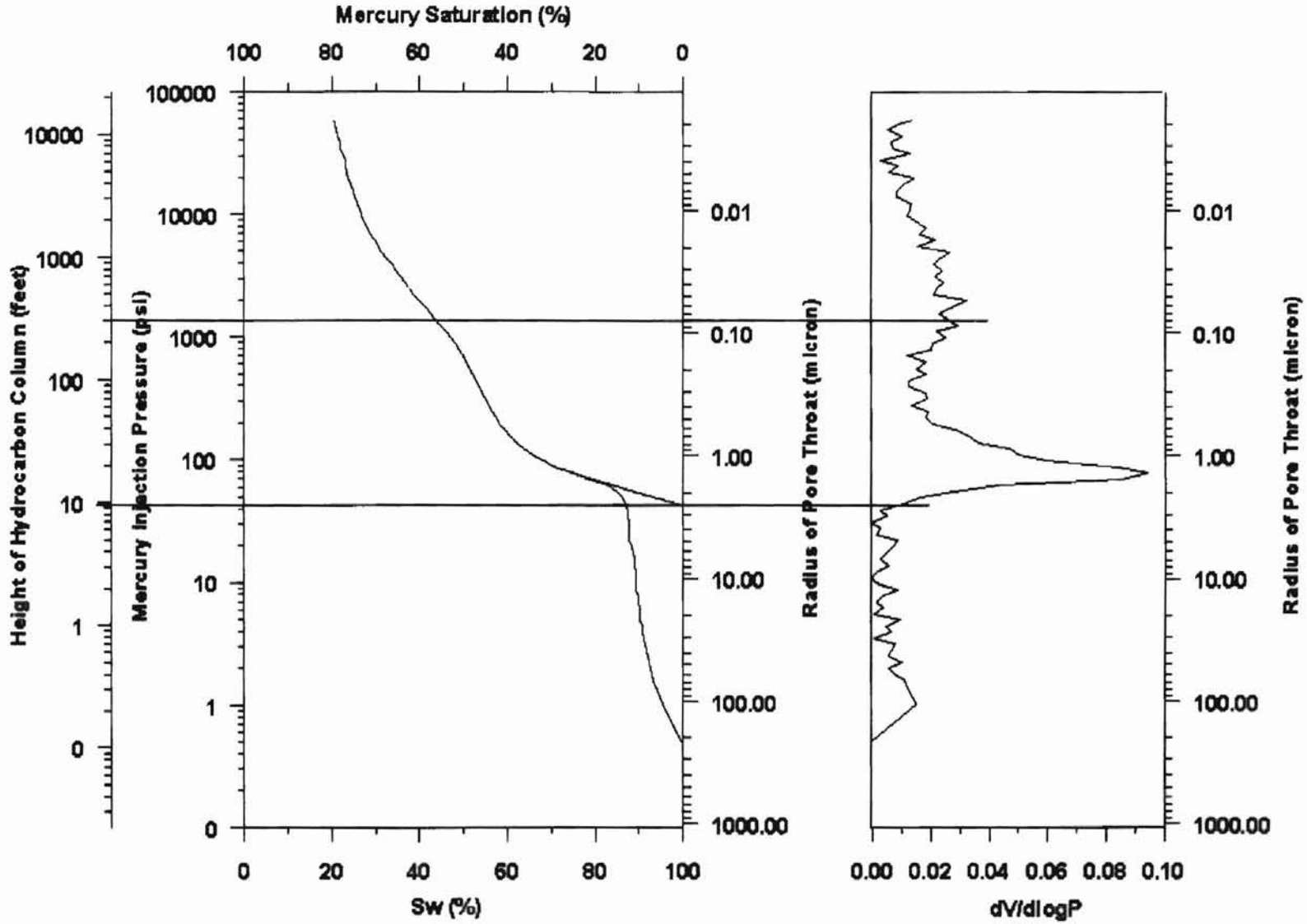

Capillary pressure curve of Sample 81-02.

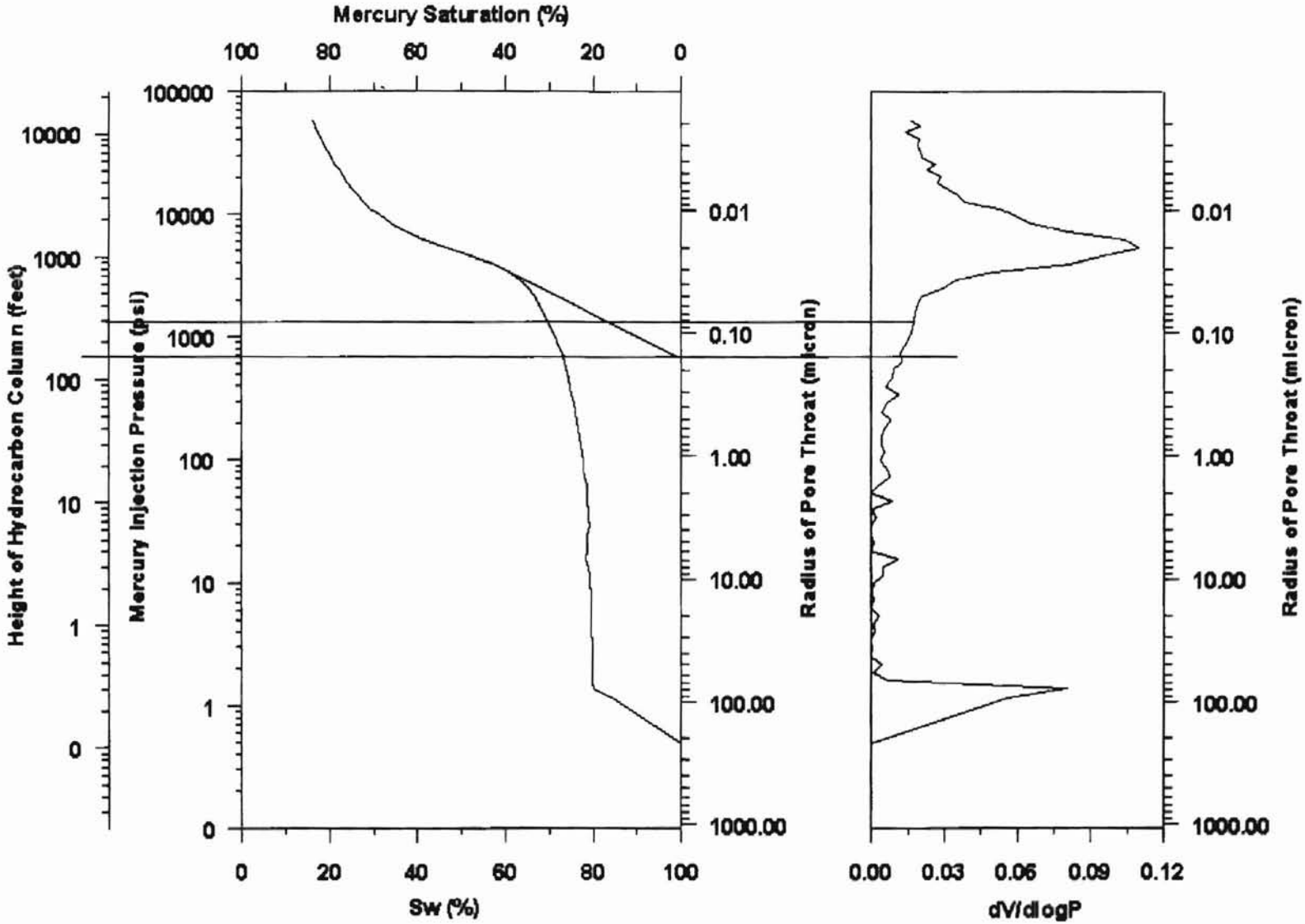

Capillary pressure curve of Sample81-09.

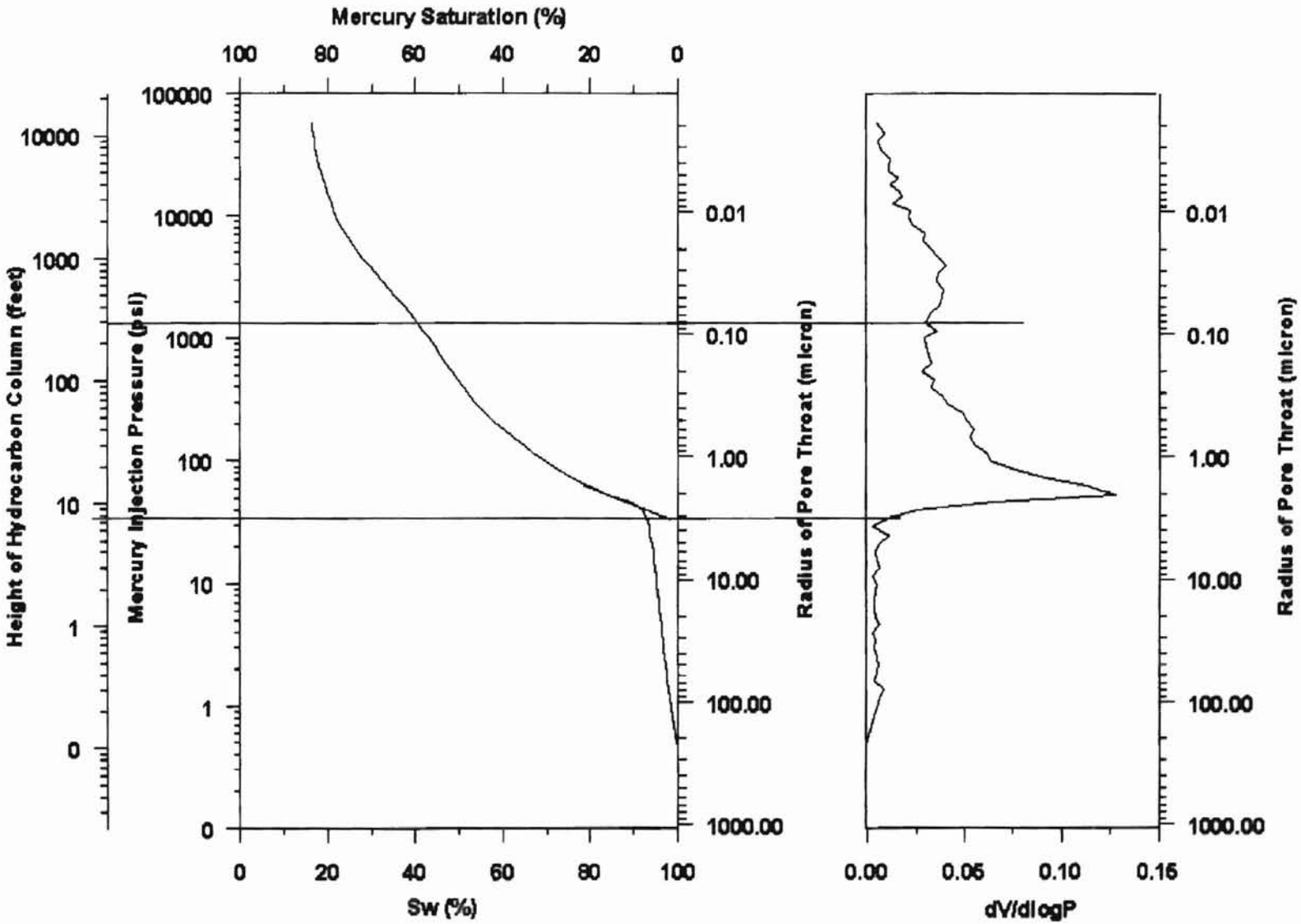

Capillary pressure curve of 81-17.

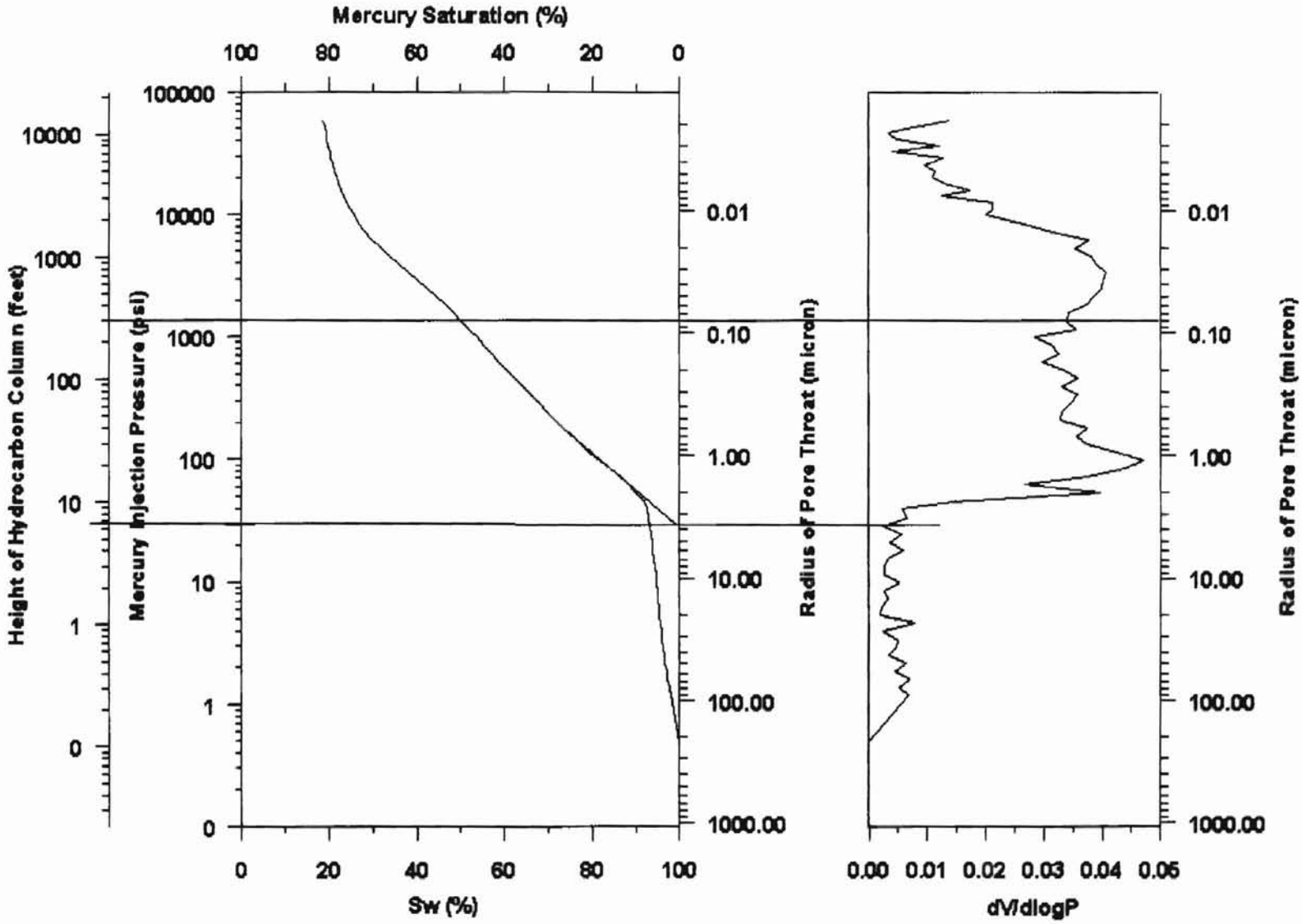

Capillary pressure curve of Sample 81-20.

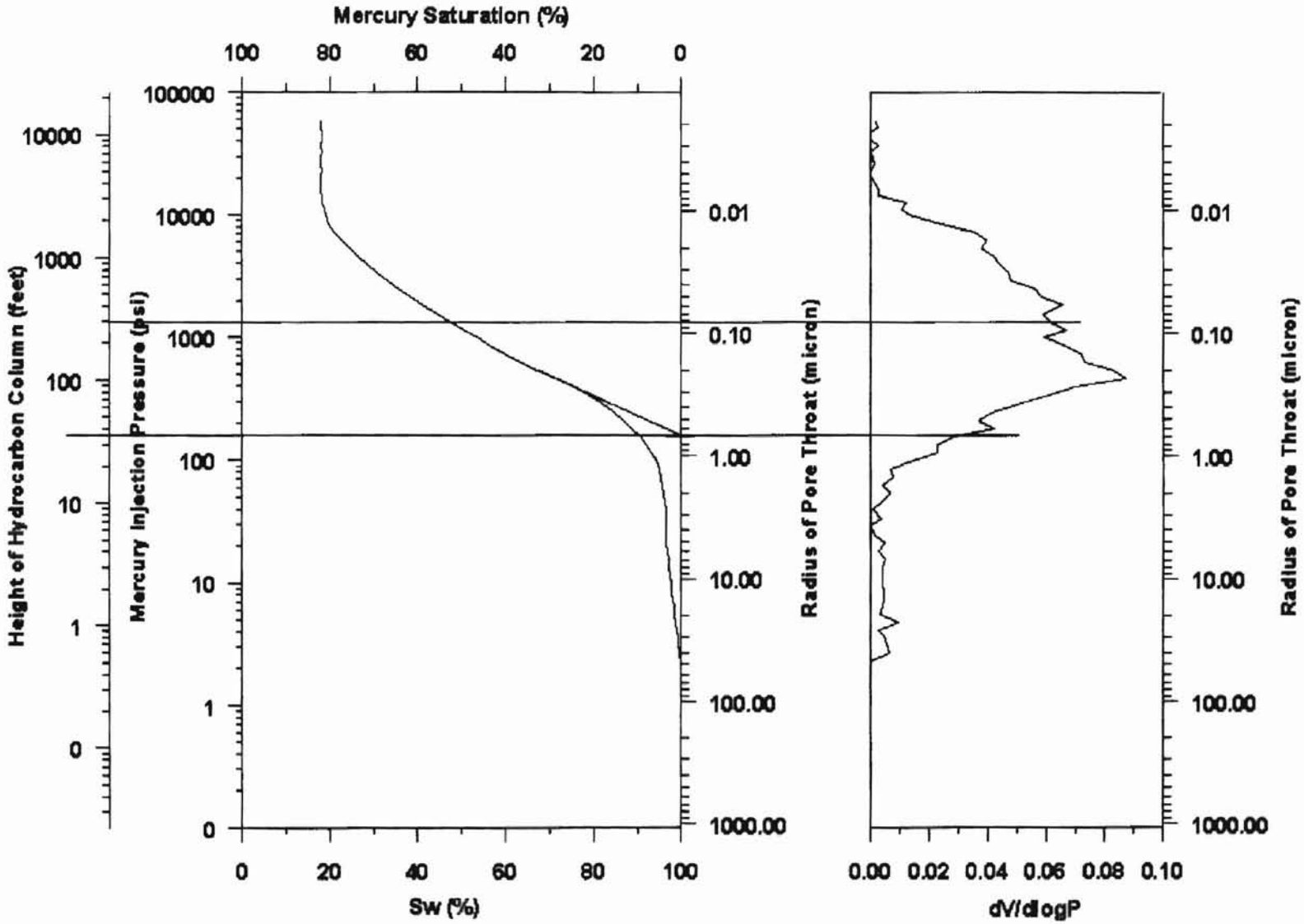

Capillary pressure curve of Sample 81-28.

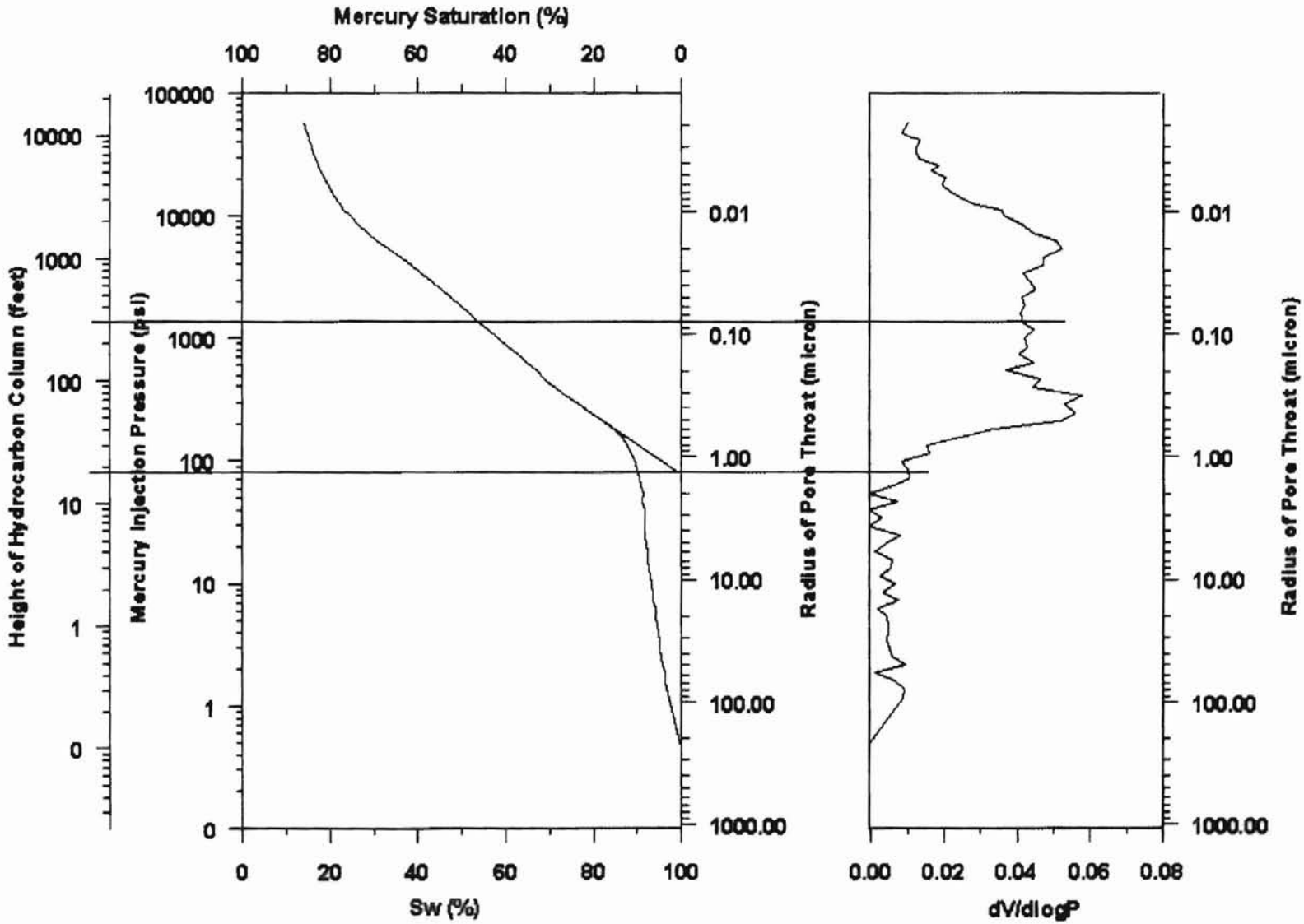

Capillary pressure curve of Sample 81-36.

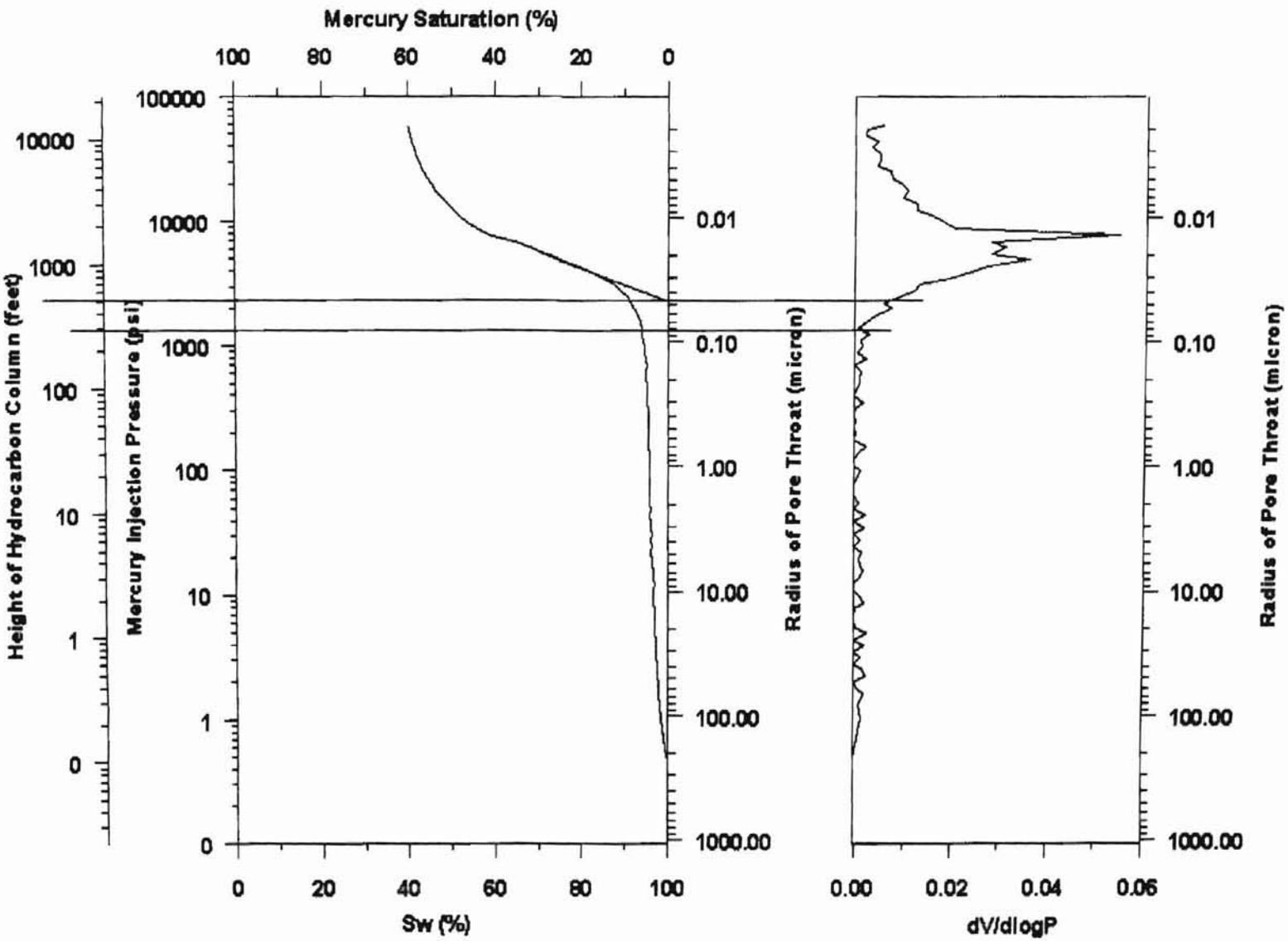

Capillary pressure curve of Sample 81-41.

VITA

Han Li

Candidate for the Degree of

Master of Science

Thesis: CHARACTERIZATION AND PETROPHYSICAL ANALYSIS OF "LOW-CONTRAST" THIN BEDDED VICKSBURG RESERVOIRS, TCB FIELD, KLEBERG COUNTY, TEXAS

Major Field: Geology

Biographical:

Personal Data: Born in Dalian, P. R. China, September 14, 1972, the girl of Yi Li and Hui Kong.

Education: Received Bachelor of Engineering degree in Geology from Sinkiang Petroleum Institute, P. R. China in 1993; received Master of Science degree in Geology from Research Institute of Petroleum Exploration and Development (RIPED), P. R. China in 1997. Completed the requirements for the Master of Science degree with a major in Geology at Oklahoma State University in July, 2000.

Experience: Research and Teaching Assistant, School of Geology, Oklahoma State University, August 1997 to present; Research Assistant, RIPED, P. R. China, September 1995 to July 1997.

Professional Memberships: American Association of Petroleum Geologists, The Honor Society of Phi Kappa Phi.